Dissertation

submitted to the
Combined Faculty of Natural Sciences and Mathematics
of the Ruperto-Carola-University of Heidelberg, Germany
for the degree of
Doctor of Natural Sciences

Put forward by
Marc Anton Alexander Rebholz
born in Konstanz

Oral examination: December 16$^{\text{th}}$, 2020

All-XUV pump-probe transient absorption spectroscopy on the dissociation dynamics of small molecules

Referees: Prof. Dr. Thomas Pfeifer

Prof. Dr. Andreas Wolf

In the beginning there was nothing, which exploded.

TERRY PRATCHETT, LORDS AND LADIES

Transiente Absorptionsspektroskopie zur Dissoziationsdynamik kleiner Moleküle unter der Verwendung von XUV Strahlung für Anregung und Abfrage:

Im Rahmen dieser Arbeit wird die Implementierung von XUV-Pump-XUV-Probe Transienter Absorptionsspektroskopie am Freie-Elektronen-Laser FLASH in Hamburg vorgestellt. Mit Hilfe dieses experimentellen Schemas wird die ultraschnelle Dissoziationsdynamik von Diiodmethan und Sauerstoff untersucht. Im Fall von Diiodmethan ermöglicht dies die resonante, ortsspezifische Anregung eines Iod 4d-Elektrons in ein antibindendes Molekülorbital. Die dadurch eingeleitete Dissoziation des Moleküls umfasst sowohl einen direkten, als auch einen indirekten Dissoziationskanal, welcher über isomere Geometrien des Molekül-Kations abläuft. Diese beiden Dissoziations-Kanäle werden mit Hilfe von simulierten Absorptionsspektren nachverfolgt und ihre Zeitkonstanten werden mittels eines globalen Fit-Modells bestimmt. Im Fall des Sauerstoff-Moleküls wird dessen Dissoziation durch die (mehrfache) Ionisierung des Moleküls eingeleitet. Daraufhin kann das Erscheinen von Absorptionssignaturen des doppelt geladenen ionischen Fragments O^{2+} im Probe-Spektrum beobachtet werden. Die Kompatibilität der gemessenen Anstiegszeiten der Fragmente zu einer Erzeugung durch Coulomb-Explosion wird mit Hilfe eines einfachen klassischen Modells untersucht.

All-XUV pump-probe transient absorption spectroscopy on the dissociation dynamics of small molecules:

In this work, the implementation of an XUV-pump–XUV-probe transient absorption spectroscopy scheme at the free-electron laser facility FLASH in Hamburg is presented. It is applied to the ultrafast dissociation dynamics of the small molecules diiodomethane and oxygen. For the diiodomethane target, the XUV pump pulse enables the resonant site-specific excitation of an iodine 4d electron to an antibonding molecular orbital. The hereby initiated dissociation of the molecule includes a direct, as well as an indirect path through isomeric geometries of the molecular cation. These parallel pathways are traced with the help of simulated absorption spectra and their time constants are extracted via a global fit model. In the case of the oxygen target, dissociation is initiated by the (multiple) ionization of the oxygen molecule. The emergence of absorption resonances of the doubly-charged ionic fragment O^{2+} is observed in the probe spectrum as a product of the dissociation. The compatibility of the extracted rise times of the fragments with Coulomb explosion is investigated with a simple classical model.

Contents

1. Introduction

The spectroscopic examination of matter has led to many important discoveries and has thereby fundamentally shaped our understanding of nature. William Hyde Wollaston and Joseph Fraunhofer independently observed the sharp absorption lines in the spectrum of the sun [1] that, today, are known as Fraunhofer lines. These absorption features, were later associated with different chemical elements by Gustav Kirchhoff and Robert Bunsen [2], which was an important step in the foundation of quantum mechanics. The origin of these discrete absorption lines was explained by Niels Bohr in his quantum model of an atom [3].

The invention of the laser [4, 5] was a breakthrough for the field of spectroscopy. On the one hand, highly stable lasers can be used for precision spectroscopy experiments and to operate atomic clocks, which define the standards for frequency and time [6]. On the other hand, ultrashort mode-locked lasers [7, 8] provide temporal resolution for spectroscopic studies. This enabled for instance the time-resolved investigation of chemical reactions on their natural femtosecond time scales ($1\,\mathrm{fs} = 10^{-15}\,\mathrm{s}$) via pump-probe spectroscopy [9, 10].

Many different experiments are based on the pump-probe spectroscopy scheme presented in reference [9]. Thereby, a dynamic process is initiated in an atomic, ionic, or molecular target by a short laser pulse. The temporal evolution of the system is subsequently probed by a second laser pulse. This method can be combined with the detection of ionic fragments [11], or electrons [12] produced from the target species, as well as with the detection of the transmitted light spectrum of the probe pulse [9].

The advent of synchrotron facilities [13] expanded the accessible spectral range for time-resolved spectroscopy to the extreme ultraviolet (XUV) and x-ray regime, however, limited to a picosecond time resolution ($1\,\mathrm{ps} = 10^{-12}\,\mathrm{s}$).

The discovery of high-harmonic generation (HHG) [14–16] enabled pump-probe spectroscopy experiments with attosecond ($1\,\mathrm{as} = 10^{-18}\,\mathrm{s}$) time resolution [17]. The low pulse energy of HHG radiation in the nJ regime, however, limits the use of this radiation to the probing of a target.

Novel free-electron laser (FEL) light sources provide XUV/x-ray radiation with pulse energies in the µJ regime and femtosecond pulse durations [18] and can thereby overcome this limitation. For instance, the measurement of charge rearrangement dynamics [19], as well as interatomic Coulombic decay (ICD) [20] was demonstrated by combining ion spectroscopy with an XUV-pump–XUV-probe scheme.

In this work, the implementation of XUV-pump–XUV-probe transient absorption spectroscopy at the free-electron laser FLASH in Hamburg [21] is presented. First experiments on the ultrafast dissociation of small molecular targets based on this scheme are discussed. The XUV-pump pulse initiates the dissociation of the target by exciting a nuclear wavepacket onto a dissociating potential energy curve (PEC). Subsequently, the temporal evolution of the system is interrogated by the XUV-probe pulse. The temporal evolution of the target is imprinted into the absorption spectrum of the probe pulse. By varying the pump-probe time delay, the dynamical evolution of the system can be traced. The investigated targets include the halocarbon molecule diiodomethane CH_2I_2 and the oxygen molecule O_2.

This thesis is structured as follows: In chapter 2, the theoretical treatment of absorption is delineated and the properties of ultrashort pulses are introduced. Furthermore, an overview over the interaction mechanisms of XUV/x-ray pulses with matter that are relevant for this work is given. Chapter 3 describes the working principle of a free-electron laser, while chapter 4 introduces the experimental setup. In chapter 5 the calibration of the experiment and the necessary steps for the combination of FEL metadata and the experimental data are described. Chapter 6 treats the nontrivial dissociation dynamics of diiodomethane. In chapter 7 the ultrafast dissociation of oxygen is treated. Finally, a summary of the results and an outlook is given in chapter 8.

2. Theoretical background

In this chapter an overview over the theoretical concepts that are important for the understanding of this work is given. A treatment of the concept of absorption is presented in section 2.1, while in section 2.2 the properties of ultrashort light pulses are summarized. Finally, the different interaction mechanisms of extreme ultraviolet (XUV) and x-ray radiation with matter are introduced in section 2.3.

2.1. Theory of absorption

To get a better understanding of the absorption of light by a medium a semi-classical model is employed in this section. A bound atomic system in an oscillating electric field can be described by a driven harmonic oscillator. The electric field induces an atomic dipole moment

$$\mathbf{d} = e \cdot \mathbf{r}, \tag{2.1}$$

where e is the electron charge and $\mathbf{r}$ is its displacement from the equilibrium position. The macroscopic polarization induced in a medium with a density of atoms per unit volume ρ_N then reads

$$\mathbf{P} = \rho_N e \cdot \mathbf{r}. \tag{2.2}$$

The polarization of a medium consisting of atomic (or molecular) dipoles in an external electric field then follows the equation of motion:

$$\frac{\mathrm{d}^2\mathbf{P}(t)}{\mathrm{d}t^2} + \sigma\frac{\mathrm{d}\mathbf{P}(t)}{\mathrm{d}t} + \omega_0^2\mathbf{P}(t) = \omega_0\epsilon_0\chi_0\mathbf{E}(t), \tag{2.3}$$

with the dielectric susceptibility

$$\chi_0 = \frac{\rho_N e^2}{\epsilon_0 m\omega_0}. \tag{2.4}$$

Here, e is the electron charge, m is the electron mass and ϵ_0 is the electric permittivity constant. To solve this second order differential equation, the oscillating electric field

$E(t) = E\exp(i\omega t)$ and polarization $P(t) = P\exp(i\omega t)$ are substituted into 2.3. This reduces the equation to:

$$(\omega_0^2 - \omega^2 + i\sigma\omega)\mathbf{P} = \omega_0^2\epsilon_0\chi_0\mathbf{E}, \tag{2.5}$$

and results in the following linear relation between electric field and induced polarization:

$$\mathbf{P} = \epsilon_0\frac{\chi_0\omega_0}{\omega_0^2 - \omega^2 + i\sigma\omega}\mathbf{E} = \epsilon_0\chi(\omega)\mathbf{E}. \tag{2.6}$$

Comparison directly gives an expression for the frequency-dependent dielectric susceptibility:

$$\chi(\omega) = \chi_0\frac{1}{\omega_0^2 - \omega^2 + i\sigma\omega}. \tag{2.7}$$

The real and imaginary part of this expression describe the phenomena of dispersion and linear absorption of light in a medium in the vicinity of a resonance:

$$\chi(\omega) = \chi'(\omega) + i\chi''(\omega). \tag{2.8}$$

In the case the driving electric field is comparable to inner-atomic field-strengths ($> 10^{10}\,\mathrm{V\,m^{-1}}$), the linear relation between polarization and electric field breaks down. In order to describe nonlinear processes equation (2.6) can be expanded in a power series:

$$P(\omega) = \epsilon_0\left(\chi^{(1)}(\omega)E(\omega) + \frac{1}{2}\chi^{(2)}(\omega)E^2(\omega) + \frac{1}{6}\chi^{(3)}(\omega)E^3(\omega) + \dots\right). \tag{2.9}$$

The individual $\chi^{(i)}(\omega)$ are the different orders of the nonlinear susceptibility. Due to symmetry reasons $\chi^{(2)}(\omega)$ vanishes for media with inversion symmetry, as is the case for the gaseous targets that are treated in this work. Higher-order terms are comparably weak and can be omitted in most cases.[1] The polarization of the medium follows the oscillating driving field and therefore itself represents an oscillating charge distribution. The electric field that is emitted by the oscillating polarization is described by Maxwell's wave equation:

$$\left(\nabla^2 - \frac{1}{c^2}\frac{\partial^2}{\partial t^2}\right)\mathbf{E}(\mathbf{r}, t) = \mu_0\frac{\partial^2}{\partial t^2}\mathbf{P}(\mathbf{r}, t). \tag{2.10}$$

[1] Electric field and induced polarization are vector quantities. For some materials the susceptibilities can therefore depend on directionality. In that case they have to be treated as tensors. For the homogeneous media investigated in this work this can be neglected.

Here, μ_0 is the magnetic permeability of free space ($\epsilon_0\mu_0 = \frac{1}{c^2}$). Assuming that the light pulse travels in z direction through the medium and its electric field is uniform in the x-y-plane allows to simplify the wave equation to the so-called Helmholtz equation:

$$\left(\frac{\partial^2}{\partial z^2} - \frac{1}{c^2}\frac{\partial^2}{\partial t^2}\right)\mathbf{E}(z,t) = \mu_0 \frac{\partial^2}{\partial t^2}\mathbf{P}(t)\delta(z). \tag{2.11}$$

The analytic solution to this equation is:

$$\mathbf{E}(z,t) = \mathbf{E}_{in}\left(t - \frac{z}{c}\right) + \mathbf{E}_{gen}(z,t), \tag{2.12}$$

with the incoming field $\mathbf{E_{in}}$ and the generated electric field:

$$\mathbf{E}_{gen}(z,t) = \sqrt{\epsilon_0\mu_0}\left[\Theta(z)\frac{\partial}{\partial t}\mathbf{P}\left(t - \frac{z}{c}\right) + \Theta(-z)\frac{\partial}{\partial t}\mathbf{P}\left(t + \frac{z}{c}\right)\right]. \tag{2.13}$$

In a typical experiment scheme that involves the absorption of light by a medium, it is not possible to directly detect the oscillating electric field of the light field. The involved time scales are on the order of femtoseconds for visible light ($1\,\mathrm{fs} = 10^{-15}\,\mathrm{s}$) and, therefore, much shorter than any available electronics are able to resolve. Instead, typically the spectrum of the light field's intensity is recorded, which is given by:

$$I(\omega) \propto \left|\int \mathrm{d}t\; e^{i\omega t}\mathbf{E}(z,t)\right|^2. \tag{2.14}$$

The Fourier transforms of the incoming and generated field component are:

$$\begin{aligned}\mathbf{E}_{in}(\omega) &= \int \mathrm{d}t\; e^{i\omega t}\mathbf{E}_{in}(t)\\ \mathbf{E}_{gen}(\omega) &\propto \int \mathrm{d}t\; e^{i\omega t}\frac{\partial}{\partial t}\mathbf{P}(t) = i\omega\int \mathrm{d}t\; e^{i\omega t}\mathbf{P}(t) = i\omega\mathbf{P}(\omega)\end{aligned} \tag{2.15}$$

From 2.15 it follows that the induced polarization oscillates with a $\pi/2$ phase-shift compared to the driving electric field. Using the above expressions, the spectral intensity can be written as:

$$\begin{aligned}I(\omega) &\propto \left|\mathbf{E_{in}}(\omega)\right|^2 + 2\,\mathrm{Re}\left[i\;\mathbf{E}^*_{in}(\omega)\cdot\mathbf{P}(\omega)\right] + \left|\mathbf{E_{gen}}(\omega)\right|^2\\ &\propto I_0(\omega) + 2\,\mathrm{Re}\left[i\;\mathbf{E}^*_{in}(\omega)\cdot\mathbf{P}(\omega)\right] + I_{gen}(\omega)\end{aligned} \tag{2.16}$$

Usually the intensity of the generated dipole radiation is weak compared to the

incident radiation ($I_{gen}(\omega) \ll I_0(\omega)$) and can therefore be neglected.[2] The absorption of light can then be understood exclusively as an interference phenomenon between the incoming field and the induced dipole emission of the medium (free-induction decay). A more detailed treatment of this theory of absorption can be found in references [22–24]. To quantify observed experimental data the optical density (OD) of a medium is used. It is directly proportional to the absorbance of the medium and is defined as:

$$\begin{aligned} \mathrm{OD} &= -\log_{10}\left[\frac{I(\omega)}{I_0(\omega)}\right] \\ &\propto \mathrm{Im}\left[\chi^{(1)}(\omega)\right]. \end{aligned} \tag{2.17}$$

Equation 2.17 can be reformulated to Lambert-Beer's law of absorption:

$$I(\omega, z) = I_0(\omega) e^{-\alpha(\omega) z}, \tag{2.18}$$

with the macroscopic absorption coefficient

$$\alpha(\omega) = \rho_N \sigma(\omega), \tag{2.19}$$

which in turn is composed of the microscopic absorption cross section $\sigma(\omega)$ times the number density of the medium ρ_N. As is shown in [25], the absorption coefficient α is directly linked to the imaginary part of the susceptibility. For the microscopic absorption cross section this translates to:

$$\sigma(\omega) \simeq \frac{1}{\rho_N} \frac{\omega}{c} \mathrm{Im}\left[\chi(\omega)\right]. \tag{2.20}$$

With equation (2.6) the absorption cross section can then be written as:

$$\sigma(\omega) \simeq \frac{\omega}{\epsilon_0 c} \mathrm{Im}\left[\frac{d(\omega)}{E(\omega)}\right]. \tag{2.21}$$

2.2. Ultrashort laser pulses

The propagation of an electromagnetic wave is described by the wave equation (2.10) that can be derived directly from Maxwell's equations. In the case of an electromagnetic wave that travels in direction z and is uniform in its lateral extension

[2] This assumption breaks down for dense media where a photon can interact multiple times with the medium and for the case of nonlinear absorption in the medium.

the wave equation can be simplified to the Helmholtz equation (2.11):

$$\left(\frac{\partial^2}{\partial z^2} - \frac{1}{c^2}\frac{\partial^2}{\partial t^2}\right)\mathbf{E}(z,t) = \mu_0 \frac{\partial^2}{\partial t^2}\mathbf{P}(t).$$

Inserting the relation between induced polarization and driving electric field (2.6) into (2.11) leads to:

$$\left(\frac{\partial^2}{\partial z^2} - \underbrace{\left[1+\chi(\omega)\right]\frac{1}{c^2}}_{k^2(\omega)}\frac{\partial^2}{\partial t^2}\right)\mathbf{E} = 0 \tag{2.22}$$

The most obvious solution to this differential equation is a plane wave:

$$\mathbf{E}(z,t) = \mathbf{E_0} e^{-i(\omega t - kz)}, \tag{2.23}$$

with the wave vector:

$$k^2 = \frac{n^2(\omega)\omega^2}{c^2} \tag{2.24}$$

and the refractive index $n(\omega)$ [25], [26]. From:

$$\mathbf{E}(z,t) = \mathbf{E_0} e^{-i\omega\left(t \mp \frac{n(\omega)}{c} z\right)}, \tag{2.25}$$

it can be seen that $\frac{c}{n(\omega)}$ is the velocity with which this wave propagates. Since eq. (2.25) represents a plane wave which, per definition, has an endless extension this velocity has no real-world meaning in the sense of a propagating laser pulse. It rather is the velocity of the phase front of the electromagnetic wave and is therefore called the phase velocity v_{ph}. In a real-world experiment using ultrashort laser pulses that interact with a target medium, the involved fields have of course a finite temporal duration. Such laser pulses can be described as a wave packet with frequency components distributed around a carrier frequency ω. The following wave packet is also a solution to the Helmholtz equation (2.22) [25, 26]:

$$\mathbf{E}(z,t) = \int_{-\infty}^{\infty} \mathrm{d}\omega' \; \tilde{\mathbf{E}}(\omega') e^{-i\left[\omega' t - k(\omega')\cdot z\right]}. \tag{2.26}$$

The wave packet can also parametrized, using its carrier frequency ω and the distribution of frequencies (Δ) around its carrier frequency: $\omega' = \omega + \Delta$. The change of

variables then results in:

$$\begin{aligned}\mathbf{E}(z,t) &= \int_{-\infty}^{\infty} \mathrm{d}\Delta\ \tilde{\mathbf{E}}(\omega+\Delta)e^{-i(\omega+\Delta)t}e^{ik(\omega+\Delta)\cdot z} \\ &= e^{-i\left[\omega t - k(\omega)\cdot z\right]} \int_{-\infty}^{\infty} \mathrm{d}\Delta\ \tilde{\mathbf{E}}(\omega+\Delta)e^{-i\Delta\cdot t}e^{i\left[k(\omega+\Delta)-k(\omega)\right]z} \\ &\equiv \mathcal{E}(z,t)e^{-i\left[\omega t - k(\omega)\cdot z\right]}.\end{aligned} \tag{2.27}$$

Here $\mathcal{E}(z,t)$ describes the envelope of the laser pulse, whereas the exponential term describes its phase evolution. The propagation of the laser pulse is determined by the evolution of its envelope $\frac{\partial\mathcal{E}(z,t)}{\partial z}$. After some derivation that is elaborately done in [26] the following expression can be found:

$$\frac{\partial\mathcal{E}(z,t)}{\partial z} = -\left(\frac{\mathrm{d}k}{\mathrm{d}\omega}\right)\bigg|_{\omega}\cdot\frac{\partial\mathcal{E}}{\partial t} - \frac{i}{2}\left(\frac{\mathrm{d}^2k}{\mathrm{d}\omega^2}\right)\bigg|_{\omega}\cdot\frac{\partial^2\mathcal{E}}{\partial t^2} + \frac{1}{6}\left(\frac{\mathrm{d}^3k}{\mathrm{d}\omega^3}\right)\bigg|_{\omega}\cdot\frac{\partial^3\mathcal{E}}{\partial t^3} + \ldots, \tag{2.28}$$

which can be rewritten to:

$$\frac{\partial\mathcal{E}(z,t)}{\partial z} + \frac{1}{v_g}\cdot\frac{\partial\mathcal{E}}{\partial t} + \frac{i}{2}\beta\cdot\frac{\partial^2\mathcal{E}}{\partial t^2} - \frac{1}{6}\beta_3\cdot\frac{\partial^3\mathcal{E}}{\partial t^3} + \cdots = 0. \tag{2.29}$$

Here v_g is the group velocity with which the pulse envelope propagates. The β_n are the different orders of dispersion coefficients that depend on material properties. In vacuum they vanish and the solution to eq. (2.29) is a gaussian pulse

$$\mathcal{E}(z,t) = \mathcal{E}_0 e^{-\left(t-\frac{z}{v_g}\right)/2\tau_p^2} \tag{2.30}$$

of duration τ_p. In the case of vanishing dispersion coefficients this pulse will travel without ever changing its shape or pulse duration.[3] If the pulse travels through a medium with non-vanishing β, but $\beta_3 = 0$ it experiences group-velocity dispersion (GVD). The solution to its equation of motion (2.29) is:

$$\mathcal{E}(z,t) = \frac{\mathcal{E}_0}{\sqrt{1-i\frac{\beta z}{\tau_p}}} e^{\frac{-\tau}{2\tau_p^2(z)}} e^{-i\phi(z,t)}, \tag{2.31}$$

[3]This is only true in the absence of absorption or amplification of the pulse as these processes can also alter the pulse parameters.

with $\tau = t - \frac{z}{v_g}$. In this case the pulse stretches in time while traveling through the dispersive medium. Its duration after having traveled the distance z is:

$$\tau_p(z) = \sqrt{\tau_p^2 + \left(\frac{\beta z}{\tau_p}\right)^2}. \tag{2.32}$$

When working with ultrashort laser pulse one has to account for these effects. From eq. (2.31) it can be seen, that the pulse will retain its gaussian shape while propagating. However its temporal duration changes according to eq. (2.32). For large propagation distances where the pulse length has significantly spread ($\tau_p(z) \gg \tau_p$), the pulse duration can be directly related to the bandwidth $\Delta\omega = \frac{1}{\Delta\omega}$ of the pulse:

$$\tau_p(z) = |\beta| z \Delta\omega. \tag{2.33}$$

The increase in pulse duration is caused by individual frequency components traveling with different group velocities. The pulse is said to be chirped in analogy to the chirping sound of birds. From eq. (2.29) it can be seen that:

$$\beta = \frac{\mathrm{d}}{\mathrm{d}\omega}\left(\frac{1}{v_g}\right) = -\left(\frac{1}{v_g^2}\right)\frac{\mathrm{d}v_g}{\mathrm{d}\omega}. \tag{2.34}$$

There are different measures to counteract group-velocity dispersion, such as chirped-mirror compressors or grating compressors that introduce negative GVD to compensate for the GVD acquired while passing through a material (glass, air, ...). One can relate the spectral bandwidth and the pulse duration through the inequality[4]:

$$\tau_{\mathrm{FWHM}} \cdot \Delta\omega_{\mathrm{FWHM}} \geq 2\pi K_p. \tag{2.35}$$

A fully compressed laser pulse is called bandwidth- or transform limited. In this case the equality in eq. (2.35) holds. The constant K_p is dependent on the exact pulse shape. For a Gaussian laser pulse $c = 2\ln(2)/\pi$. For different pules shapes other constants can be found. While traveling in a material the Gaussian laser pulse also acquires the phase:

$$\phi(z,t) = \frac{\beta z \tau^2}{2\tau_p^2 \tau_p(z)^2}. \tag{2.36}$$

[4]Here, the full-width at half maximum values of the pulse's intensity ($\mathcal{E}_0^2$) are used. For a Gaussian pulse it is: $\tau_{\mathrm{FWHM}} = \sqrt{4\ln 2}\tau_p$

This phase can be expanded in a power series to get a better understanding of its temporal behavior:[5]

$$\phi(t) = \phi_{\mathrm{CEP}} + \frac{\partial\phi}{\partial t} + \phi^{(n)}. \tag{2.37}$$

Here, ϕ_{CEP} is the so-called carrier-envelope phase. It describes the offset between the maximum of the pulse envelope $\mathcal{E}(z,t)$ and the electric field maximum. The term $\frac{\partial\phi}{\partial t} \equiv \omega_{\mathrm{inst}}$ is called the instantaneous frequency and describes the frequency of the chirped laser pulse at a certain point in time. It is often desired to treat the spectral phase of the pulse instead of the temporal phase, since spectra of ultrashort pulses can directly be measured. The temporal structure of the pulses usually has to be inferred from the complex-valued Fourier transform that involves knowledge of the spectral phase. Analog to (2.37) the spectral phase can be expanded in a power series:

$$\phi(\omega) = \sum_{n=0}^{\infty} \frac{(\omega-\omega_0)^n}{n!} \left.\frac{\partial^n\phi}{\partial\omega^n}\right|_{\omega_0} = \sum_{n=0}^{\infty} \frac{(\omega-\omega_0)^n}{n!} D_n. \tag{2.38}$$

The individual D_n are the so-called dispersion coefficients and are used to quantify the effects different materials have on the pulse. D_0 represents, again, the carrier-envelope phase, this time in the spectral domain. D_1 is the equivalent of a temporal delay of the pulse that is called the group delay (GD), and D_3 is the group-delay dispersion (GDD) that describes the change in instantaneous frequency of the pulse (chirp). It has to be noted that GDD is a material property. It is simply the group-velocity dispersion of a material with length l: GDD = GVD $\cdot\, l$. The treatment of higher-order dispersion effects follows the same lines and can be found in various text books, e.g. [25] and [26]. It is of no particular importance for this work and will therefore be omitted here.

For the experiments conducted in this work, femtosecond free-electron laser (FEL) pulses are used. The source of these pulses is the FEL FLASH in Hamburg, which relies on the self-amplified spontaneous emission (SASE) process to initiate lasing. The obtained SASE pulses are partially coherent ultrashort laser pulses of stochastic nature. The propagation of such SASE pulses and their interaction with matter shares most of the properties with conventional ultrashort laser pulses. However, they possess a spiky substructure in their temporal profile, as well as in their spectrum (see section 3.4, Figure 3.4) due to random jumps in the spectral phase. Their properties are discussed in more detail in section 3.4.

[5] This expansion is true for all pulse shapes, not only for Gaussian pulses.

2.3. Interaction of extreme ultraviolet (XUV) and x-ray radiation with matter

In this section, the different interaction mechanisms of XUV and x-ray radiation with matter, as well as how these interactions can be used to investigate the electronic structure of matter are briefly outlined.

2.3.1. The photoelectric effect

Under the general term of photoelectric effect, three distinct albeit similar mechanisms are summarized, all of which have in common the ejection of an electron via the absorption of a photon. The external photoelectric effect was discovered in the late 19^{th} century [27–30]. For its interpretation Albert Einstein was awarded the Nobel prize in physics in 1921 [31]. Photons hitting a solid material with a photon energy $E_{phot} = h\nu$ greater than the characteristic work function W of the material are able to release electrons from the material. The kinetic energy of the free electrons is thereby given by:

$$E_{kin} = h\nu - W, \tag{2.39}$$

with the Planck constant h and the frequency of the photons ν.

In the case of a semiconducting material the internal photoelectric effect increases the material's conductance by generating electron-hole pairs. This effect can be used to generate electric energy from light (photovoltaic effect).

The effect with most relevance for this work is the photoionization, also called the atomic photoeffect. When an atom is hit with a photon of sufficient photon energy, a bound electron is released from the atom. Upon irradiation with extreme ultraviolet (XUV) or x-ray light, even inner-shell electrons can be released from the atom (see Figure 2.1). In the case of photoionization, one typically does not speak of the work force but of the ionization potential I_p of an atom. The photoelectric effect is a strong confirmation for the quantum nature of light and is thereby a key experiment for the foundation of quantum mechanics.

2.3.2. Relaxation of electronically excited atoms and molecules

The absorption of a photon can also leave an atom or molecule in an excited state. With the extreme ultraviolet radiation used in this work, even inner-shell electrons

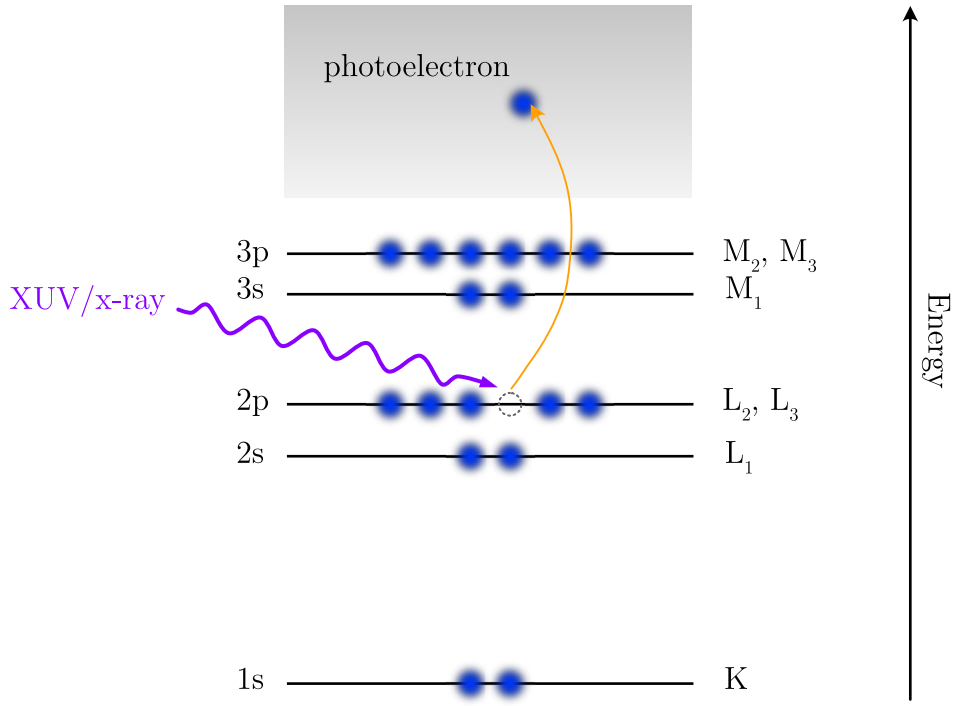

Figure 2.1.: Photoionization of an atom. The incoming XUV/x-ray radiation promotes an initially bound electron into the continuum.

can be resonantly excited due to the high photon energy of the radiation. Hereby, an inner-shell vacancy is created in the system. Such an excited state will decay over time although it is an eigenstate of the field-free hamiltonian H_0, since, in general, it is no eigenstate of the total hamiltonian $H = H_0 + V$ that has contributions from the electromagnetic field. Even in the case of all external fields being exactly zero, the vacuum fluctuations of the electromagnetic field remain and lead to the decay of the excited state.

There are various decay channels for excited atoms and molecules. The ones with significance for this work are delineated in this section. Their depiction can be found in Figure 2.2. Radiative decay (Figure 2.2a) preferably happens in low-Z atoms. All relaxation processes where a photon is emitted fall under this category (e.g. fluorescence). It is important to note, that normally only transitions with a non-vanishing dipole moment are considered. All other transitions are highly suppressed.

Auger decay describes the process where an inner-shell hole of an atom or molecule is filled and the excess energy is used to eject another electron. If no valence electron

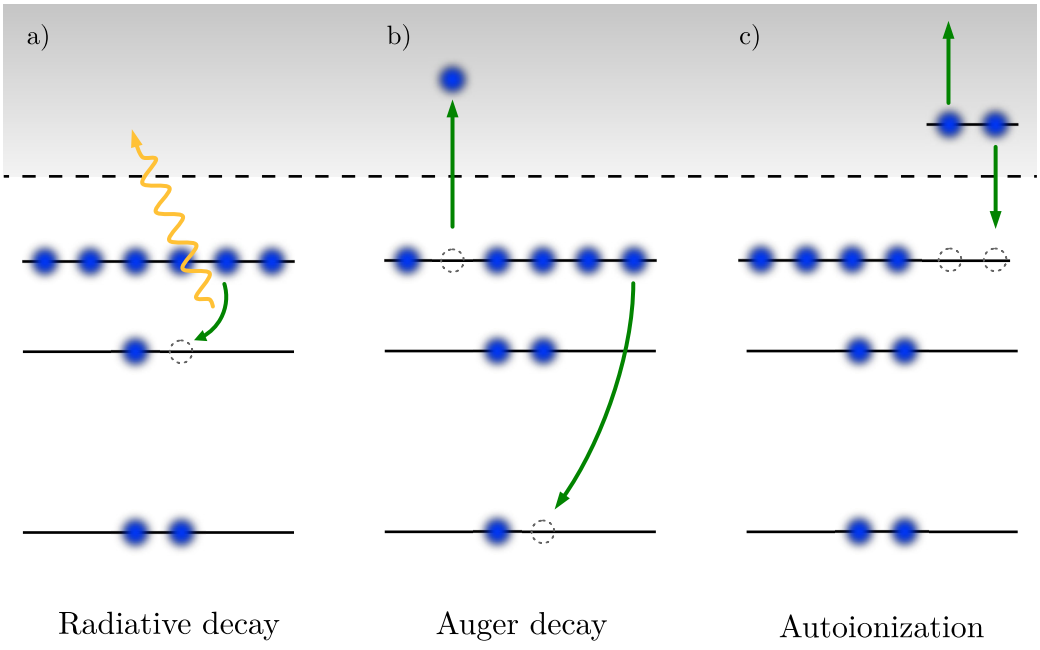

Figure 2.2.: The different relaxation processes of an excited atom or molecule. a) Radiative decay: An electronic vacancy in an inner shell is filled by an electron from an energetically higher shell. The excess energy is released in the form of a photon. b) Auger decay: An inner-shell vacancy is filled by an electron from a higher shell. The excess energy is used to release another electron with a certain kinetic energy from the system. c) Autoionization: Due to the correlation between electrons, one photon can simultaneously excite two electrons into a bound state above the ionization threshold. When one electron relaxes, the excess energy is used to release the second electron.

but an inner-shell electron is ejected a whole cascade of Auger decays can follow. This is mainly the case for larger atoms. Auger decay is the preferable relaxation channel for intermediate-Z atoms. The iodine 4d-vacancy, which plays an important role in the experiments described in this thesis (see chapter 6), relaxes mainly through an Auger process [32].

Autoionization (Figure 2.2c) happens due to the correlation of electrons through Coulomb interaction. One photon of sufficient energy is able to excite two electrons simultaneously. These doubly-excited states are often embedded in an ionization continuum. When one of the excited electrons relaxes, the released energy is transferred to the second electron, thereby ionizing the system. This process is indistinguishable from direct photoionization (cf. Figure 2.1). The interference of these indistinguishable quantum pathways gives rise to so-called Fano-lineshapes [33].

2.3.3. X-ray photoelectron spectroscopy

X-ray photoelectron spectroscopy (XPS) is based on the photoelectric effect and is used to get insight into the electronic structure of a target species. The target is illuminated with x-ray radiation of a distinct photon energy $E_{\text{phot.}}$. The kinetic energy $E_{\text{kin.}}$ of the ejected photoelectrons is measured in a time-of-flight spectrometer. Through energy conservation this directly relates to the released electron's binding energy via

$$E_{\text{binding}} = E_{\text{phot.}} - (E_{\text{kin.}} + W), \tag{2.40}$$

where W is the characteristic work force of the target. In Figure 2.3 the mechanism

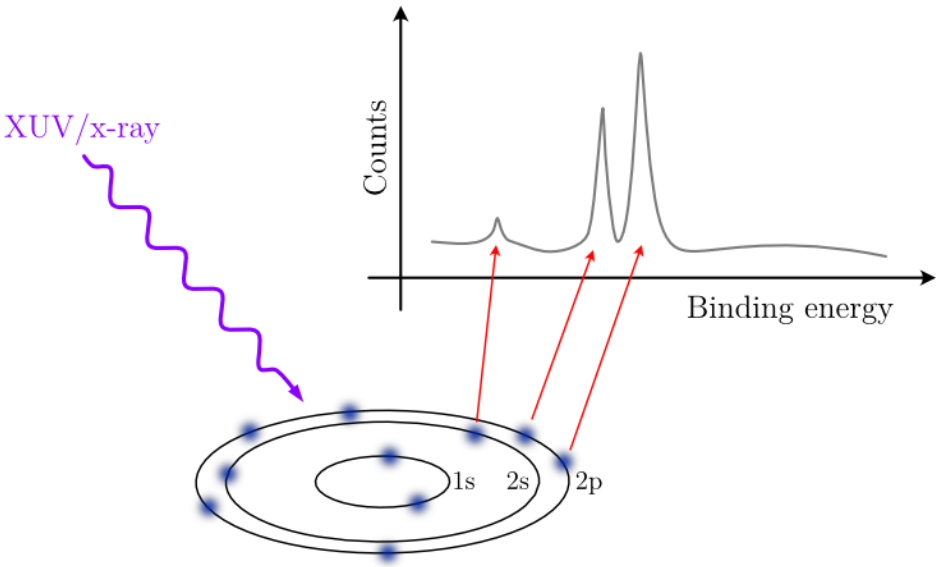

Figure 2.3.: Working principle of x-ray photoelectron spectroscopy. Incoming XUV/x-ray radiation ionizes an atom or molecule. Depending on its photon energy, the light can release electrons from different bound states. Resonances in the kinetic energy spectrum of the released electrons give insight into the electronic structure of a system.

of an XPS experiment is shown. The characteristic peaks in the electron spectrum are element-specific and give a detailed look into the electronic structure of the target. The first x-ray photoelectron spectrum was already recorded in 1907 [34]. The technique was later developed into a powerful analytical tool for the physical and chemical sciences by Kai Siegbahn [35], who was awarded the Nobel prize in physics in 1981 for his work on XPS. Extensions of XPS make use of the angle-resolved detection of electrons and the coincidence detection of electrons and ions [11, 36].

2.3.4. X-ray absorption spectroscopy

X-ray absorption spectroscopy (XAS) is a powerful technique that is used in a broad field of researches. This is due to the fact that XAS enables to easily distinguish between different elements since the binding energy of electrons is highly element-specific. One can even resolve the ionization state of an atom bound in a molecule or a solid-state body due to the chemical shift in binding energies for different states of matter. XAS is used in molecular and condensed matter physics, as well as in chemistry, material science and biology to learn about the structure and composition of a material. The basic scheme of XAS can be found in Figure 2.4. An isolated atomic species shows characteristic absorption edges as depicted in blue in Figure 2.4. As long as the photon energy of the incident photon is smaller than the ionization

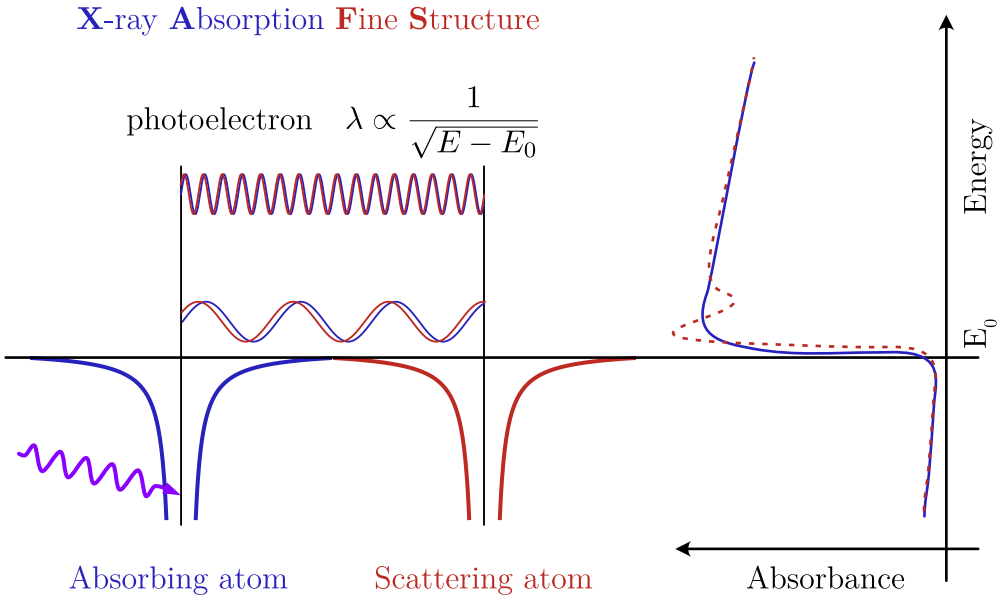

Figure 2.4.: Schematics of x-ray absorption spectroscopy (XAS) and its extension to dense targets (XAFS). As long as the photon energy of the incoming radiation is below the ionization potential of an atom, no electrons are released from the atom and the absorption is low. When the photon energy exceeds this threshold, a sharp increase in absorption is observed. The emerging absorption edges are element-specific and even state-selective. Is the absorbing atom in the vicinity of a second atom, rescattering of the electronic wavefunction can occurs. This leads to an oscillating structure imprinted on the absorption edges.

potential ($E_{\text{phot.}} < I_P$) no electrons can be released from the atom and the absorption is comparatively low. When the photon energy exceeds this threshold the absorption increases in a near step-like manner (see Figure 2.4). Such absorption edges exist for

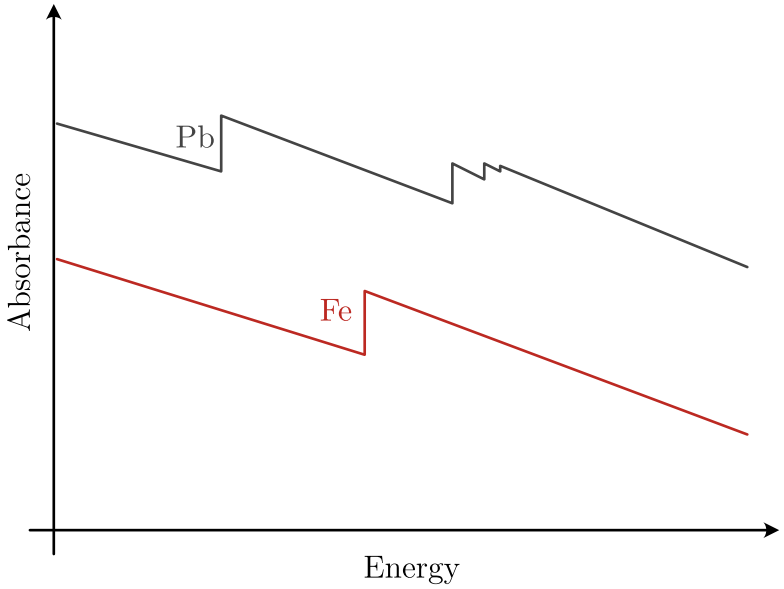

Figure 2.5.: Element specific absorption edges.

every bound electron and are characteristic for an element (see Figure 2.5)

For an atomic target, or when the experimental focus lies on these absorption edges one speaks of x-ray absorption near-edge structure (XANES). In the case of a dense target, a more complex absorption spectrum is found due to rescattering of the free-electron wave packet at neighboring atoms. Depending on their energy the initial and the rescattered electron wave packets interfere constructively or destructively which leads to an oscillating structure imprinted on the absorption spectrum, as is depicted in the red dashed curve in Figure 2.4. This is called the x-ray absorption fine structure (XAFS, see Figure 2.4). The period of this oscillation is related to the distance between absorbing and rescattering atom. This can be used to measure the bond length of a molecule or the lattice constant of a crystal.

However, not only the absorption edges originating from ionization thresholds are characteristic for specific elements. Transitions between bound electronic levels in the XUV/ x-ray spectral range are equally element-specific [37]. The lead to absorption resonances below the absorption edges. These transitions are highly dependent on the electronic environment. They can therefore be used to investigate the chemical shift introduced by different oxidation states [38] or the influence of the electronic environment of atoms bound in a molecule [39, 40]. Furthermore, the resonant site-specific excitation of a molecular target is possible which provides a promising tool for

the investigation of molecular dynamics triggered by local excitation (see chapter 6).

3. Free-electron lasers (FELs)

Synchrotron facilities provide access to extreme-ultraviolet (XUV) and even soft-x-ray radiation since the 1980's [13]. However, the temporal resolution of these facilities is limited to the picosecond regime. In the visible spectral range, advances in ultrashort laser physics made it possible to study electronic processes within atoms and molecules on their natural femtosecond timescales ($1\,\mathrm{fs} = 10^{-15}\,\mathrm{s}$) [9, 10]. The discovery of high-harmonic generation (HHG) provided a new source for XUV radiation, with a temporal resolution down to the attosecond ($1\,\mathrm{as} = 10^{-18}\,\mathrm{s}$) regime [14–16]. However, the intensities provided by HHG sources are comparatively low (in the nJ regime). The implementation of a laser in the XUV/soft-xray spectral region is to this day a research target. It is not easily possible to reach the population inversion that is needed for an efficient laser gain medium [41–47]. Additionally, most materials have very strong absorption in the XUV/soft-x-ray spectral range and the refractive indices of most materials are close to 1 in this spectral range, which renders refractive optics very inefficient. This makes the use of lenses impossible. Reflective optics work to some extent, however, it is necessary to use them under very small grazing incidence angles (typically $\lesssim 10°$ for 50 eV radiation) if the reflection over a broad spectral range is desired. Multilayer coated mirrors exist, which can be optimized for the reflection in a narrow spectral range. In general, the technical requirements on the quality of such optical elements are tremendously high. Deviations in the planarity of flat mirrors, or errors in the curvature of focusing mirrors have to be small compared to the light's wavelength which is $\sim 25\,\mathrm{nm}$ for 50 eV radiation. Additionally, the surface roughness has to be on the sub-1 nm-level, otherwise diffuse reflection reduces the reflection efficiency by several 10 %.

To overcome these issues, the synchrotron effect is used to operate sources for high-intensity XUV radiation. Relativistic charged particles, when accelerated, emit radiation tangential to their direction of propagation. Synchrotron facilities can in this way provide radiation from the XUV to the hard-x-ray regime with excellent beam stability and have been around since the 1970s. However, their pulse duration

is limited to the picosecond range. Free-electron lasers (FELs) are able to overcome this limitation and provide pulse durations in the femtosecond regime. Additionally their peak brilliance[1] is up to 10 orders of magnitude higher than that of a bright synchrotron source [21]. This allows for the realization of nonlinear spectroscopy schemes in the XUV spectral range. The experiments in this work were performed at the **F**ree-electron **LAS**er in **H**amburg (FLASH). It was the first FEL to reach the extreme-ultraviolet spectral region and is online since 2005.

3.1. Undulator radiation

In synchrotron facilities the electromagnetic radiation is produced by forcing a relativistic electron beam on a sinusoidal trajectory. This is done in a so-called undulator (see Figure 3.1). The same effect is exploited in free-electron lasers, albeit using a linear accelerator instead of the circular accelerators employed in synchrotrons. This is due to the much higher charge of individual electron bunches, which is required to achieve lasing in a free-electron laser. Coulomb repulsion leads to the expansion of the electron bunches, so that they cannot be recycled. The produced radiation is also called undulator radiation.

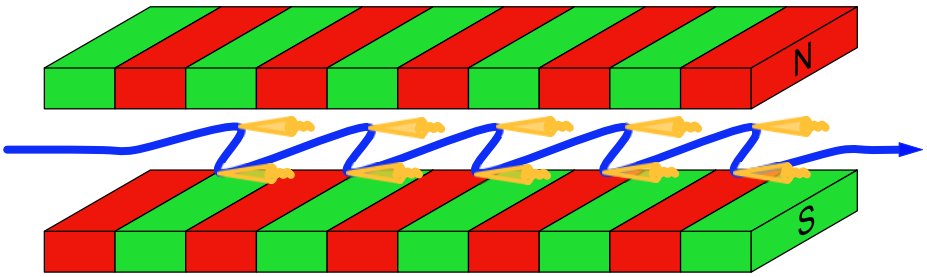

Figure 3.1.: FEL undulator. An electron beam, accelerated in a linear accelerator, is forced onto a sinusoidal trajectory via periodically poled magnets. Through the synchrotron effect it emits radiation with a photon energy depending on the electron kinetic energy. Due to the relativistic speed of the electron beam, most of the produced radiation is emitted in forward direction.

[1] brilliance $= \frac{\text{photons}}{\text{s}\cdot\text{mrad}^2\cdot\text{mm}^2\cdot 0.1\,\%\text{BW}}$

The working principle of a free-electron laser is delineated in this section. It follows the lines of [48], where a much more detailed treatment can be found. To produce the undulator radiation an electron beam is accelerated to (highly-) relativistic speeds. It is then forced on a sinusoidal trajectory using a system of alternating magnets with period λ_u called an undulator (see Figure 3.1). Due to Lorentz contraction the electron beam experiences the period:

$$\lambda_u^* = \frac{\lambda_u}{\gamma}, \tag{3.1}$$

with the Lorentz factor $\gamma = 1/\sqrt{1 - v_{el}^2/c^2}$. The frequency of the electron's oscillation is Doppler-shifted in the laboratory frame:

$$\nu = \gamma(1 + \beta)\nu^*, \tag{3.2}$$

where $\beta = \frac{v}{c}$ and the * denotes the moving frame. For the wavelength of the oscillation it follows:

$$\lambda = \frac{\lambda_u}{\gamma^2}\frac{1}{1+\beta} \simeq \frac{\lambda_u}{2\gamma^2}. \tag{3.3}$$

However, this does not take into account the oscillatory motion of the electron beam inside the undulator. For an electron beam traveling in z direction the magnetic field inside of the undulator is:

$$\mathbf{B} = -B_0 \sin(k_u z)\mathbf{e_y}, \tag{3.4}$$

with the wave vector of the undulator $k_u = 2\pi/\lambda_u$ and the unit vector in y direction $\mathbf{e_y}$. The electrons inside the undulator experience acceleration perpendicular to their direction of propagation due to the Lorentz force:

$$\gamma m_e \frac{\partial \mathbf{v}}{\partial t} = -e\mathbf{v} \times \mathbf{B}. \tag{3.5}$$

This equation can be transformed into two coupled equations of motion for the transverse (x) and longitudinal (z) direction of motion, with the solutions [48]:

$$\begin{aligned} x(t) &= \frac{K}{\gamma k_u}\sin(\omega_u t), \\ z(t) &= \bar{v}_z t - \frac{K^2}{8\gamma^2 k_u}\sin(2\omega_u t). \end{aligned} \tag{3.6}$$

Here, $\bar{v}_z$ is the average longitudinal velocity:

$$\bar{v}_z = \left(1 - \frac{1}{2\gamma^2}\left(1 + \frac{K^2}{2}\right)\right) c \equiv \bar{\beta} c, \tag{3.7}$$

$\omega_u = \bar{\beta} c k_u$ and K is the so-called undulator parameter:

$$K = \frac{eB_0}{m_e c k_u}. \tag{3.8}$$

It is important to note that the longitudinal velocity is not constant [Eq. (3.6)]. With these findings eq. 3.3 can be generalized to [48]:

$$\lambda = \frac{\lambda_u}{2\gamma^2}\left(1 + \frac{K^2}{2}\right). \tag{3.9}$$

The electromagnetic radiation emitted by the relativistic electron beam has the wavelength given by Eq. (3.9). The radiation is emitted in a cone of opening angle $\Theta_{max} \simeq \frac{K}{\gamma}$. It can be shown that contributions from different points of the electron beam's trajectory only interfere constructively for $K \leq 1$ [48, 49]. This condition has to be fulfilled to form a stable light beam.

3.2. Energy exchange between electron beam and light field

Electron beam and generated undulator radiation in general are pulsed. For simplicity the undulator radiation is here treated as a plane electromagnetic wave. All derivations are in principle also valid for a pulsed light field.

$$E_x(z,t) = E_0 \cos(kz - \omega t + \varphi_0) \tag{3.10}$$

The change in the electron beam's energy W with time can be written as:

$$\frac{\mathrm{d}W}{\mathrm{d}t} = \mathbf{v} \cdot \mathbf{F} = -e v_x(t) E_x(t). \tag{3.11}$$

Two cases have to be distinguished here. For $\frac{\mathrm{d}W}{\mathrm{d}t} < 0$ the light wave gains energy from the electron beam and for $\frac{\mathrm{d}W}{\mathrm{d}t} > 0$ the light wave loses energy. From eq. 3.11 it can be directly seen that for the light to gain energy, transverse electron velocity v_x and the

electric field vector E_x have to be aligned (see Figure 3.2). Since the electron beam

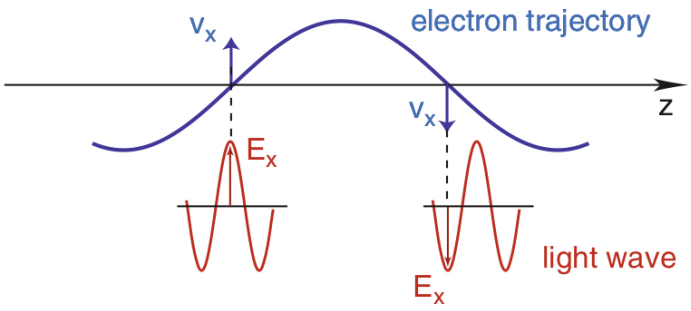

Figure 3.2.: Necessary phase-matching condition for the efficient energy exchange between electron and light beam. The transverse velocity of the electron and the electric field vector of the generated light field have to point in the same direction [cf. Eq. (3.11)]. Graphic reprinted from [48].

will always travel with a velocity $\bar{v}_z < c$ (eq. 3.7), but more importantly due to the oscillating trajectory of the electrons, there will be some slippage in this alignment during the propagation. To ensure coherent buildup of radiation the following phase-matching condition has to be achieved: While the electron beam travels half a period of its trajectory, the light wave has to move forward by half its wavelength $\frac{\lambda_{ph}}{2}$ (see also Figure 3.2). This phase matching condition can also be expressed via the temporal difference between electrons and photons:

$$\Delta t = t_{el} - t_{ph} = \left(\frac{1}{\bar{v}_z} - \frac{1}{c}\right)\frac{\lambda_u}{2} \stackrel{!}{=} \frac{\lambda_{ph}}{2c}. \tag{3.12}$$

From this the wavelength of the emitted radiation can be directly expressed:

$$\lambda_{ph} = \frac{\lambda_u}{2\gamma^2}\left(1 + \frac{K^2}{2}\right). \tag{3.13}$$

It can be seen that the expressions for the wavelength of the emitted radiation (eq. (3.13)) and the expression for the undulator wavelength in the rest frame (eq. (3.9)) are in fact identical. For undulator periods that are typically in the cm-regime photon wavelengths down to the Å-range can be reached [46]. It has to be noted that eq. (3.12) can also be solved by odd higher harmonics of the photon wavelength $\left(\frac{\lambda_{ph}}{3}, \frac{\lambda_{ph}}{5}, \ldots\right)$. These higher-harmonics are in fact produced in FELs and certain countermeasures have to be taken to suppress them if a monochromatic spectrum is desired.

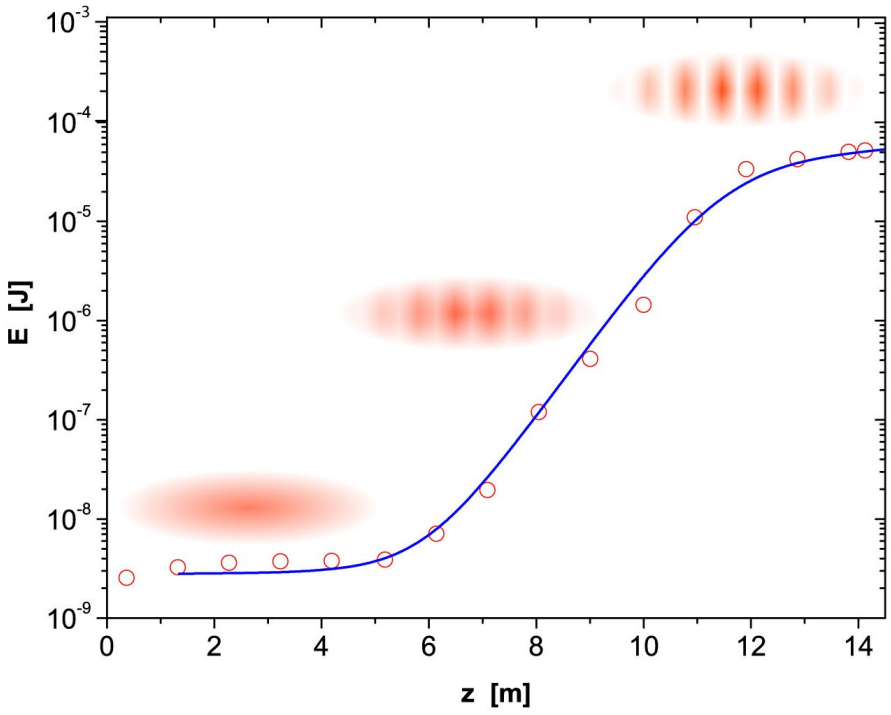

Figure 3.3.: The back-action of the light field onto the electron bunches leads to the production of so-called microbunches. Each of these microbunches in the following emits as a single particle, which leads to the efficient amplification of the FEL radiation. A more detailed description of this process can be found in the main text. Figure reprinted from [48].

3.3. Microbunching

For lasers in general an optical cavity is a crucial component and the quality of this resonator directly affects the performance of the laser. For FELs in the optical or terahertz regime resonators exist and are used. They are called low-gain FELs because in each pass through the undulator the light field is only weakly amplified. As stated before, it is highly demanding to manufacture high quality optics for the XUV spectral range. It is therefore not possible to build an optical resonator that fulfills the technical requirements for a laser with reasonable effort. Therefore, another mechanism has to be found that guarantees sufficient amplification of light in an XUV FEL. Due to the lack of a resonator the light field has to be amplified in a single pass through the undulator. FELs operated in this way are called high-gain FELs.

To reach high amplification of the light field an electron beam with a high bunch charge is fed into the undulator. The problem in doing so is that Coulomb repulsion

will make this electron bunch unstable, as well as massively impact its size. This leads to an electron bunch that is large compared to the light wavelength which prevents the coherent buildup of light intensity. Fortunately the effect of microbunching solves this issue. It can be seen from eq. (3.6) that the z-component of the electron velocity is not constant but oscillates. This modulation leads to the aggregation of electrons at regions with maximum energy transfer to the light field [cf. Eq. (3.11)]. An intuitive picture is that fast electrons are slowed down due to high energy transfer to the light field, while slow electrons are accelerated due to the opposite process. Each individual microbunch now acts as a single particle with charge Ne. This enables the efficient amplification of radiation in a coherent manner. The intensity of the light field is proportional to the square of the number of electrons in each microbunch: $I \propto N^2$. In contrast to this in a synchrotron facility the electrons act as individual particles and the intensity simply scales with N. Due to the high amplification of the light field the microbunching gets ever more efficient. The intensity inside the undulator grows exponentially with the length, as does the degree of microbunching [48, 50] (see Figure 3.3):

$$I(z) \propto e^{\frac{z}{L_g}}. \tag{3.14}$$

Here L_g is the so-called gain length of the undulator. The light intensity saturates when the microbunches are fully developed. A longer propagation in the undulator in fact decreases the intensity again. It is therefore crucial to choose a suitable undulator length [46, 48].

3.4. FEL start-up and self-amplified spontaneous emission

The start-up of an FEL can be initiated in several ways. It is possible to use an external light source to seed the initial photon beam via an optical laser [51]. In principle a high-harmonic source which directly provides seeding light in the XUV spectral range can also be used [52]. However it is technologically very challenging to translate these techniques to the Å-spectral range. Another way to initiate the FEL operation is to exploit self-amplified spontaneous emission (SASE). One way to picture this process is the following: The electron beam in the undulator spontaneously generates white noise radiation of which one Fourier component that fulfills the phase matching condition (3.13) is amplified. The wavelength of the amplified radiation

can be tuned via the undulator parameter K. In practice the electron beam's kinetic energy and the undulator gap width is used. An elegant way to initiate lasing in an FEL is to use so-called self-seeding [53]. Here, in the first part of the undulator, lasing is initiated via the SASE process. This light is then monochromatized and subsequently used to seed the rest of the undulator. In this way amplification of only one single wavelength can be obtained.

The experiments described in this work were performed at the SASE-FEL FLASH which in its normal mode of operation uses the SASE process to obtain lasing. Additionally, the broader bandwidth of SASE FELs, in comparison to seeded FELs, is beneficial for the performed transient absorption spectroscopy experiments. Therefore, the properties of SASE pulses will be delineated in more detail in the following. In Figure 3.4 several single-shot detected SASE spectra are shown (colors) together with the average FEL spectrum (black), averaged over 10000 FEL shots. The individual

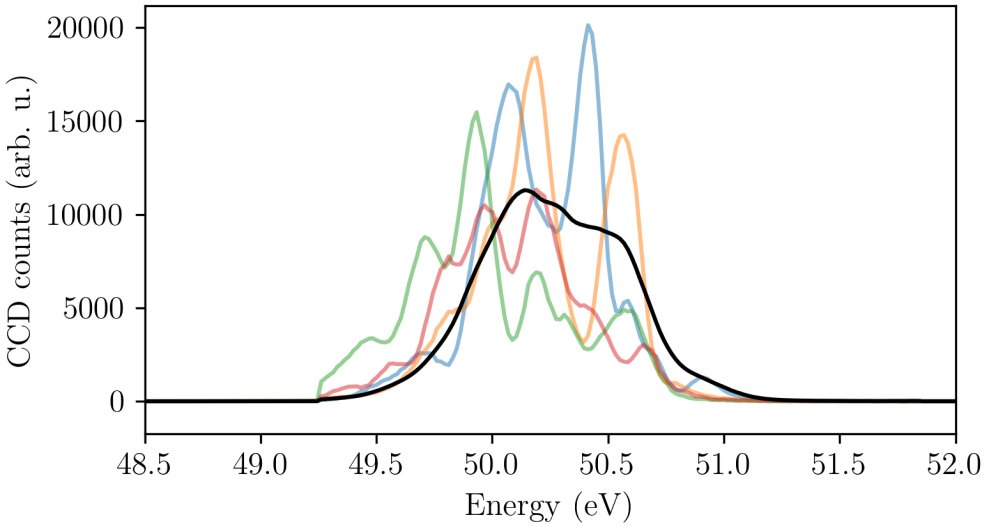

Figure 3.4.: SASE spectra from individual FEL pulses as used in this work (colored). Averaging over several hundred FEL shots results in the average spectrum of the FEL (black), which is proportional to the undulator gain curve of the FEL.

SASE shots show a random distribution of multiple spikes. This is due to the inherent stochastic nature of the generation process of the SASE pulses that starts from shot noise. These pulses therefore are best described by chaotic light. Shot-to-shot fluctuations can not only occur in the position and number of spikes but also in central wavelength, pulse energy and bandwidth which is why great care has to be taken when analyzing SASE FEL data. The average SASE FEL spectrum follows the

gain curve of the FEL which has a nearly Gaussian shape. An important measure for SASE pulses is the coherence time $\tau_{\text{coh.}}$. In general, the correlation function reads:

$$g(t-t') = \frac{\langle E(t)\rangle\langle E^*(t')\rangle}{\left|\langle E(t)\rangle\right|^2} = \frac{\int \left|\langle \tilde{E}(\omega)\rangle\right|^2 \exp\left[-i\omega(t-t')\right] \mathrm{d}\omega}{\int \left|\langle \tilde{E}(\omega)\rangle\right|^2 \mathrm{d}\omega}. \tag{3.15}$$

Inserting the electric field

$$\tilde{E}(\omega) \propto \exp\left(-\frac{\omega}{\sigma_\omega}\right), \tag{3.16}$$

which is proportional to the FEL gain curve and, therefore, of Gaussian shape, yields the correlation function:

$$g(t-t') = \exp\left(-\frac{\sigma_\omega^2 (t-t')^2}{2}\right). \tag{3.17}$$

From this the coherence time of the SASE pulses can be calculated:

$$\tau_{\text{coh.}} = \int (g(t))^2 \,\mathrm{d}t \approx \frac{\sqrt{\pi}}{\sigma_\omega}. \tag{3.18}$$

From the coherence time one can assess the average number of spikes in the SASE spectra. For an electron bunch of duration T_{bunch} the average number of spikes is:

$$N_{\text{spikes}} = \frac{T_{\text{bunch}}}{\tau_{\text{coh.}}}. \tag{3.19}$$

The spectral width of an individual spike then is:

$$\Delta\omega_{\text{spike}} = \frac{2\sqrt{2\ln 2}}{T_{\text{bunch}}}. \tag{3.20}$$

3.5. The Free-electron LASer in Hamburg (FLASH)

The layout of the SASE **F**ree-Electron **LAS**er in **H**amburg (FLASH), where the experiments described in this work were performed, is depicted in Figure 3.5. It was the world's first FEL reaching the XUV and soft-x-ray spectral range and is operational since 2005.

A gun laser with sub-ps pulse duration generates short electron bursts with a charge of up to 200 pC. It is possible to generate electron bunch trains with an intra-bunch repetition rate of up to 1 MHz and an inter-bunch repetition rate of 10 Hz [55]. All

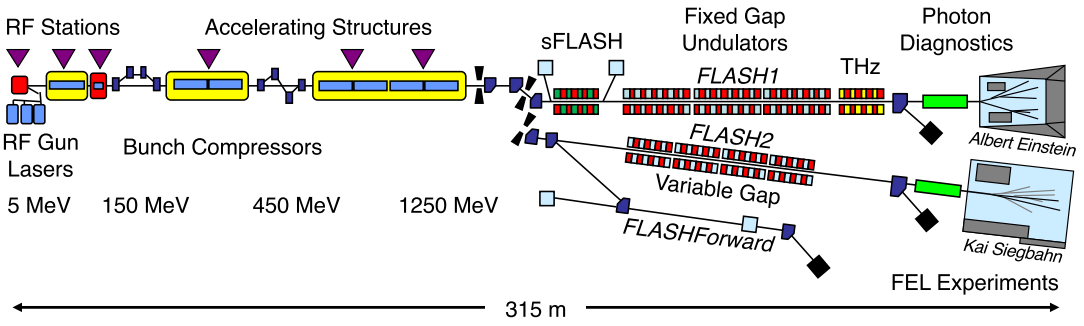

Figure 3.5.: Layout of the FEL FLASH and its beamlines [54].

Table 3.1.: Parameters of the FLASH1 undulator [57]. Additional details can be found in [58].

FEL parameter	**typical**	**this work**
Pulse energy (µJ)	1 . . . 500	45
Pulse duration (FWHM) (fs)	30 . . . 200	65 ± 15
Wavelength (nm)	4.2 . . . 51	24.5
Photon energy (eV)	14 . . . 295	50.6
Spectral bandwidth (FWHM)		
(% of central photon energy)	0.7 . . . 2	1.5
Inter-bunch repetition rate (Hz)	10	10
Intra-bunch repetition rate (kHz)	40, 50, 100, 200, 250, 500, 1000	—
Photons per pulse	$10^{11} \ldots 10^{14}$	10^{13}

of the experiments described in this work were performed in the single-bunch mode that provides 1 electron bunch every 100 ms. This directly translates into a repetition rate for the light pulses of 10 Hz, which allows for the detection of the experimental spectra on a single-shot basis.

The electron bunches are accelerated in a superconducting linear accelerator to energies of up to 1 GeV and temporally compressed via chicanes that guide faster electrons on a longer trajectory. The compressed electron bunches are then fed into one of two undulators (FLASH1 and FLASH2) to generate XUV/ soft-x-ray light of femtosecond pulse durations (see sections 3.1-3.4). The two undulators can even be operated in parallel [56]. The typical beam parameters of the FLASH1 undulator that was used in this work are summarized in Table 3.1.

3.5.1. FEL pulse energy measurement

The pulse energy of the FEL pulses can be measured via the ionization they introduce in a dilute gas medium in a so-called gas-monitor detector (GMD). On its path through the ionization chamber an FEL pulse ionizes a gas target (see Figure 3.6). The number of produced ions is directly proportional to the number of photons and thereby the pulse energy:

$$N_{\text{ions}} = N_{\text{photons}} \cdot \sigma \cdot \rho l, \tag{3.21}$$

where N_{ions} is the number of produced ions, N_{photons} is the number of photons in the pulse, σ is the photoionization cross section and ρl is the pathlength-density product. The produced ions and electrons are accelerated in an electric field and detected

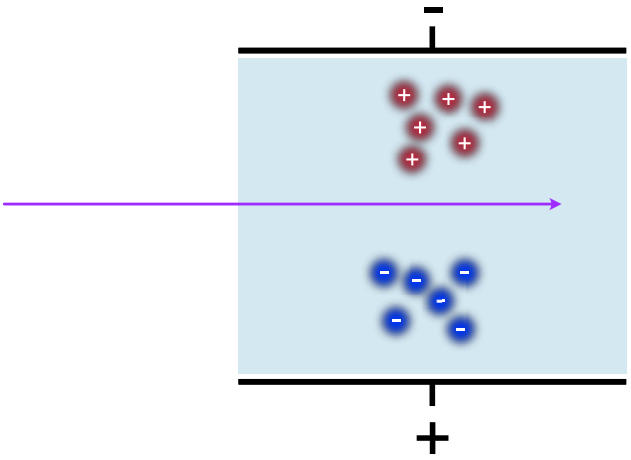

Figure 3.6.: Working principle of the gas-monitor detector (GMD) used to measure the FEL pulse energy at FLASH. The FEL beam travels through a chamber filled with a dilute gas, ionizing the gas on its passage. The number of produced ions is proportional to the number of photons in an FEL pulse and thereby the pulse energy.

by Faraday cups. The measured current is proportional to the absolute number of photons in an FEL pulse which can in this way be determined with an accuracy of 10 % [59]. In addition to the Faraday cups, position-sensitive detectors are installed to measure the pointing of the FEL beam. An example for the fluctuations in pulse energy during one typical experimental run can be found in Figure 3.7. As can be seen the pulse energy roughly fluctuates between 0 and 80 µJ with a mean value of 48 µJ and a standard deviation of 13 µJ, which are typical values for a SASE FEL.

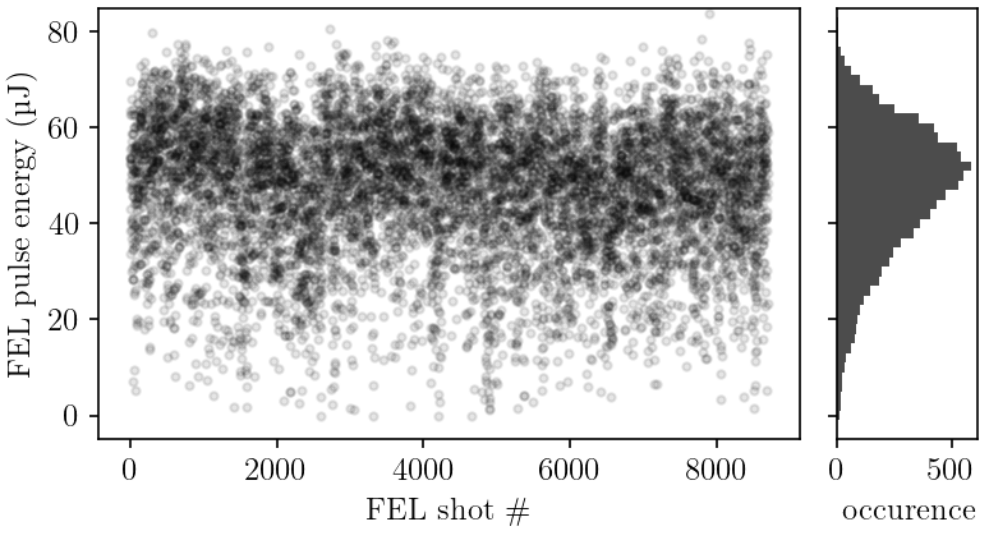

Figure 3.7.: Pulse energy fluctuations as measured by the GMD during one experimental run.

3.5.2. Online reference spectrometer

The stochastic nature of SASE pulses furthermore leads to fluctuations in wavelength and spectral shape of every individual FEL pulse (see Figure 3.4). To be able to determine the absorbance of an investigated target it is important to have a reference spectrum:

$$\mathrm{OD} = -\log_{10}\left[\frac{I_{\mathrm{signal}}(\omega)}{I_{\mathrm{reference}}(\omega)}\right].$$

For SASE pulses, this reference differs from pulse to pulse. Therefore, it is important to record reference spectra on a shot-to-shot basis. For this purpose an online reference spectrometer is available at FLASH [60] (see Figure 3.8). One beamline mirror is hereby replaced by a variable line spacing (VLS) grating. It acts as a plane mirror for the zeroth order reflection that is propagated further downstream to the experiment, while the first diffraction order is dispersed by the VLS grating and detected on a CCD-camera chip. The SASE spectra in Figure 3.4 are detected with this spectrometer.

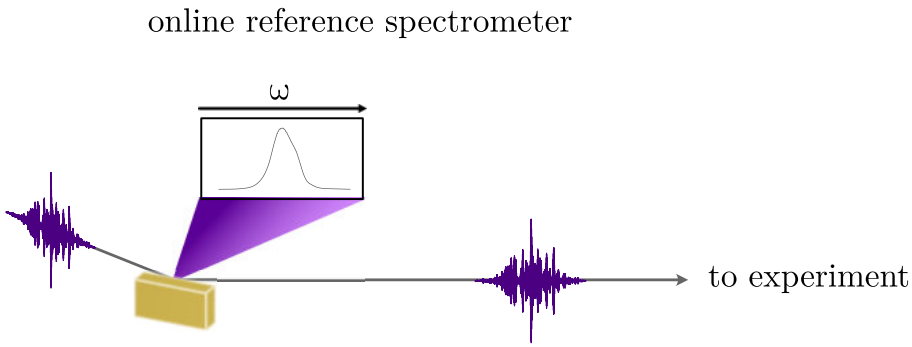

Figure 3.8.: Online reference spectrometer. To measure a reference of the incoming FEL beam, one beamline mirror is replaced by a variable line-spacing grating. For the zeroth order reflection, which is propagated further downstream to the experimental setup, this grating acts as a plane mirror. The first diffraction order is detected on a CCD-camera. These references can be recorded on a single-shot basis.

4. Experimental setup

In this chapter, a detailed description of the home-built experimental setup and how it is implemented at the FEL beamline is given.

A short overview over the entire FEL beam path on its way through the instruments of the FEL beamline (red box in Figure 4.1, see section 3.5) and the experimental setup (blue box in Figure 4.1, see sections 4.2 - 4.4) will be given here. The FEL

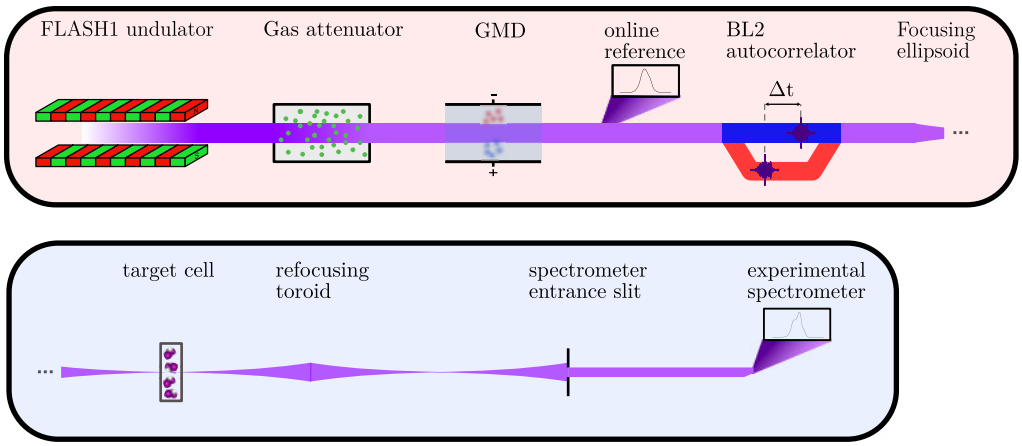

Figure 4.1.: Scheme of the entire FEL beampath. The section in the red box belongs to the FEL beamline, while the section in the blue box belongs to the home-built experimental setup.

beam is generated in the FLASH1 undulator with a pulse repetition rate of 10 Hz. It passes a gas attenuator, which is a long tube filled with a specifically chosen gas. The gas pressure can be precisely controlled via a computer-controlled needle valve. The type of gas is chosen in such a way that it has a nonresonant absorption cross section at the photon energy of the used XUV radiation. In this way the intensity of the FEL beam can be fine-tuned. The realized intensity is subsequently measured in a gas monitor detector (GMD, see section 3.5.1). A reference spectrum of the FEL beam is recorded on a shot-to-shot basis via the FLASH online reference spectrometer [60] (see section 3.5.2). The FEL pulses are then geometrically split into two parts in the FLASH BL2 autocorrelator [61] (see section 4.2). A time-delay between the

hereby generated pump and probe pulses is introduced by varying the optical path length of one of the pulses. Pump and probe beam are separated in space after the autocorrelator. The partial beams are focused into the experimental setup by an ellipsoidal mirror with a focal length of $f = 2\,\mathrm{m}$ to a focus size of $\sim 25\,\mu\mathrm{m}$, where the beams cross in the target cell. Therefore, pump and probe pulses are in spatial overlap in the target (see section 4.3). In the far field pump and probe beams are spatially separated, again. The transmitted pump and probe spectra can therefore be recorded on the same CCD-camera chip with a spatial offset.

4.1. Overview over the home-built experimental setup

The experimental apparatus presented in this work was designed with the goal to perform experiments using a combination of octave-spanning optical light (VIS), near-infrared (NIR) radiation, extreme ultraviolet (XUV) light from high-harmonic generation (HHG) sources, as well as free-electron lasers (FELs). The experiments described in this work are all-XUV pump–probe experiments using the Free-electron LASer in Hamburg (FLASH) as a source. Therefore, the description of the setup has its focus on the parts used for this kind of experiments. The all-XUV pump–probe transient absorption spectroscopy described in this work is based on the geometric splitting of the incoming FEL pulse into a phase-locked pulse pair. The hereby created pump and probe pulses are delayed in time with respect to each other and focused into the target where they spatially overlap. The absorption spectrum of the probe pulse (as well as the pump pulse) are detected as a function of the pump-probe time delay. Changes in the target's probe absorption spectrum are related to dynamical processes triggered in the target medium by the pump pulse.

The experiments described in this work were performed at beamline BL2 of the FLASH1 undulator (see section 3.5). This beamline can provide an already focused FEL beam through insertion of a focusing ellipsoidal mirror ($f = 2\,\mathrm{m}$) into the beam path. Additionally, an online reference spectrometer [60] can be used which provides a reference spectrum of the FEL beam before it enters the user experiment on a shot-to-shot basis (see section 3.5.2). The option to insert a split-and-delay unit (SDU) for pump–probe experiments provides a large flexibility for user experiments (see section 4.2).

The home-built experimental setup consists of multiple vacuum chambers, each containing one key part of the experiment. The individual parts will be discussed

in more detail in the following sections. An overview of the setup can be found in Figure 4.2 with a photograph of the setup as used at FLASH in Figure 4.3. The main chambers are depicted in light grey, while the smaller chambers containing diagnostics are shown in a darker shade of grey.

The focused FEL beam enters the experimental setup from the right. After passing a differential pumping stage and a diagnostic chamber containing apertures for the fixation of the beam pointing, its focus lies in the center of the target chamber. In the target gas cell (see section 4.3) the beam interacts with the target medium. Having passed the second diagnostic chamber, the beam enters the mirror chamber where the beam is rerouted by a toroidal mirror and a split-mirror. The toroid makes a $2f$–$2f$ image of the first focus into an empty vacuum chamber. When the experimental setup is operated with a HHG source, this is where the target cell is positioned. For the FEL experiments discussed here it is kept empty. This design allows the operation with either an HHG or an FEL source without a major redesign of the setup. Subsequently the beam enters the experimental spectrometer. It consists of 2 chambers and a translation mount for the CCD camera detector. In the first spectrometer chamber, the adjustable entrance slit is placed. In the following main spectrometer chamber, a metal filter array for the attenuation of the FEL beam, as well as the dispersive reflection grating are placed. The dispersed light is detected by an XUV-sensitive CCD camera. A more detailed description of the spectrometer can be found in section 4.4.

The highly intense XUV FEL beam can significantly ionize the residual gas in the vacuum chambers, which would damage the uncoated XUV optics inside the setup and lead to scattering losses of the XUV radiation. Therefore, differential pumping stages are installed between the chambers to limit the molecular conductance between them. This is important since the pressure in the target chamber frequently reaches the 10^{-3} mbar regime while performing experiments. The differential pumping stages ensure that UHV conditions with chamber pressures well below 10^{-8} mbar are maintained in adjacent chambers. This is realized by connecting the vacuum chambers via oblong metal tubes. The tubes have lengths of 100 mm with diameters of 5 and 10 mm depending on where they are placed along the path of the converging/diverging FEL beam. They can be seen at the intersections of individual vacuum chambers in Figure 4.2. Turbo-molecular pumps with speeds of $300\,\mathrm{l\,s^{-1}}$ and $2000\,\mathrm{l\,s^{-1}}$ on every vacuum chamber are used to keep the UHV conditions stable under the high experimental gas loads.

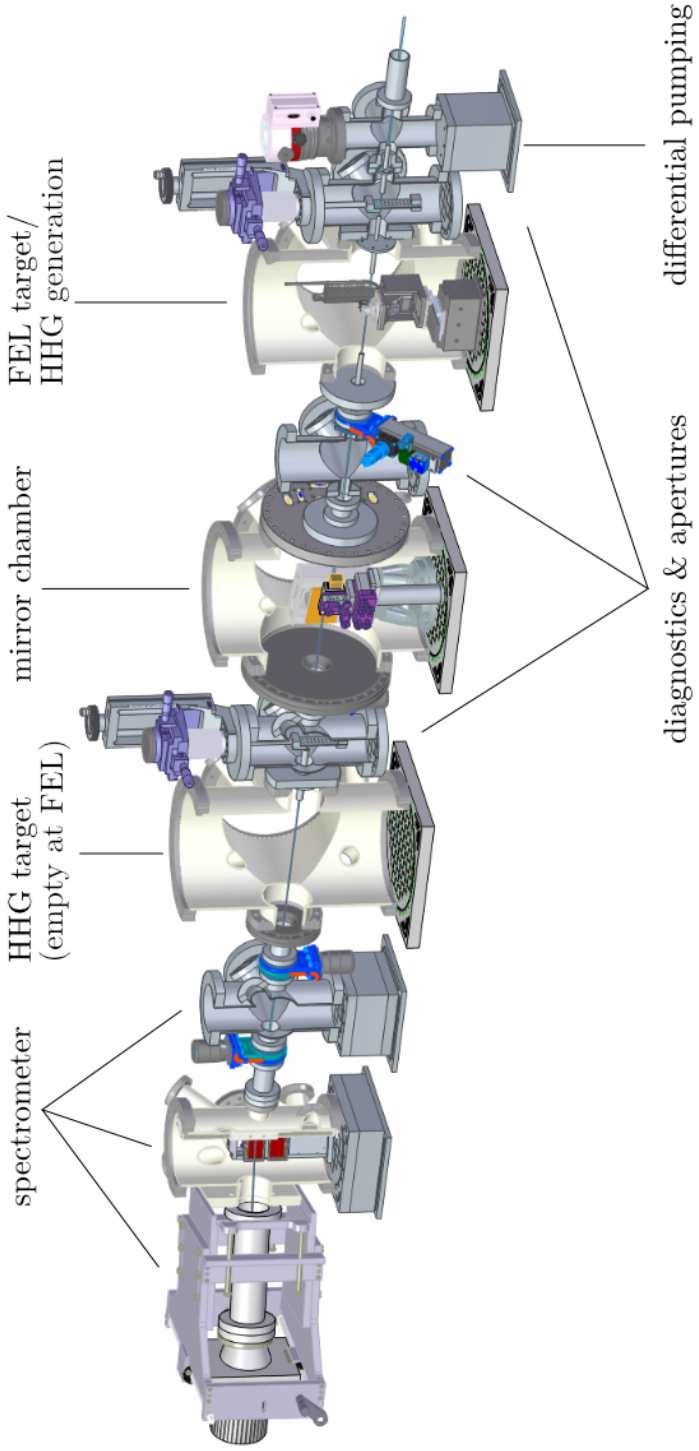

Figure 4.2.: Cut through the experimental setup. Having already passed the FLASH beamline BL2 autocorrelator (see section 4.2) and the focusing ellipsoidal mirror, the FEL beam enters the setup from the right. After passing a differential pumping stage and a diagnostic chamber, the focus of the FEL is in the center of the FEL target chamber. Here, the heated target cell (see section 4.3) is positioned. The beam passes several additional diagnostic chambers and is refocused by a toroidal mirror placed inside of the mirror chamber (see section 4.5). The second focus of the FEL is in the empty HHG-target chamber. The FEL spectra are recorded in a home-built high-resolution spectrometer (see section 4.4).

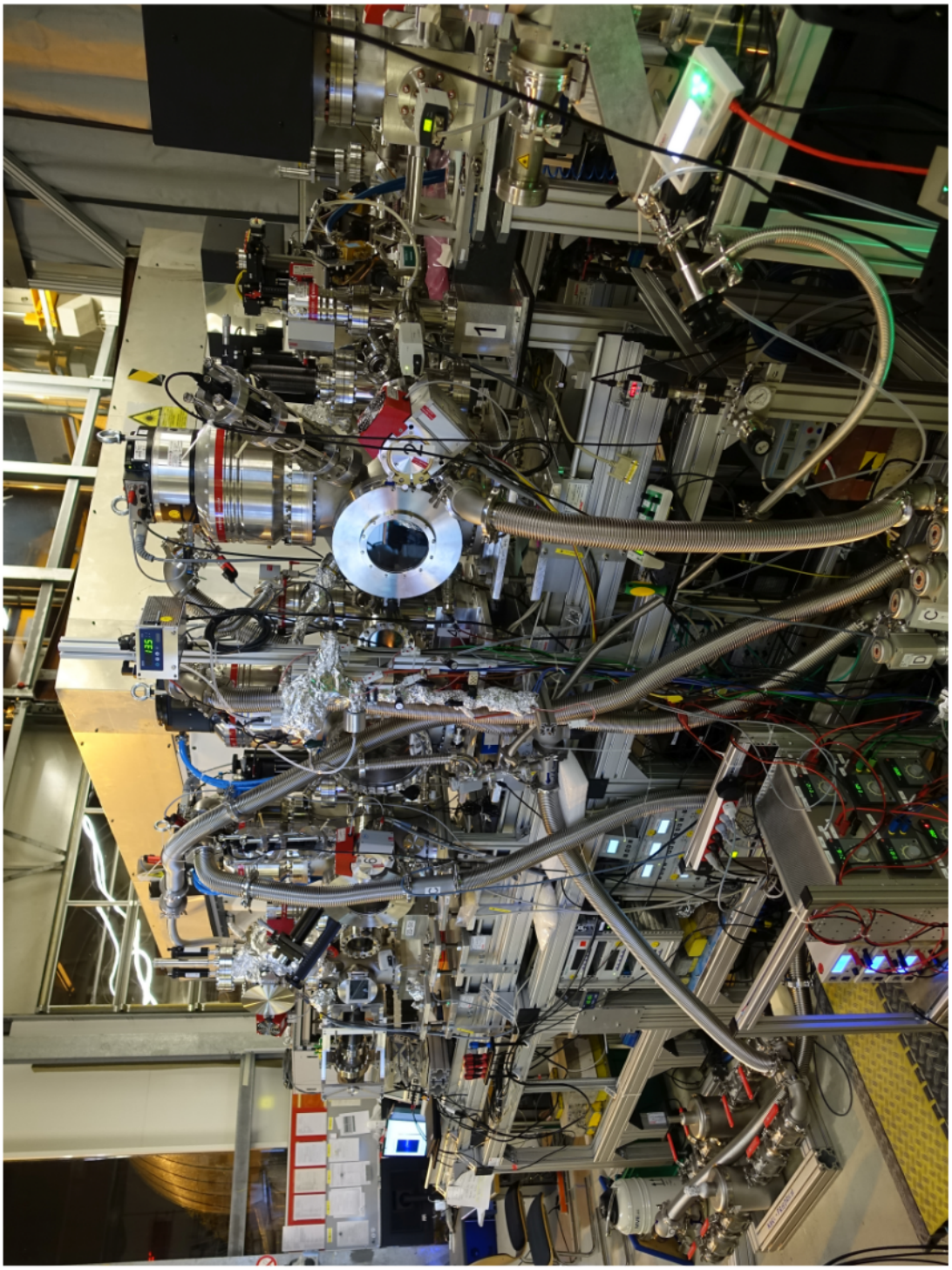

Figure 4.3.: Photograph of the experimental setup as installed at FLASH.

4.2. The FLASH beamline BL2 autocorrelator

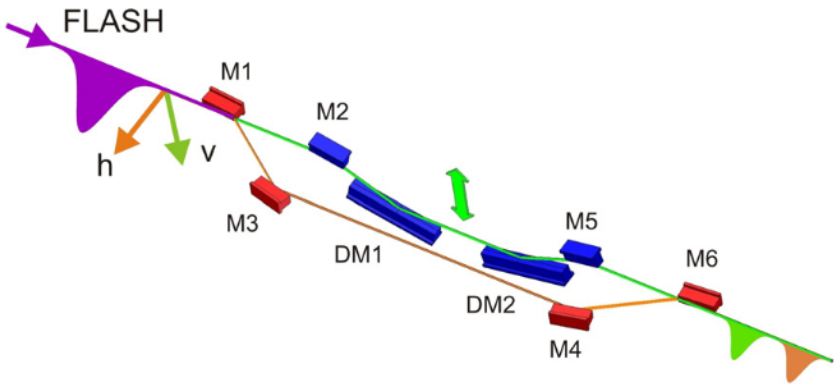

Figure 4.4.: Sketch of the FLASH beamline BL2 autocorrelator. The incoming FEL pulses are split into two pulses by mirror M1. The hereby generated pump and probe pulses travel over different arms of the interferometer. The mirrors of the fixed beam path are depicted in red, while the mirrors belonging to the variable beam path are depicted in blue. The optical path length of the variable path can be altered by translating mirrors DM1 and DM2 simultaneously. The two beam parts are recombined via mirror M6. Figure reprinted from [61].

The FLASH beamline BL2 autocorrelator is a split-and-delay unit (SDU) based on a Mach-Zehnder-type interferometer. It includes 8 carbon coated mirrors hit under grazing incidence angles of 3° for the fixed beam path (marked in orange in Figure 4.4) and 6° for the variable beam path (marekd in green in Figure 4.4) to expand the total delay range. The incoming FEL beam is geometrically split into two parts by a mirror only partially inserted into the beam path (mirror M1 in Figure 4.4). The fixed beam path is depicted in red in Figure 4.4 while the variable beam path is depicted in blue. Due to the different reflection angles, the two autocorrelator paths have different transmissions for XUV radiation. For the 50 eV radiation used in this work, the autocorrelator has a transmission of $\sim 70\,\%$ in the fixed beam path and $\sim 60\,\%$ in the variable beam path. Furthermore, the splitting ratio between fixed and variable beam path can be altered via mirror M1. A splitting ratio of roughly 2:1 between fixed and variable beam path was chosen for the experiments in this work.

Moving the delay stage consisting of mirrors DM1 and DM2 introduces as delay between the two split FEL pulses before the beam is recombined at mirror M6. A total delay of 18 ps between the split pulses can be introduced with sub-fs resolution and an interferometric stability of 0.28 fs [61]. To compensate for possible misalignment of the beam pointing, closed-loop piezo tilt-actuators are installed at the mirrors DM1 and

DM2. Unfortunately, the feedback loop for the delay stage was out of order during our measuring campaign. Therefore, the absolute delay position had to be measured independently. The temporal overlap of the split pulses defines the experimental time zero. It could be determined with an accuracy better than 10 fs via an autocorrelation measurement in neon [62] (see section 5.1).

4.3. The heated target cell

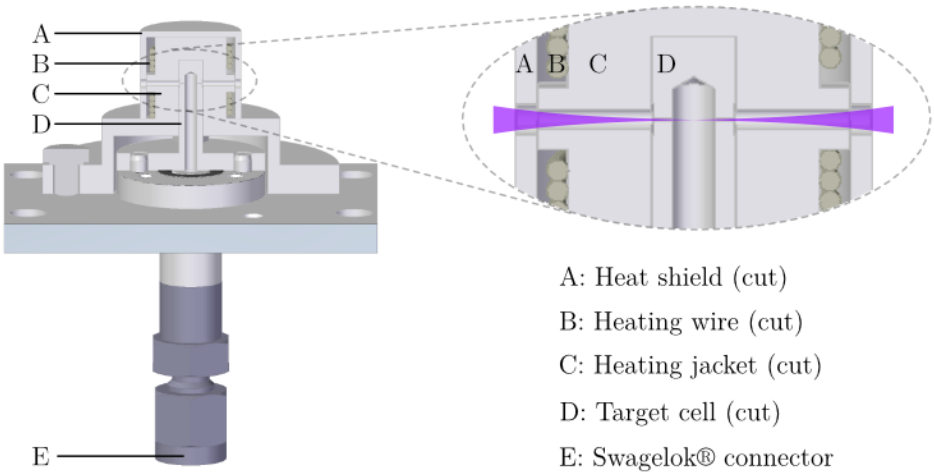

Figure 4.5.: Cut through the heated target cell. A: heat shield, which protects other equipment in the vicinity of the target cell from heating up. B: Heating wire. C: Heating jacket. This enables the exchange of target cells without the need to rewrap the heating wire. D: Target gas cell. E: Swagelok® connector to connect the gas cell to the heated feeding line.

The absorption of light in a medium is directly related to its density. In order to reach sufficiently high target densities and at the same time retain the vacuum conditions required for FEL operation, a target gas cell is designed that can be operated at target pressures of several tens of mbar while keeping the pressure in the surrounding vacuum chamber in the 10^{-4} mbar range. Pinholes are drilled through the cell's front and backside along the optical axis which allow focusing the FEL beam into the cell without it being attenuated by window material to obtain maximum on-target intensities. Depending on the experiment's requirements, cells with pinhole diameters of 100 µm, 200 µm or 300 µm can be chosen. This cell design has a typical leak rate on the order of 0.1 mbar l s^{-1} when operated at target pressures in the 10 mbar regime. The FEL beam can be focused down to $\sim$ 25 µm using the beamline BL2 ellipsoidal

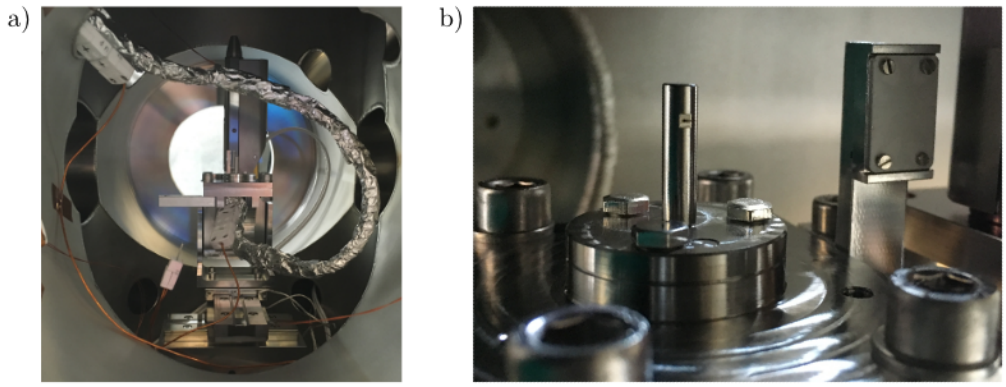

Figure 4.6.: Foto of the heated target cell. a) Overview inside the vacuum chamber. The heated flexible gas feeding line can be seen in the foreground wrapped in aluminum foil. b) Closeup with the heating jacket removed. Next to the target cell, a screen coated with fluorescent material can be seen. It is used for alignment purposes of the FEL beam and can be monitored with a microscope objective from outside the vacuum chamber.

mirror which is small enough to avoid significant clipping of the beam at the edges of the pinholes. The target cells can be manufactured in stainless steel, which is mostly used for FEL experiments, or the glass ceramic MACOR® that provides much better resistance to laser ablation when using optical lasers. For the transient absorption experiments in molecular targets performed at FLASH, target cells made of stainless steel with hole diameters of 200 µm were used. A specialty of this cell design is the possibility to heat it in a controlled fashion using multiple sections of PI-controlled heating elements. This enables to perform experiments with targets that are liquid or even solid at room temperatures by gently heating them. Vapor pressures on the order of 10 mbar can be reached in this way which is sufficient for transient absorption experiments. A heat gradient has to be realized which starts with the sample reservoir as its coldest point and ends with the target cell as the hottest point to avoid condensation of the sample along the supply line. Additionally, clogging of the cell's pinhole by polymerized target molecules is reduced in this way. Individual sections of the setup are wrapped in separate loops of heating wire. Measuring resistors of the Pt100 type deliver the feedback for the PI control loop. A sketch of the heated gas cell can be found in Figure 4.5. Shown are the Swagelok® connector that connects to the heated gas supply line (E), a cut through the target cell itself (D), the heating jacket (C) with heating wire (B) and the heat shield (A) which prevents surrounding equipment from heating up. A photograph, showing the vacuum side of the target cell system (left panel) and a close-up of the target cell (right panel) can be found

in Figure 4.6. Next to the target cell a fluorescent screen is mounted (see Figure 4.6 b)) which lights up under irradiation of XUV light and is used for alignment of the FEL beam. The entire target cell system can be moved via a closed-loop motorized XYZ-manipulator with sub-µm repeatability.

4.4. The flat-field XUV spectrometer

The home-built experimental spectrometer is based on a concave reflective grating, optimized for a grazing incidence angle of 4.7°. The groove density of the grating varies along the optical axis (variable line spacing, VLS), which, together with the concave grating substrate, ensures the imaging of the first diffraction order onto a flat focal plane[1]. The used grating is specified for a spectral range of 20 eV to $\sim$ 113 eV (11 nm to 62 nm), which is imaged onto a focal plane of 110 mm width [63]. Placed in the focal plane is an XUV-sensitive back-illuminated CCD camera [64] with a chip of 1340 × 400 pixels of size 20 µm × 20 µm to detect the dispersed light. The camera can be moved along the focal plane by a home-built mechanical bearing [65]. The spectrometer can in principle be operated with the target cell acting as its entrance slit. This ensures highest possible transmission of light which can be crucial for experiments with low-intensity HHG radiation. In the case of FEL experiments with very high photon flux an additional motorized 2D-slit [66] was installed. The slit has two orthogonal pairs of metal blades forming an adjustable rectangular aperture. One blade pair acts as a tunable entrance slit that allows for the optimization of the spectrometer's resolution, while the other blade pair adds the flexibility to partially block the incoming beam. This makes it possible to record only the spectra of either probe or pump beam, while blocking the other. After optimizing the alignment of the spectrometer, its resolution was determined to be $\lambda/\Delta\lambda \approx 1500$ during the experiments described in this work by using absorption resonances in Ne^{2+} ions [62]. Due to the high photon flux of the FEL radiation employed in this work the incident FEL beam has to be attenuated as not to saturate or even damage the CCD camera chip. For this purpose an array of aluminium and zirconium foils of thicknesses ranging from 200 nm up to 4 µm is installed to partially absorb the XUV radiation. Selecting a suitable combination of these metal foils is crucial to ensure

[1] The focal plane of a spectrometer based on a conventional grating lies on the so-called Rowland circle. This leads to the loss of resolution at the edges of a flat detector. Additionally, a complex mechanical bearing has to be used to ensure movement of the detector on a perfect circle, or the grating has to be rotated.

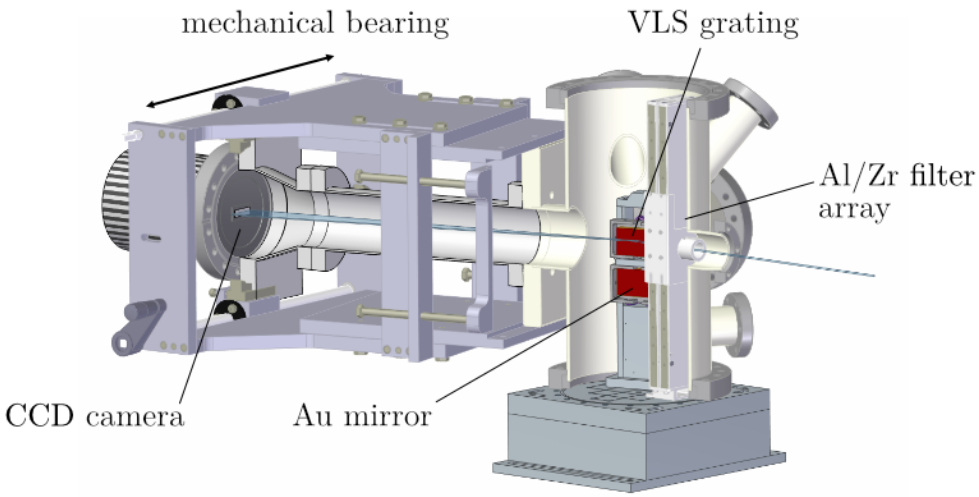

Figure 4.7.: Sketch of the home-built experimental spectrometer. The FEL beam enters the spectrometer through the entrance slit (not shown). It is attenuated via an array of aluminum and zirconium filters and dispersed by a flat-field grating. The dispersed light is detected by a CCD camera chip. This camera can be moved along the focal plane of the grating to detect different spectral regions.

that the entire dynamic range of the CCD camera chip of 16 bit is utilized without saturating the chip. The grating mount can be moved in the vertical direction using a stepper motor. It is in this way possible to switch to a different grating with another groove density. For the presented experiment, the second grating was swapped for a plane gold mirror. This enables monitoring the direct reflection of the FEL beam on the CCD camera which helps with the alignment of the entire setup.

4.5. The home-built split-and-delay unit and upgrades for the experimental setup

As described in the previous sections, the pump–probe experiments conducted in this work were performed with the autocorrelator [61] installed at beamline 2 (BL2) at FLASH. However, a split-and-delay unit specifically designed for our experimental setup was originally planned to be used for these experiments. Together with the refocusing toroid, it is located in the mirror chamber of the setup as can be seen in Figure 4.2. Unfortunately, the low surface quality of the toroidal mirror led to significant scattering losses. Therefore, the planned all-XUV pump–probe experiments turned out to be impossible with this device due to the losses after multiple reflections

and the degraded beam quality in the focus. Instead, the experiments were conducted by placing the target cell in the focus of the FLASH ellipsoidal mirror (see Figure 4.1). The pump and probe pulses were hereby generated via the FLASH BL2 autocorrelator as described in the previous sections.

For the experiments presented in this work, the home-built split-and-delay unit was used for the rerouting of the experimental signal into the spectrometer. Therefore, it will be briefly described in the following. It consists of a four-quadrant split mirror

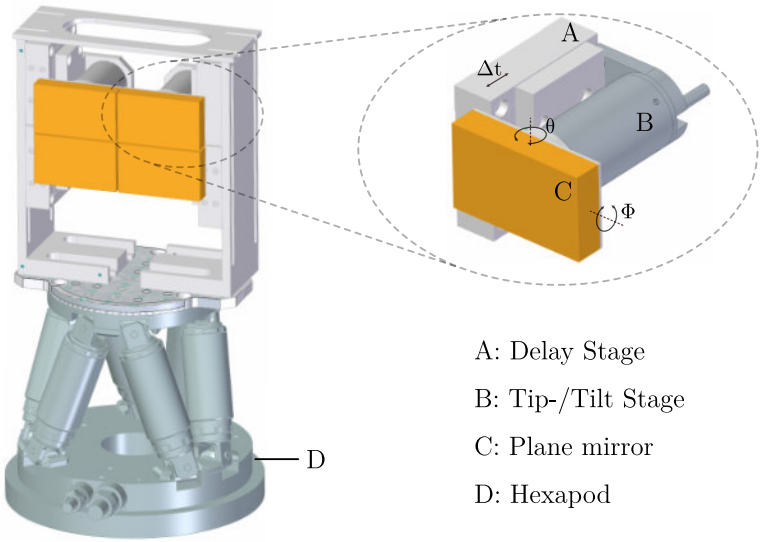

Figure 4.8.: Sketch of the home-built split-and-delay unit. It consists of 4 mirror segments, 3 of which are mounted on a combination of translation and tip/tilt actuators. In this way, complex pulse sequences can be realized. The entire mirror system is mounted on a hexapod 6-axis manipulator, which enables precise alignment under UHV conditions.

system as can be seen in Figure 4.8. The four mirrors are arranged in a 2x2 array, with gaps of $\sim 200\,\mu m$ between the mirrors. The inner edges of the mirror array features no bevels to further minimize the loss of photons. Individual mirror segments are interchangeable, so mirrors of different coatings and dimensions can be used. In this way, the setup can be optimized for experiments at different photon energies and incident angles. For the presented experiments, mirrors with a gold-coated surface of $50\,mm \times 30\,mm$ and a thickness of $10\,mm$ were used. The mirrors are fabricated from high-quality substrates with a flatness of $\lambda/20$ for $\lambda = 633\,nm$ radiation. The surface roughness of the coating is $< 0.2\,nm$ which ensures very low scattering losses. The mirrors possess a reflectivity of $> 50\,\%$ for the spectral range between $20\,eV$ and $110\,eV$ [67] when hit under the incidence angle of 15°.

Three of the mirror segments are mounted on a combination of a piezo-controlled

tip/tilt actuator [68] and translation stage [69]. A total range of 250 µm with a resolution of 0.7 nm steps can be driven with each translation stage. This translates into a total delay range of ~ 850 fs under 15° incidence angle. In theory a step size on the order of 1 as can be realized with these stages, which, in reality, is limited to a temporal resolution of ~ 30 as [70] by the stability of the setup. To determine the interferometric stability of the mirror setup, a frequency-stabilized HeNe-laser is coupled into the vacuum setup. After being reflected by two of the mirror segments, it is coupled out again. Both beam halves are brought into spatial overlap and the emerging interference fringes are detected on a CCD-camera chip. Moving one of the translation stages of the split mirror leads to a shift of these interference finges. Integrating over the area of one fringe while moving the delay stage leads to an interferogram. The phase stability of this interferogram can then be translated into the delay stability of the split mirror setup [70].

The tip/tilt stages are used to compensate for the walk-off that is introduced in the grazing-incidence beam when translating one mirror segment. This is done by moving the translation stages to their two extremal points and both times bringing the partial beams into spatial overlap via the tip/tilt actuators. The settings of the tip/tilt stages at both extremal positions are saved in a spreadsheet. The settings of the tip/tilt stages for the intermediary time delay positions are linearly interpolated. This procedure ensures spatial overlap of all partial beams over the entire time delay range [71]. The 4-quadrant arrangement of the mirrors enables the implementation of a boxcar geometry of the four partial beams [72]. More complex multidimensional pulse schemes can in this way be realized with this setup. The entire mirror setup is mounted on top of a hexapod 6-axis manipulator [73], which enables precise alignment under UHV conditions.

As an upgrade to the experimental setup, the refocusing toroid was replaced with an XUV-grade ellipsoidal mirror with a focal length of $f = 1$ m in succession to the presented experiments. Focus diameters of 10 µm can be reached with this ellipsoid at the FLASH facility, as was measured during later experimental campaigns. In addition, the number of reflections of the FEL beam is reduced by 1, which ensures higher on-target XUV intensities for future experiments.

5. Data processing

The data acquisition of the FEL experiments described in this work are very complex. Not only did we measure the experimental signal spectra on a 10 Hz single-shot basis, but we recorded a large amount of metadata for every incident FEL pulse. This allows to perform a correlated analysis of the experimental signal for different FEL pulse parameters. The raw experimental spectra have to be energy-calibrated and the temporal overlap between pump and probe pulses has to be determined before being able to interpret the observed effects. Therefore, an in-depth look on the acquisition of the experimental data and its calibration is given in this section.

5.1. Calibration of the experimental apparatus

For the calibration of the experimental apparatus an XUV-pump–XUV-probe transient absorption measurement in neon gas is performed. Not only does this experiment give a detailed view into the ionization dynamics of neon under the influence of intense XUV SASE pulses [62], but it provides a good energy calibration of the spectrometer due to the well-known transitions of Ne^{2+}. The absorbance (optical density, OD) of Ne^{2+}, together with the transitions used for its energy calibration can be found in Figure 5.1. The XUV pump pulse doubly ionizes the initially neutral neon target which is subsequently probed by the XUV probe pulse. In addition to the precise energy calibration of the experimental spectrometer the temporal overlap of pump and probe pulses can be determined with an accuracy better than 10 fs due to the coherent enhancement of transmission when individual SASE spikes of the pulses exactly overlap in time [62, 74] (coherent artifact, c.f. Figure 5.2). Furthermore the instrument response function (IRF) of the experiment can be determined from the transient absorption change. In Figure 5.2 the spectrally integrated absorption change of the probe pulse is shown over the course of the time delay. For positive times the pump pulse precedes the probe pulse, thereby bleaching the neon target which results in a lowered absorption of the probe pulse. Fitting an error function to the

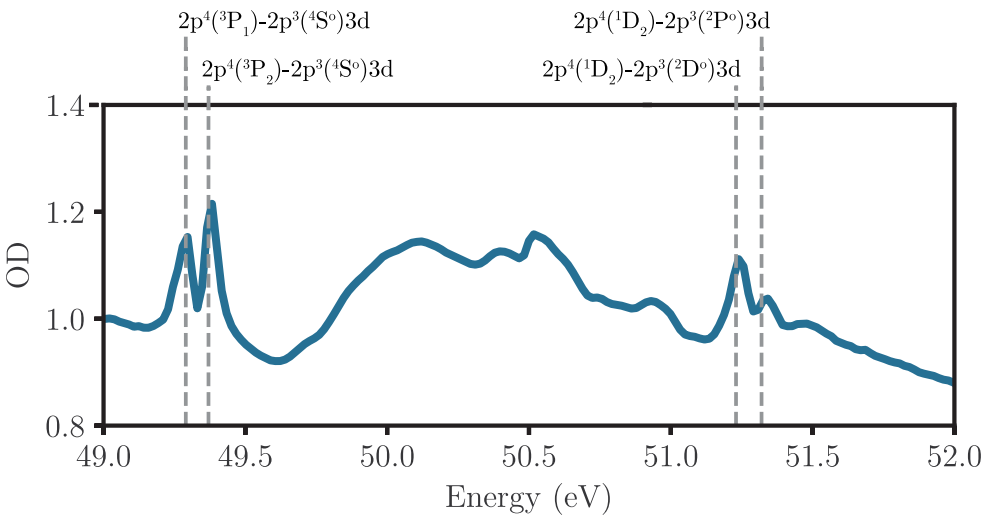

Figure 5.1.: Absorbance (optical density, OD) of a Ne^{2+} target measured in the presented experimental setup. The known energy values of the observed absorption resonances are used for the energy calibration of the home-built spectrometer.

step reveals the width of the IRF of 65 ± 15 fs, which is given by the average duration of the FEL pulses.

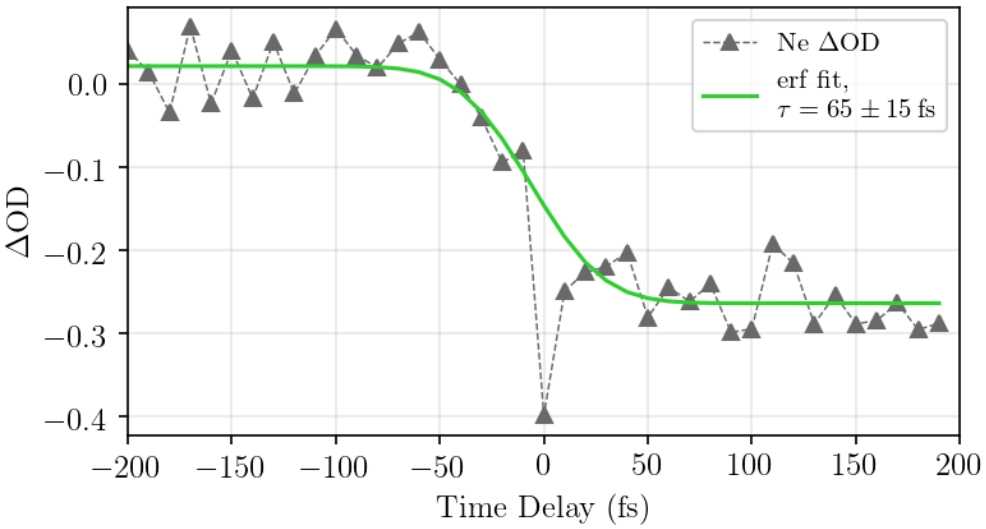

Figure 5.2.: The instrument response function (IRF) of the setup is determined via a second-order autocorrelation in Ne. The temporal overlap of pump and probe pulses is determined via the coherent enhancement of transmission, when the spiky SASE pulses exactly overlap in time [62, 74].

5.2. FEL metadata

The most important FEL parameters for our time-resolved spectroscopy experiments are the pulse energy, the pulse duration and the reference spectrum of every incident FEL pulse. These parameters play an important role in the interpretation of the experimental data and the underlying mechanisms.

The pulse energy of individual incident FEL pulses is measured in a gas-monitor detector (GMD) via the degree of ionization introduced in a gas target [59, 75, 76].

To estimate the FEL pulse duration, a transverse deflection RF structure (TDS) is available at the FLASH facility [77, 78], which measures the electron bunch length of the FEL. This sets an upper bound to the FEL light pulse duration, since only a part of the electron bunch participates in the lasing process. The length of the light pulse was thereby estimated to be 75 fs [79]. This is in good agreement with the duration of 65 ± 15 fs that were directly measured in the interaction region of our experimental setup via a second-order autocorrelation [62] (see section 5.1).

The reference spectra of the incident FEL pulses are recorded on a shot-to-shot basis via the FLASH VLS online spectrometer [60]. In addition to the discussed parameters, the gas pressure in the interaction region as well as the FEL beam pointing, which are important indicators for the stability of the conducted experiments, are recorded. Various further metadata parameters can be measured but play a minor role for this work and are omitted here. For more details on the experimental setup see chapter 4.

5.3. The Bunch-ID

In the FLASH data acquisition system (DAQ) a unique identifier, the so-called Bunch-ID, is assigned to every individual FEL pulse. All of the stored metadata that belongs to an FEL pulse is tagged with this Bunch-ID. In this way, a correlated post-analysis of individual pulse parameters and the experimental signal is possible. To be able to utilize this powerful technique with our home-built experimental setup, the Bunch-ID from the FLASH-DAQ is fed into our data acquisition system and stored together with every individual spectrum. The experimental data can then be post-selected for various incident pulse parameters to look for correlations between the two. Several of these correlations are used in the evaluation of the experimental data, which will be discussed in the following.

5.3.1. Bunch-ID shift-correction

Due to the great complexity of the data acquisition and the high data rate, over time we observed a slippage between the Bunch-ID supplied by the FLASH-DAQ and the Bunch-ID assigned to the recorded experimental spectra. This slippage manifests in a mismatch between the pulse energy measured upstream of the experiment via the FLASH gas-monitor detector (c.f. section 3.5.1) and the total counts recorded in our spectrometer, which are directly proportional to the incident pulse energy (see Figure 5.3). This slippage has to be corrected for, which is an important step in the data evaluation scheme implemented in this work.

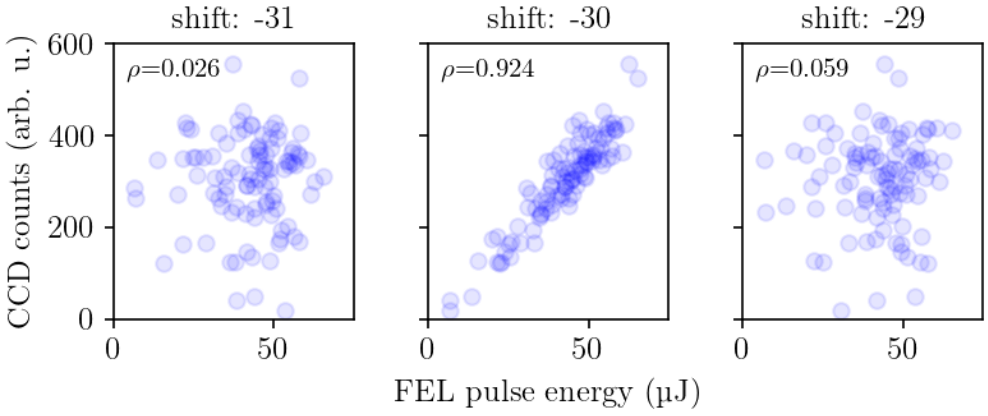

Figure 5.3.: Scatter plots of the incoming FEL pulse energy in µJ measured upstream of the experiment via the FLASH gas-monitor detector and the integrated CCD-camera counts measured in our home-built spectrometer. It can be clearly seen that for the correct Bunch-ID assignment the correlation coefficient ρ is close to 1 (mid panel), whereas for mismatching Bunch-IDs it is close to 0.

Due to the 10 Hz single-shot detection of the experimental spectra, a large amount of data is acquired during one experimental run. This makes a manual correction of the Bunch-ID slippage impractical. Therefore, an automatic script is written which corrects for a possible Bunch-ID mismatch by using the Pearson correlation coefficient ρ between the incoming pulse energy (E_{GMD}) and the integrated CCD-camera counts (N_{CCD}):

$$\rho = \frac{\mathrm{cov}(N_{\mathrm{CCD}}, E_{\mathrm{GMD}})}{\sigma_{N_{\mathrm{CCD}}} \sigma_{E_{\mathrm{GMD}}}}. \tag{5.1}$$

It is equal to ± 1 for positive/negative linear correlation and equal to 0 for the absence of correlation. In Figure 5.3 scatter plots with their corresponding correlation coefficient are shown for different values of a Bunch-ID shift. It is evident that in the mid panel the correlation between incident pulse energy and integrated CCD

counts is very good. Shifting the correct Bunch-ID by ±1 results in the complete loss of correlation. The numbers labeled on top of the panels are the respective shifts in Bunch-ID between the FLASH-DAQ and our data acquisition. As can be clearly seen, the Pearson correlation coefficient is indeed a good measure for the Bunch-ID shift-correction. This procedure is repeated for every single FEL shot within an experimental run. Exemplary results are shown in Figure 5.4. Having corrected for these shifts in Bunch-ID enables the usage of the FLASH online reference spectra that are recorded for every incident FEL pulse.

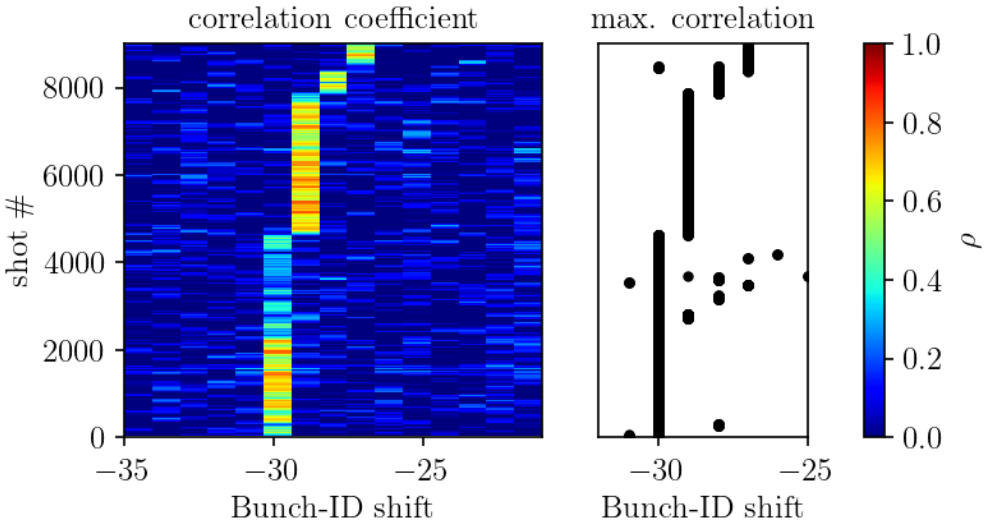

Figure 5.4.: Determination of the correlation maximum between the pulse energy of incident FEL pulses and the integrated counts detected in our setup. This enables the correct assignment of incident FEL pulses and their online reference spectra to the experimental signal detected in our home-built spectrometer.

5.4. Online reference spectra

The reference spectra recorded in the online reference spectrometer at FLASH [60] (see section 3.5.2, Figure 3.8) are used to calculate the optical density of the investigated targets using Eq. 2.17. However, since the reference spectra are recorded in a separate spectrometer with entirely different geometry they have to be calibrated in energy and count-rate to match the experimental spectrometer. To do so, a reference measurement with no target gas in the experimental gas cell is performed.

In the following the naming convention will be based on the names of the CCD cameras of the individual spectrometers, which are PCO for the FLASH online

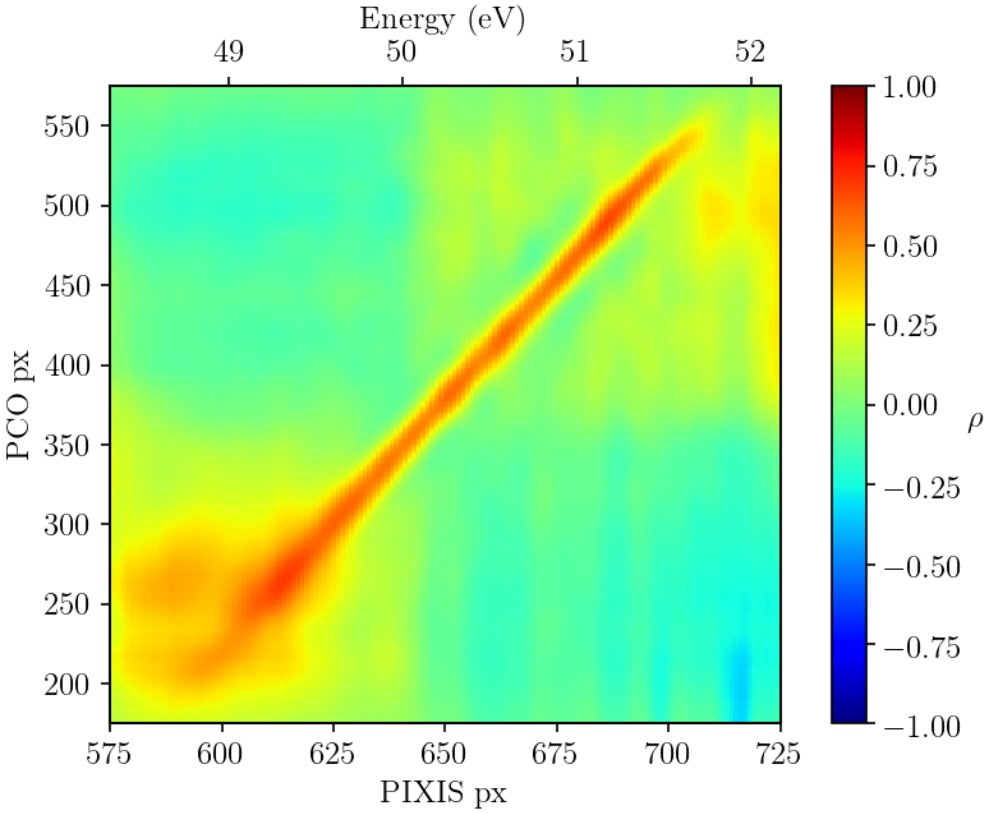

Figure 5.5.: Pearson correlation map calculated according to Eq. (5.2) between online reference spectra (PCO) and spectrum detected in the home-built spectrometer in the absence of a target gas. This enables the energy calibration of the online reference spectra via the correlation maximum

reference spectrometer and PIXIS for our home-built spectrometer. Conventional resampling of the PCO spectra onto the energy-calibrated PIXIS spectra leads to artifacts in the optical density due to the non-vanishing absorption of our experimental apparatus [80]. Therefore, a different method to calibrate the PCO spectra was developed, based on the single-shot detection of the spectra and the correlation between experimental and online reference spectra. The Pearson correlation coefficient is calculated for every combination of pixels (i, j) recorded in the two spectrometers

$$\rho_{ij} = \frac{\mathrm{cov}(N^i_{\mathrm{PCO}}, N^j_{\mathrm{PIXIS}})}{\sigma^i_{N_{\mathrm{PCO}}} \sigma^j_{N_{\mathrm{PIXIS}}}}, \tag{5.2}$$

where $N^{\mathrm{px}}_{\mathrm{S}}$ denotes the respective counts recorded in pixel px of spectrometer S. This cross-correlation is calculated on a single-shot basis. After averaging over a large number of shots ($\gtrsim 10000$) the correlation map in Figure 5.5 is found. A distinct area

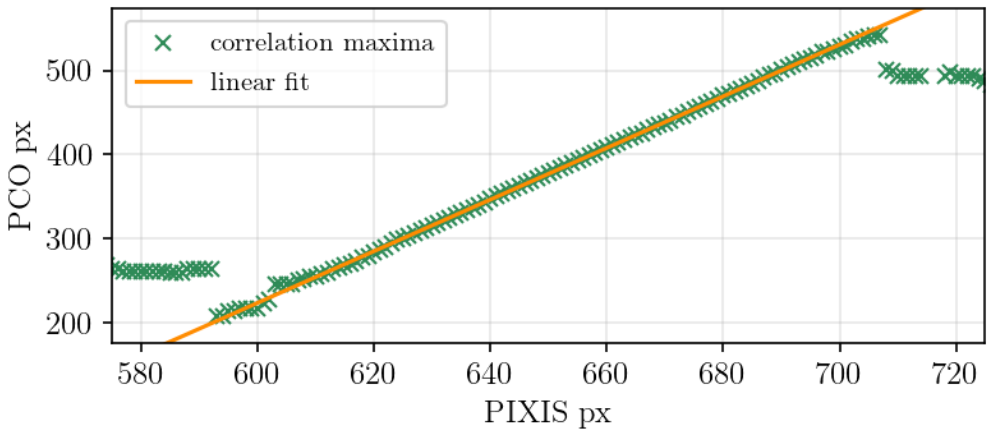

Figure 5.6.: Maxima of the correlation map (Figure 5.5). The linear mapping between experimental spectrometer and online reference spectrometer can be seen. This enables the energy calibration of the online reference spectra.

of high correlation ($\rho \sim 1$) in the shape of a narrow diagonal is found in the center of the graph surrounded by areas of vanishing correlation. The maxima of the correlation map can be precisely traced using a simple peak finder algorithm, which reveals the linear mapping between experimental spectrometer and online reference spectrometer (see Figure 5.6). This is used to calibrate the energy of the online reference spectra. As was stated before, this entire process is performed with no target gas inside the experimental apparatus. Since the settings of the spectrometer are not changed before performing the actual experimental measurements, the energy calibration remains the same. Since the pixel densities of the two spectrometers are different, in a final step, the now energy-calibrated online reference spectra have to be interpolated onto the energy axis of the experimental spectrometer to be able to determine the absorbance of a target. The count rate of the online reference spectrometer is adjusted to match the count rate the home-built spectrometer via the relation of integrated counts between the two spectrometers.

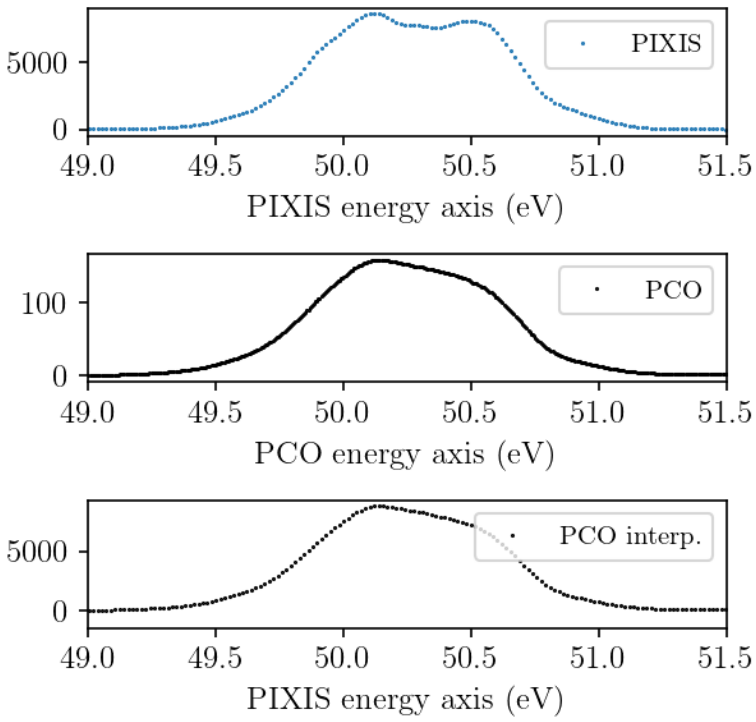

Figure 5.7.: Reference spectrum recorded with the home-built spectrometer (upper panel). Energy-calibrated online reference (mid panel). Online reference interpolated onto the energy-axis of the home-built spectrometer (lower panel).

6. XUV-pump–XUV-probe transient absorption spectroscopy on the nontrivial dissociation of diiodomethane (CH_2I_2)

In chapter 4, the experimental setup was introduced with which all of the experiments presented in this work were performed, while chapter 5 outlined the necessary steps of data processing that have to be taken before the experimental data can be interpreted. In this chapter, the results of the XUV-pump–XUV-probe transient absorption spectroscopy experiments in small halomethane molecules are presented. The experiments were conducted at the free-electron laser FLASH in Hamburg during a measurement campaign in 2016. In the course of this campaign, several further experiments were conducted. A dynamical study of the XUV-induced photo-dissociation of molecular oxygen will be presented in the following chapter. Further noteworthy experiments of the same measurement campaign, which are not the topic of this work, are the measurement of the XUV-intensity dependent lineshape change of the He 2s2p absorption line [81, 82] and the investigation of the influence of partially coherent SASE radiation on the coupling effects in doubly-charged neon ions [62, 83].

The focus of this chapter is on the study of ultrafast molecular dynamics that is triggered via a resonant XUV excitation. The particularity of this excitation step is its site-specificity. Tuning the employed XUV radiation to a core-to-valence resonance of the investigated molecule allows to excite an inner-shell electron of one of the bound (iodine) atoms to a molecular orbital. Transient absorption spectroscopy then allows to detect changes in the molecular absorption in real time. The main target of investigation for these experiments is the diiodomethane (CH_2I_2) molecule.

In recent years, the advances in ultrashort laser pulse technology enabled many experiments on femtosecond molecular dynamics. For instance, the femtosecond

photo-dissociation dynamics of molecules, following the breaking of a molecular bond by strong-field infrared [84] and ultraviolet [85, 86] laser pulses could be investigated in this way. The addition of an XUV probe from a high-harmonic source further augmented these studies by providing site-specific probing to the delocalized excitation [87–92]. In the presented work, this spectroscopic scheme will be further expanded by using a site-specific XUV excitation for the pump and probe steps. In this way, non-perturbative effects (e.g. Stark shift) are strongly suppressed. This gives a more straightforward access to the field-free molecular structure and dynamics.

The presented transient absorption spectroscopy, which is based on the detection of the XUV spectra transmitted through a target, can be seen as a complementary approach to techniques based on the detection of charged fragments. Charged-particle spectroscopy has been used with great success for the investigation of molecular dynamics, which includes time-of-flight experiments [93–95], velocity-map imaging studies [96, 97], as well as coincidence-detection experiments [19, 98–100].

6.1. The CH_2I_2 molecule

Diiodomethane (CH_2I_2, DIM) and its singly charged cation are a main target of investigation of this work. Therefore, the chemical relevance of diiodomethane and its electronic and molecular properties will be illustrated briefly in this section.

Many halocarbons play an important role in the atmospheric chemistry of the earth [101] and in the formation of marine aerosols [102]. Diiodomethane and other halomethanes are metabolic byproducts of marine algae and, increasingly, originate from anthropogenic sources. They are broken up by UV-photodissociation in the stratosphere, thereby forming a significant source for atmospheric iodine [103–105]. Iodine itself plays an important role as a condensation nucleus for marine aerosols[1] and as a reactant in ozone chemistry. Therefore, it has a large influence on the atmospheric greenhouse effect. Furthermore, diiodomethane and other halomethanes are widely used in the chemical industries, for instance as reactants in cyclopropanation reactions [107].

This work focuses on the ultrafast relaxation dynamics of diiodomethane upon resonant core-electron excitation with extreme ultraviolet (XUV) light. Diiodomethane was chosen as a target for this experiment for several reasons. Atomic iodine with its

[1] As marine aerosols one classifies aerosols in the atmospheric layer above the oceanic surface. They are mostly of marine origin and not transported there from land masses [106].

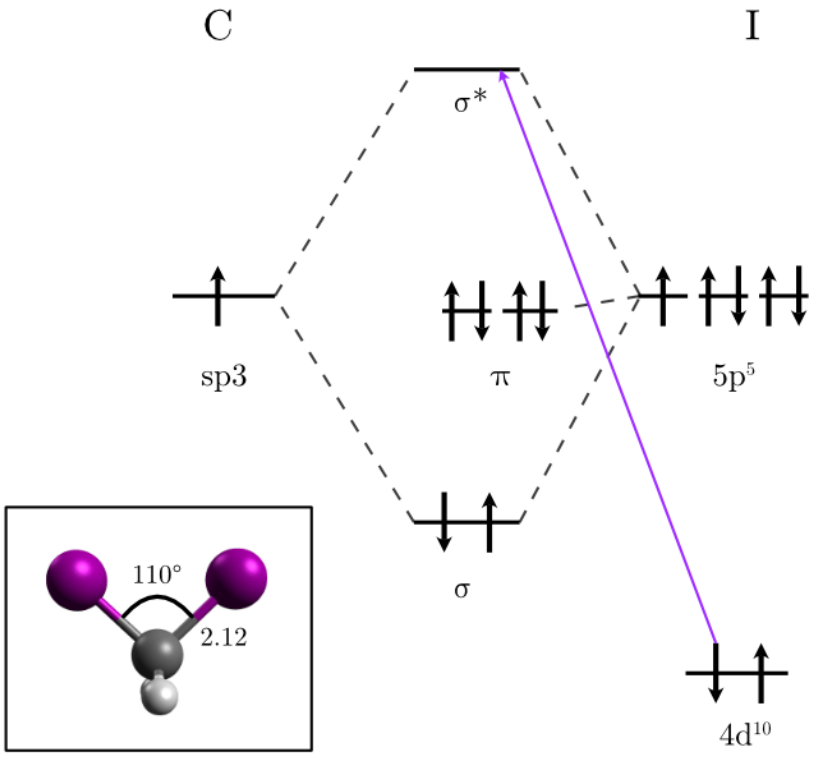

Figure 6.1.: The electronic structure of the molecular C-I bond of the diiodomethane molecule is shown here. An electron from the iodine p-orbital and one from the carbon sp3-hybridized orbital hereby form a σ-type molecular bond. The site-specific transition from an iodine 4d-orbital to an antibonding σ^* molecular orbital via a $\sim 50\,\mathrm{eV}$ photon is indicated by the purple arrow. The inset in the box shows the configuration of the neutral diiodomethane molecule with the bond length in Å.

53 electrons has multiple closed electronic shells ($[\mathrm{Kr}]\,4d^{10}\,5s^2\,5p^5$). Transitions from those inner shells to energetically higher levels have a very defined transition energy. The observed resonances in electron or photon absorption spectra that emerge from different core-to-valence transitions don't overlap and are also highly element-specific [37]. They retain their element-specificity even when the iodine atom is bound in a molecule [108, 109]. This enables a very defined, site-specific excitation step of the molecular target. Additionally, the photoabsorption cross section of iodine-containing molecules in the XUV spectral domain is on the order of a few Mb [110]. This comparatively large absorption cross section greatly facilitates the technically very challenging XUV transient absorption experiments described in this work. Lastly, diiodomethane has a very interesting size for quantum dynamical studies. On the one hand, it is small enough to be able to calculate its electronic structure with sufficient precision and to visualize intra-molecular nuclear motions in a clear manner. On

the other hand it is already large enough to be a three-dimensional molecule whose geometry can change upon excitation [111, 112].

Diiodomethane is a liquid at standard conditions with a vapor pressure of 1.1 mbar at 20 °C [113]. Therefore gentle heating of the liquid sample is necessary to get a sufficiently high target density for transient absorption spectroscopy. At 80 °C a vapor pressure of $\sim$ 15 mbar can be reached, which is sufficient for the sensitivity of the presented experimental setup.

The electronic structure of the diiodomethane molecule with its C-I bonds can be seen in Figure 6.1. This σ-type molecular bonds are formed by a 5p-orbital of the iodine atom and an sp3-hybridized orbital of the carbon. The XUV transition from the iodine 4d orbital to the antibonding σ^* molecular orbital is indicated by a purple arrow. The remaining p-electrons of the iodine don't participate in this molecular bond.

A static XUV absorption spectrum of diiodomethane was recorded prior to the FEL measurement campaign with the broadband XUV high-harmonic source in Heidelberg (see Figure 6.2). It shows several pronounced absorption resonances of which only the investigated $4d_{5/2}$–σ^* resonance lies within the FEL spectrum.

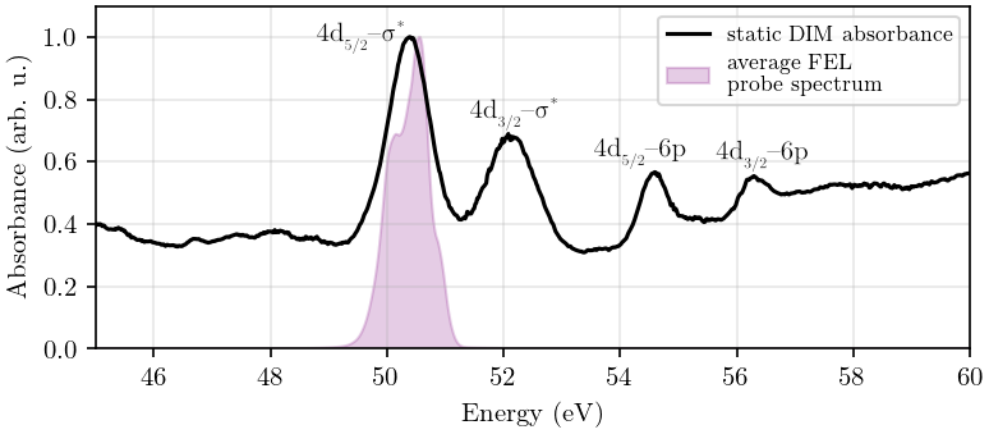

Figure 6.2.: Static absorption spectrum of diiodomethane in the XUV spectral range between 45 eV and 60 eV, as recorded with our broadband high-harmonic source in Heidelberg. The spin-orbit split 4d–σ^* and 4d–4p absorption resonances can be seen on top of a nonresonant absorption background. The average FEL probe spectrum as used in the presented experiment is shown as well as a purple shaded area. Only the $4d_{5/2}$–σ^* resonance lies within this probe spectrum.

6.2. The experimental scheme

The entire experimental setup is illustrated in chapter 4, while the working principle of the FEL light source is outlined in chapter 3. A brief sketch of the experimental scheme for the transient absorption on small molecules is given here (see Figure 6.3).

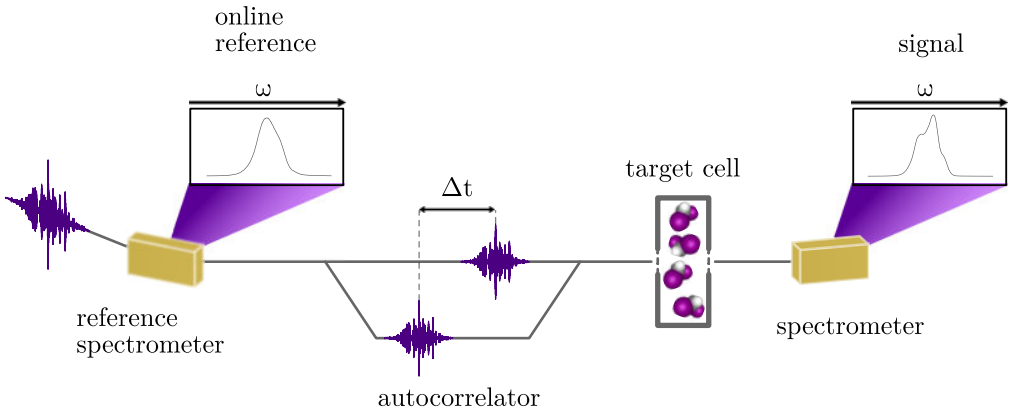

Figure 6.3.: A sketch of the experimental scheme. The SASE FEL pulses enter the setup from the left with a repetition rate of 10 Hz. For every FEL shot, a reference spectrum is recorded (see section 5.4) before it enters the split-and-delay unit (autocorrelator, see section 4.2). There, the FEL pulses are split into pump and probe pulses and a variable time delay between those two is introduced (see section 4.2). Pump and probe pulses are focused into the heated target cell containing the diiodomethane sample (see section 4.3). The transmitted probe spectrum is subsequently detected in a high-resolution spectrometer as a function of the pump-probe time delay (see section 4.4).

The incoming SASE FEL pulses have a repetition rate of 10 Hz, a pulse energy of $48 \pm 13\,\mu J$ and a pulse duration of about 65 fs, as inferred from XUV-XUV autocorrelation measurements, see section 5.1. A reference spectrum of every incoming FEL pulse, before it enters the target, is recorded on a single-shot basis via the FLASH BL2 online spectrometer [60] (see sections 3.5.2, 5.4). The FEL pulses are then geometrically split into a pulse pair via the FLASH BL2 autocorrelator (see section 4.2). For an ideal FEL beam, the hereby generated pump and probe pulses would be exact copies of each other up to their intensity which can be adjusted via the splitting ratio. However, due to its spontaneous generation process, the FEL beam experiences a spatial chirp. Therefore, pump and probe pulses have slightly different spectra even in the absence of an absorbing target (see Figure 6.4). Since the online reference spectra are taken from the full beam, this has to be taken into account when calculating the optical density (OD) of the target medium. For the presented experiment, the pump pulses were chosen to be roughly 50 % more intense

than the probe pulses. The time delay between the pump and probe pulses is varied by changing the length of one of the interferometer arms. Both pulses are then focused into the target cell (see section 4.3) in a noncollinear geometry to a focus size of 25 µm. They spatially overlap in the focus and are separated again in the far field. Therefore, the spectra of pump and probe pulse can be detected simultaneously on the same camera chip. In principle, the roles of pump and probe pulse are interchangeable in this way. The nomenclature of "pump pulse" for the more intense pulse and "probe pulse" for the weaker pulse is used throughout this work. The average pulse energy of 48 µJ, the focus size of 25 µm and the average pulse duration of 65 fs, together with a transmission of the experimental setup of roughly 25 % translate into on-target intensities in the mid-10^{13} W cm^{-2} regime. The diiodomethane target was brought into the interaction region via gentle heating of the sample reservoir and the connected feeding tubes to $\sim 80\,°C$, as delineated in chapter 4.3.

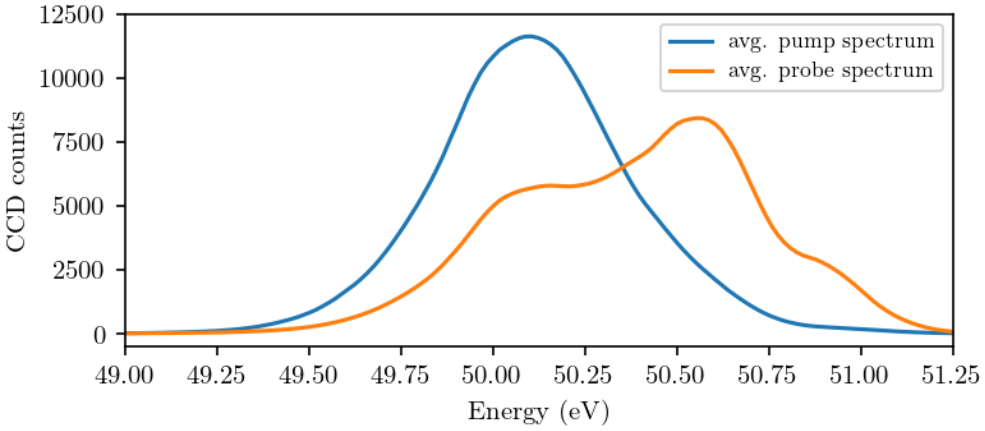

Figure 6.4.: Average spectra of the pump and probe pulses in the absence of an absorbing target. The different spectral shape of pump and probe spectra is the result of the FEL beam's spatial chirp and not a signature of absorption. As can be seen, the center of the probe spectrum is shifted to higher energies by ~ 0.2 eV due to a spatial chirp in the FEL beam. This leads to an artifact in the optical density (OD), since the reference spectrum is taken from the full FEL beam. This systematic deviation is intrinsically removed in the calculation of the differential OD due to it being time-independent. See main text for more details.

6.3. Time-dependent transient absorption spectroscopy of diiodomethane

The pump and probe spectra, as well as the online reference spectra are recorded on a single-shot basis while scanning the pump-probe time delay. For the evaluation of the experimental data, only FEL pulses that fall into the pulse energy range between 40 µJ and 60 µJ are selected (see Figure 6.5). This is done to mitigate the influence of outliers, since FEL pulses with extreme pulse energy values also tend to be spectral outliers compared to the average FEL spectrum [71].

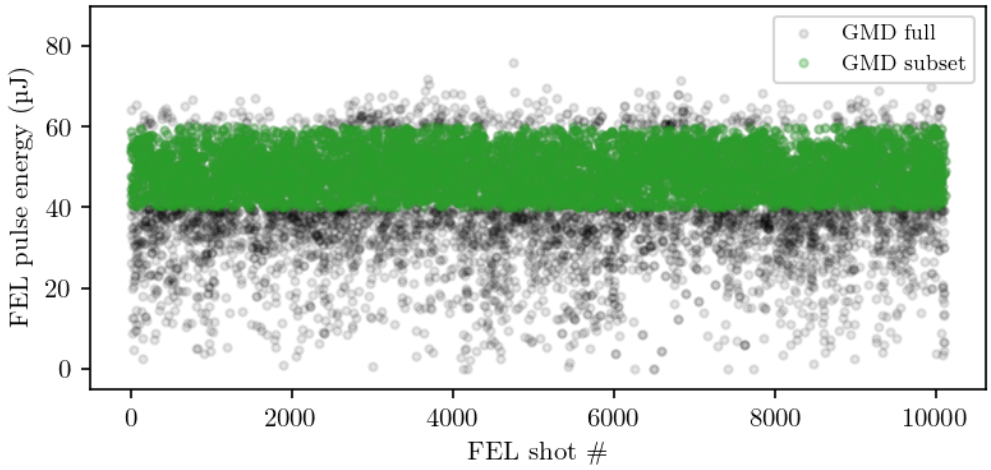

Figure 6.5.: FEL pulse energy measured on a single-shot basis in the gas monitor detector (GMD, see section 3.5.1). Only FEL shots, whose pulse energy falls in the range between 40 µJ and 60 µJ are considered for the data analysis to mitigate the influence of outlier pulses.

After the energy calibration of the spectra, as delineated in chapter 5, the transmitted spectra along with their corresponding online-reference spectra are shown in Figure 6.6. The time-dependent absorbance, or optical density (OD) is calculated from these spectra according to:

$$\mathrm{OD}(E,t) = -\log_{10}\left[\frac{I_{\mathrm{probe}}(E,t)}{I_{\mathrm{online\ ref.}}(E,t)}\right], \tag{6.1}$$

where $I_{\mathrm{probe}}(E,t)$ are the transmitted probe spectra and $I_{\mathrm{online\ ref.}}(E,t)$ are the corresponding online reference spectra. Albeit all spectra being measured on a single-shot basis, it is not possible to calculate optical density on a shot-to-shot basis due to the different resolving powers of the two spectrometers. The spiky structure of the SASE

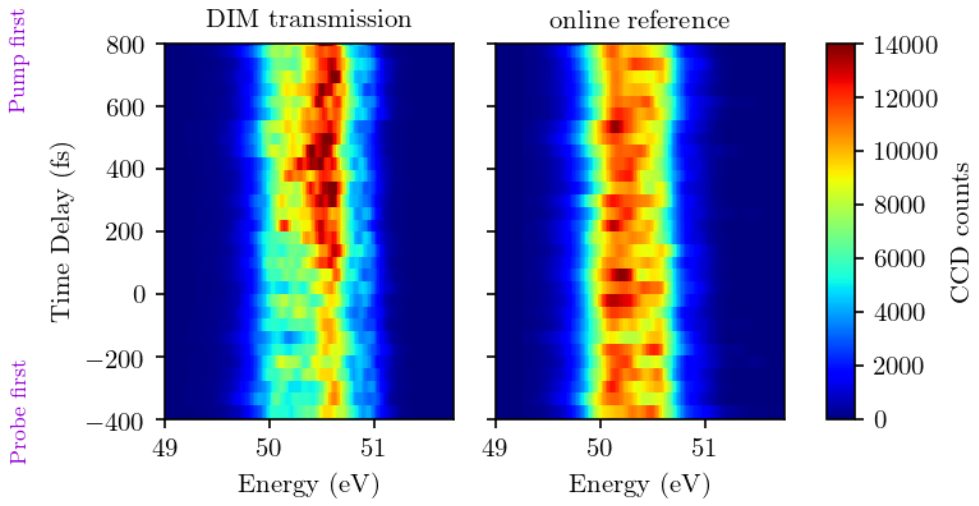

Figure 6.6.: Left panel: Probe spectrum, transmitted through the diiodomethane sample. Right panel: online reference spectrum taken from the full FEL beam. The increased transmission of the probe beam for positive time delays (pump first) can be clearly seen already in this raw data.

spectra (cf. Figure 3.4) leads to artifacts through the division in Eq. (6.1). Therefore, the average over 100 single-shot spectra is taken for every time-delay position before calculating the optical density (see Figure 6.7). A pronounced gradient from positive optical density at lower photon energies to negative optical density at higher photon energies can be observed. This is a remnant of pump and probe spectra not being identical (cf. Figure 6.4), which has to be corrected for. It stems from the fact that the average probe spectrum's center of mass is at higher photon energies than that of the entire FEL beam's average spectrum. Since the optical density [EQ. (6.1)] is calculated with the online reference spectra which are taken from the entire FEL beam (cf. Figure 6.3), this unphysical artifact occurs. To remove this artifact, the differential OD (ΔOD) can be used. It is calculated by averaging the OD between −400 fs and −100 fs and subtracting this average from the time-dependent OD:

$$\Delta\mathrm{OD}(E,t) = \mathrm{OD}(E,t) - \langle \mathrm{OD}(E,t) \rangle|_{t=-400\,\mathrm{fs}}^{t=-100\,\mathrm{fs}} \tag{6.2}$$

The OD for negative time delays, where the probe pulse interacts with the unperturbed target, is equal to the static absorbance of the target. By subtracting it from the time-dependent OD, the changes in absorbance are highlighted. Another advantage of using the ΔOD is that the time-independent systematic deviations are inherently removed (see Figure 6.8). Two main features emerge in the plot of the $\Delta\mathrm{OD}(E,t)$.

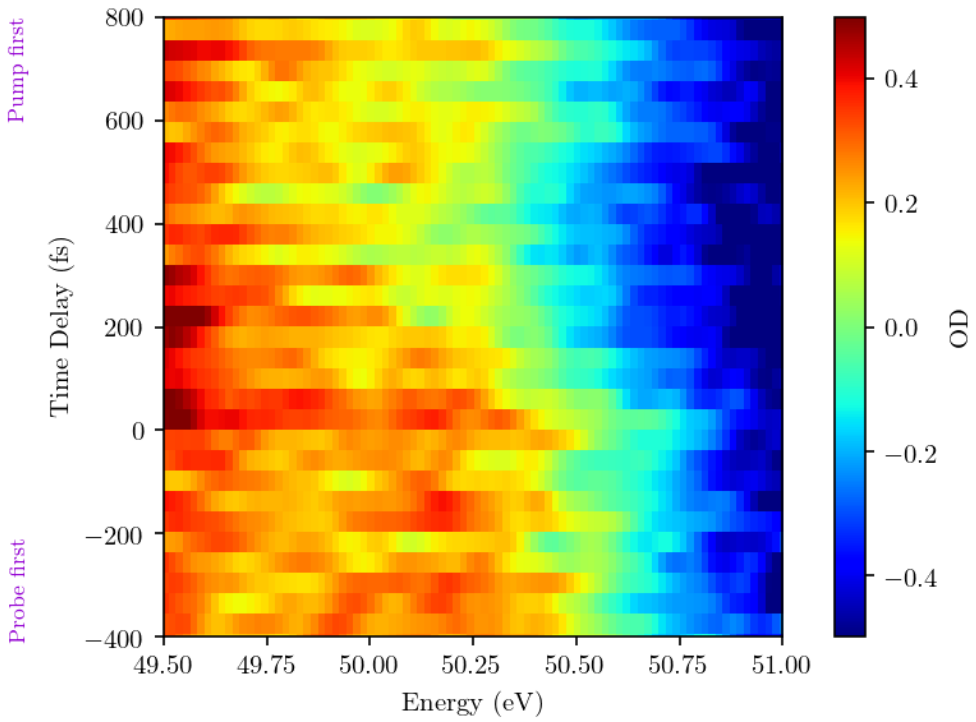

Figure 6.7.: Optical density (OD) calculated according to Eq. (6.1). The gradient from positive OD at low energies to negative OD at high energies that can be observed independent of the time delay is an artifact of the unequal pump and probe spectra. Nevertheless, a gradual decrease in total absorption can be observed around the peak of the $4d_{5/2}$–σ^* resonance (50.0 eV-50.8 eV). Additionally, an increase in absorption is visible around a time delay of 200 fs and the energy of 49.6 eV.

In the vicinity of the $4d_{5/2}$–σ^* resonance, a smooth decrease in absorbance is visible. while in the lower energy region around 49.6 eV a transient increase in absorbance can be observed. The underlying molecular processes that lead to these dynamical absorption features will be discussed in the following paragraphs.

6.3.1. The time constants of the observed dynamics

As can be seen in Figure 6.8, the SASE fluctuations of the FEL pulses lead to statistical noise in the experimental data. Since the chosen time delay step size of 40 fs is much shorter than any expected molecular dynamics and even shorter than the instrument response function of 65 fs (see chapter 5.1), a boxcar moving average over ±1 delay step in time delay direction of the $\Delta\mathrm{OD}(E,t)$ is performed in order to increase the number of averaged spectra. This is done by convolution of $\Delta\mathrm{OD}(E,t)$ with the

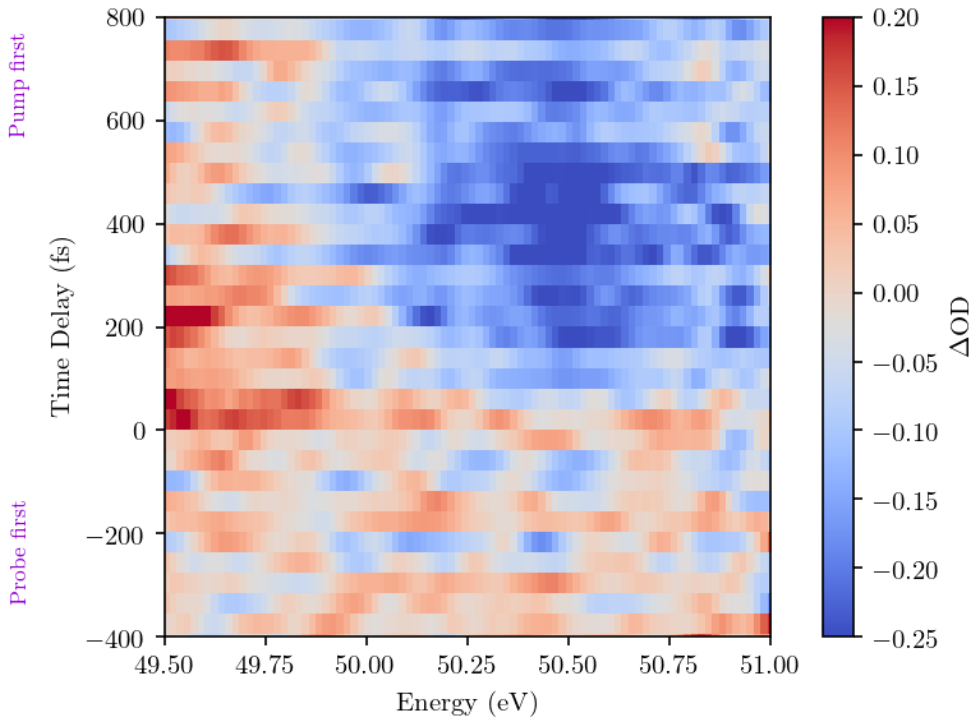

Figure 6.8.: The differential ΔOD, calculated according to Eq. (6.2). The decrease in absorption in the vicinity of the $4d_{5/2}$–σ^* resonance (50.0 eV-50.8 eV) is clearly visible, as is the transient increase in absorption between 0 fs and 400 fs around 49.6 eV.

rectangular function $\Pi(t, T)$:

$$\Delta\widetilde{\mathrm{OD}}(E, t) = \Pi(t, T) * \Delta\mathrm{OD}(E, t), \tag{6.3}$$

with

$$\Pi(t, T) = \Theta(t + T/2) - \Theta(t - T/2), \tag{6.4}$$

where $\Theta(\tilde{t})$ is the heaviside step function and T defines the width of the boxcar function. The resulting $\Delta\widetilde{\mathrm{OD}}(E, t)$ in relation to the static absorption spectrum can be seen in Figure 6.9. Since the spectral bandwidth of the FEL probe beam is on the order of 1 eV, only the $4d_{5/2}$–σ^* resonance of the spin-orbit split 4d–σ^* transition can be investigated, as can be seen in Figure 6.9. Nevertheless, the transient absorption change within this narrow probe window can be linked to non-trivial molecular relaxation dynamics with support from theory as is shown in this section.

In a first step the time constants associated with the observed dynamics will be

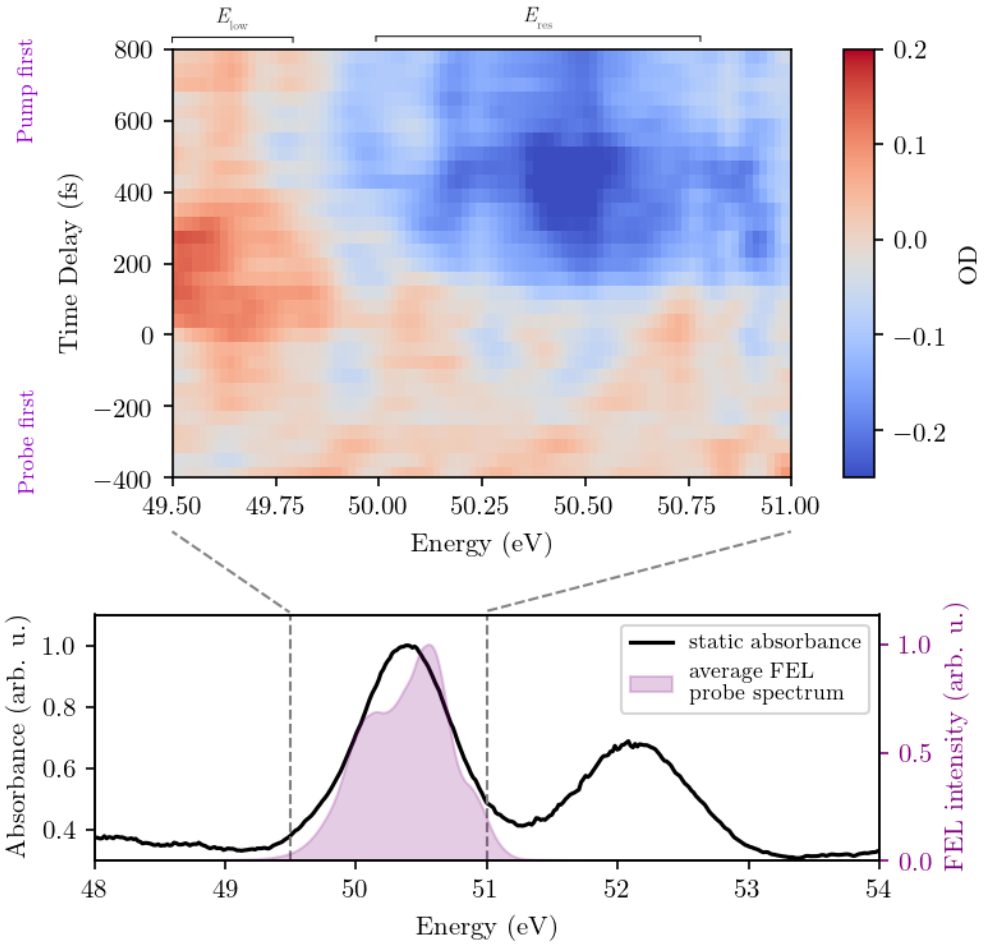

Figure 6.9.: The differential absorbance ΔOD in the vicinity of the $4d_{5/2}$–σ^* resonance of diiodomethane as a function of the pump-probe time delay (upper panel). In the lower panel, the static absorbance of diiodomethane is shown over a wider energy range (cf. Figure 6.2). The average FEL probe spectrum is illustrated in violet shading. The energy regions E_{low} and E_{res} are indicated on top of the graph.

investigated. For this purpose, the following global exponential fit model is employed:

$$\begin{aligned}\Delta\mathrm{OD}(E,t) = y(E) + \mathrm{IRF}(t) * [\Theta(t) \times (\Delta\mathrm{OD}_{\mathrm{late}}(E) \\ + \Delta A_1(E) e^{-t/\tau_1} + \Delta A_2(E) e^{-t/\tau_2})].\end{aligned} \tag{6.5}$$

Hereby, E is the photon energy and t is the time delay. $y(E)$ is a time-independent offset, $\mathrm{IRF}(t)$ is the instrument response function that is modeled by a Gaussian function of width 65 fs FWHM (see section 5.1). $\Theta(t)$ is the Heaviside step function, while $\Delta\mathrm{OD}_{\mathrm{late}}(E)$ is the value of the ΔOD measured at large positive time delays ($t = 800$ fs). The time constants τ_1 and τ_2 are independent of energy and quantify

the molecular dynamics that underlie the observed absorption change. $\Delta A_1(E)$ and $\Delta A_2(E)$ are their corresponding spectral weights. The $*$-symbol denotes the convolution between the function describing the dynamics and the IRF, while the $\times$-symbol denotes a multiplication. In principle, the entire spectro-temporal absorption $\Delta\mathrm{OD}(E,t)$ can be globally modeled with Eq. (6.5). However, since the probe window only has a spectral width of 1.5 eV and the noise level of the data is comparatively high due to the SASE fluctuations of the FEL, the global fit is restricted to two spectral components of the data. One at the resonance energy region (E_{res}), averaged between 50.0 eV and 50.8 eV and the other in the low-energy region (E_{low}), averaged between 49.5 eV and 49.8 eV. Globally fitting Eq. (6.5) to the data results in the two time constants $\tau_1 = 166 \pm 11$ fs and $\tau_2 = 290 \pm 30$ fs. The results of the fit are summarized in Table 6.1 and are plotted in Figure 6.10 together with the ΔOD averaged over the spectral regions of interest E_{low} and E_{res}. The error bars on the lineouts are calculated via error propagation of the standard error of the mean of the ΔOD. It is apparent

Table 6.1.: Results of globally fitting Eq. (6.5) to the measured ΔOD.

energy region (eV)	$\tau_1 = 166 \pm 11$ fs	$\tau_2 = 290 \pm 30$ fs
E_{low}: 49.5 − 49.8	$\Delta A_1 = 0.04 \pm 0.06$	$\Delta A_2 = 0.11 \pm 0.05$
E_{res}: 50.0 − 50.8	$\Delta A_1 = 0.57 \pm 0.06$	$\Delta A_2 = -0.34 \pm 0.05$

from the results of the global fit model, that the transient increase in the low-energy region E_{low} appears with the time constant of the IRF and decays again with the longer time constant $\tau_2 = 290 \pm 30$ fs. The on-resonance absorption at E_{res} on the other hand decays with the faster time constant $\tau_1 = 166 \pm 11$ fs. The time constants on the order of a few 100 fs indicate that the underlying mechanism includes nuclear motion and not only an electronic response of the system.

In a first interpretation of the observed features, the resonant decrease in absorption (E_{res}) is linked to the direct dissociation of the molecule. When a fraction of the ensemble of diiodomethane molecules in the target volume breaks apart, the total absorption is lowered. This is of course not only true at the resonance energy, but everywhere. Unfortunately most of the nonresonant absorption happens outside of our probe spectrum. The transient feature at lower energies (E_{low}), which appears and vanishes again, indicates that direct dissociation can not be the only contribution to the observed dynamics. Prior research on diiodomethane suggests that isomeric

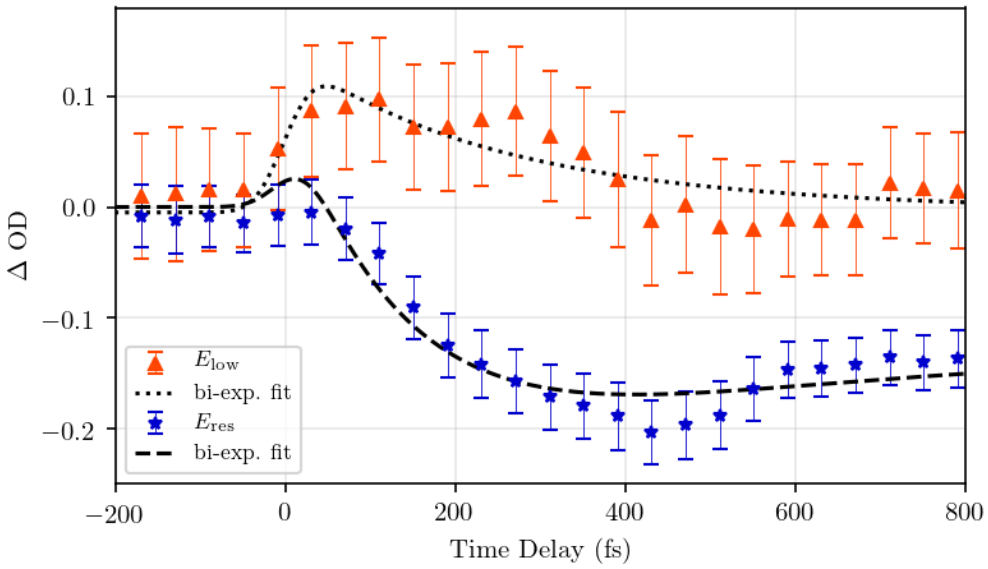

Figure 6.10.: Lineouts through the $\Delta\text{OD}(E,t)$, averaged over the energy regions $E_{\text{low}} = 49.5 - 49.8\,\text{eV}$ and $E_{\text{res}} = 50.0 - 50.8\,\text{eV}$, together with the results of globally fitting Eq. (6.5) to these lineouts.

species of the diiodomethane cation $CH_2I_2^+$ may play a role in the dissociation of diiodomethane. Experiments using UV-photoexcitation in the valence shell [111], as well as static synchrotron experiments [112] have been conducted on this topic. In this work, a time-dependent study of the diiodomethane dissociation dynamics after a core-electron excitation is presented.

6.3.2. The mechanism

The first pulse resonantly excites a localized iodine 4d electron into an antibonding σ^* molecular orbital in the valence shell (cf. Figure 6.1). The hereby generated core hole decays on a time scale of 10 fs via an Auger process [39, 40]. This is much faster than the instrument response function of the experimental setup and can therefore not be resolved. The cationic states populated via this Auger decay determine the further molecular relaxation dynamics. The resonant excitation step leads to the production of singly charged cations as the most abundant species in the target volume. This might at first seem surprising for an inner-shell excitation at 50 eV photon energy, followed by an Auger decay. However, one has to keep in mind that the discussed excitation step is a resonant process in the neutral molecule. No direct photoionization occurs before the Auger decay. In principle it is energetically possible to generate

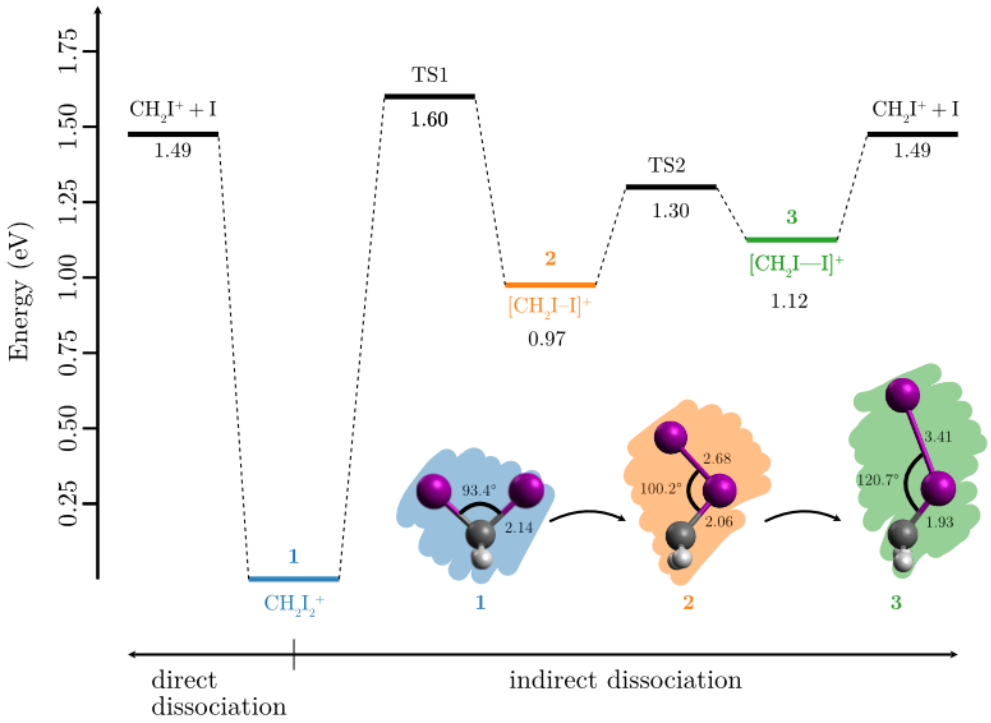

Figure 6.11.: Potential energies of the direct and indirect dissociation paths of the diiodomethane cation. The indirect dissociation path involves the three minimum-energy structures 1, 2 and 3, as well as the transient states TS1 and TS2 inbetween them. The corresponding geometries of the molecular cation in its three minimum-energy structures are shown in the inset. All distances are in Å. The figure is adapted from reference [112].

dications via the ejection of two Auger electrons. However, as is reported in reference [114] for the case of atomic iodine, the branching ratio for I^{2+} to I^+ is roughly 1:2 upon the similar atomic 4d–5p transition. The production of singly-charged cations is favored in this case since all Auger final states lie below the double ionization threshold of iodine. The same is true for diiodomethane, since the calculated Auger final states are located between 8.5 eV and 14 eV (cf. Figure 6.12) and, therefore, below the double ionization threshold of diiodomethane at 24 eV. Only few excited states are populated in this way, while the Auger electron carries away the excess energy.

The transient increase of absorption in the low-energy region E_{low} (cf. Figure 6.9, Figure 6.10) indicates that, in addition to the direct dissociation of the diiodomethane molecule, another relaxation mechanism has to be at play. Previous static synchrotron experiments on $CH_2I_2^+$ suggest that an indirect dissociation path exists that includes isomeric geometries of the cation [112]. A sketch of the energy landscape of direct

and indirect dissociation path can be found in Figure 6.11. Both of these dissociation pathways occur in parallel. The structure of the molecule is shown in the inset for three points along the indirect dissociation path, with all of the bond lengths given in Å. Geometry 1, hereby is the geometry of the cation in its ground state, while geometries 2 and 3 are two minimum-energy configurations along the indirect dissociation path.

The influence of the isomeric geometries on the observed absorption changes is investigated in this work. To do so, the absorption spectra of the molecular geometries 1-3 have to be known. The electronic excitation spectra of the isomeric species were computed by our theory collaboration partners Victor Despré and Alexander I. Kuleff from the Institute of Physical Chemistry of the University of Heidelberg. The ionization spectra are computed using the Algebraic Diagrammatic Construction Green's function method at third order (ADC(3)) [115]. This method returns the energies needed to produce each cationic state through the removal of an electron from a specific orbital of the neutral molecule. The energy of the first state is thereby equal to the first ionization potential of the system. The height of the poles is proportional to how much a state is populated after the ionization [116]. The exemplary ionization spectrum of molecular geometry 1 can be found in Figure 6.12.

After the cations have been produced by the pump pulse, the probe pulse interrogates the temporal evolution of the cations via the excitation of a dipole transition between cationic states. The first ten states of the ionization spectrum are considered to be initial states for these probe transitions and are plotted in red[2], while all energetically higher states are considered final states of the transitions and are plotted in blue. Initial and final states are assessed by an energetic consideration. Since the photon energy of the probe pulse roughly spans a bandwidth between 49.5 eV and 51 eV, the transition energies between initial and final states also have to be in this range to be observable within the available probe window. As can be seen from Figure 6.12, the tenth state is already ~ 5.5 eV above the first state. Therefore, its contribution to the absorption in the probed spectral window is small[3]. Transitions from even higher lying initial states lead to absorption features at photon energies below our probe window.

In addition to the ionization spectra, the transition dipole moments $\mathrm{d}_{i,f}$ between the ten initial states (i, plotted in red) and the final states (f, plotted in blue) are

[2]Only 7 states of are visible in the plot, since the pole strength of 3 intermediate states is vanishing.
[3]From reference [109] it is known that the same is true in the case of iodomethane (CH_3I).

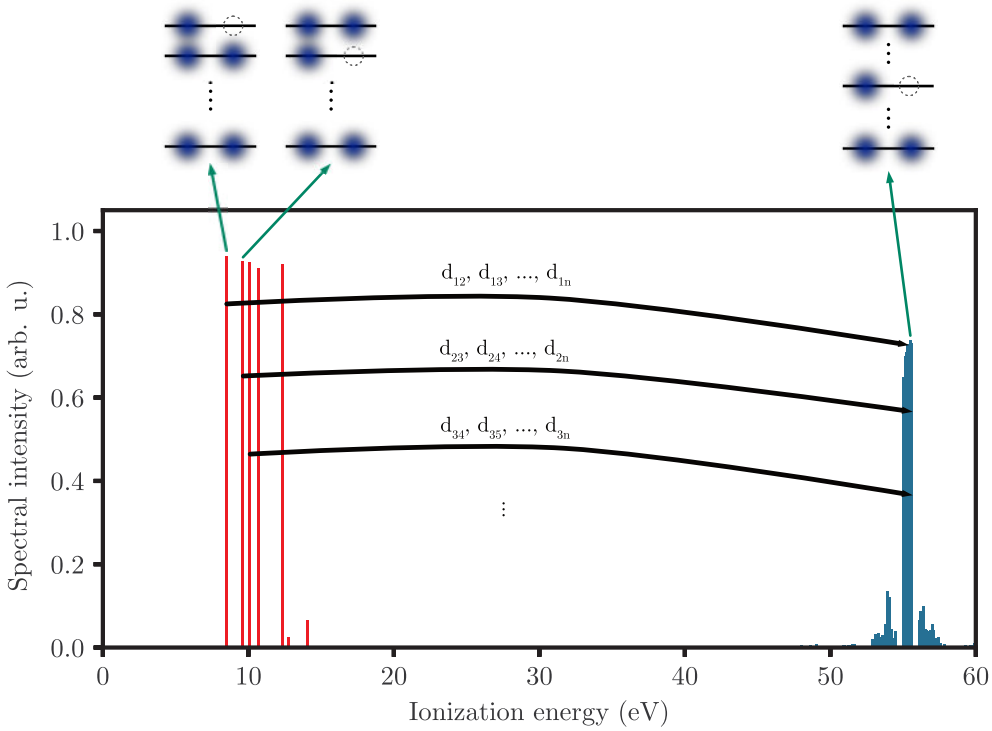

Figure 6.12.: Ionization spectrum of the diiodomethane cation in geometry 1, computed via the Algebraic Diagrammatic Construction at third order (ADC(3)) [115]. Individual poles are obtained by removing an electron from a specific molecular orbital, as indicated by the piktogramm on top. Additionally, the transition dipole moments $d_{i,f}$ between the ten energetically lowest states (initial i, marked in red) and every higher lying state (final f, marked in blue) that can be reached by the absorption of one 50 eV photon are calculated. The possible transitions are indicated by the black arrows.

calculated. Only final states that can be reached with a single 50 eV photon are considered. Transitions between all other states don't contribute to the absorbance within our probed spectral range. From the ionization spectra, the transition energies between every initial ($i = 1, \ldots, 10$) and all final states ($f = 1, \ldots, n$) are calculated. The contribution of every such transition to the total absorption is proportional to the absolute square of its corresponding transition dipole moment $\left|d_{i,f}\right|^2$. Finally, every absorption contribution is convolved with a Gaussian with a width that corresponds to the Auger lifetime of 10 fs. The entire procedure is repeated for all of the molecular geometries 1-3 as depicted in Figure 6.11. The resulting theoretical absorption spectra of the diiodomethane cation $CH_2I_2^+$ in the configurations of geometry 1-3 can be found in Figure 6.13. It has to be noted that the theoretically calculated absorbance in Figure 6.13 is plotted on a logarithmic scale. As can be seen from Figure 6.13, the absorption spectrum of geometry 1 reveals an absorption peak at ~ 50.8 eV, which

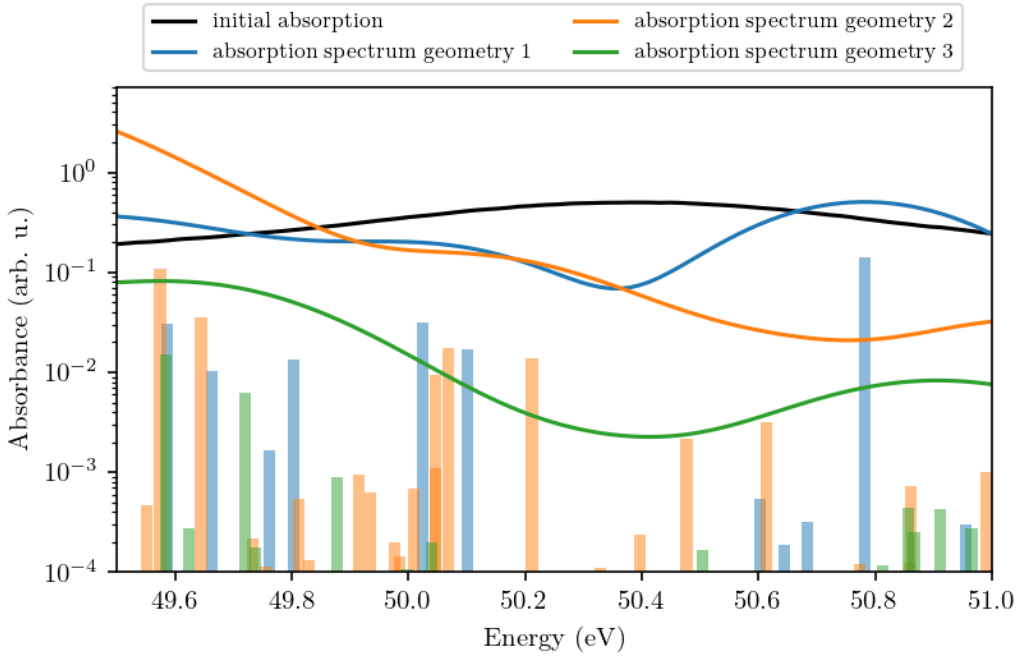

Figure 6.13.: Measured absorption spectrum of the initial molecular configuration 0, as well as the absorption spectra of geometries 1-3, computed from the transition energies and the absolute square of the transition dipole moments $\left|\mathrm{d}_{i,f}\right|^2$ provided by the ADC(3) method. The individual $\left|\mathrm{d}_{i,f}\right|^2$ are shown as vertical bars. The absorption spectra of geometries 1-3 are the result of convolution with a Gaussian, the width of which corresponds to the Auger lifetime. The color coding shows the affiliation to the geometries 1-3.

is in the vicinity of the diiodomethane $4\mathrm{d}_{5/2}$–σ^* resonance (cf. Figure 6.2). This absorption peak vanishes for geometries 2 and 3. The absorption of geometry 2 instead peaks in the energy region E_{low} where the transient increase in absorption can be observed in the experimental ΔOD (cf. Figure 6.9). The absorption of geometry 3 is roughly an order of magnitude smaller than that of geometries 1 and 2 in the probed spectral window. Additionally, the measured absorption of the neutral molecule is shown.

The conformity of geometry 2's absorption peak with the transient increase in the experimental data is a first indication that the indirect dissociation path of the diiodomethane cation is responsible for this observed feature in the transient absorption data. On its way into fragmentation, the cation would transiently pass the individual isomeric geometries in a time-ordered sequence. To investigate if this is reflected in the observed experimential ΔOD, the following fit model is employed:

$$\begin{aligned}\Delta\mathrm{OD}(E,t) = \Delta a_0(t)S_0(E) + \Delta a_1(t)S_1(E) \\ + \Delta a_2(t)S_2(E) + \Delta a_3(t)S_3(E) + b(t).\end{aligned} \tag{6.6}$$

The $S_i(E)$ $(i = 1, 2, 3)$ designate the absorption spectra of the cationic geometries, while $S_0(E)$ denotes the absorption spectrum of the neutral molecule. The time-dependent amplitudes $\Delta a_j(t)$ $(j = 0, 1, 2, 3)$ are a measure of every molecular configuration's contribution to the total differential absorption at a specific time delay. Therefore, they can be used to track the evolution of the molecule's geometry change. In general the individual molecular configurations have a non-resonant background absorption in addition to their resonant absorption features. The presented theoretical absorption spectra only account for the resonant part of the absorption. Therefore, a non-resonant background $b(t)$ is introduced in the fit model.

The model for $\Delta\mathrm{OD}(E, t)$ in Eq. 6.6 is fitted to the experimental data for every time-delay position by varying the amplitudes $\Delta a_j(t)$, with $j = 0, 1, 2, 3$, and minimizing the squared residuals. The resulting temporal evolution of the individual contributions to the total $\Delta\mathrm{OD}(E, t)$ can be found in Figure 6.14. The progression of the molecule through its different configurations can be clearly seen following a logical time-ordering of the absorption contributions $\Delta a_0(t), \Delta a_1(t)$, $\Delta a_2(t)$, $\Delta a_3(t)$. Intuitively, one would expect a sharp drop in $\Delta a_0(t)$ with a simultaneous increase in $\Delta a_1(t)$ with the time constant of the IRF at $t = 0$ due to the ionization of the target. The absence of this feature, in combination with the overall minor contribution of geometry 1 can be explained by the similarity of the cationic and neutral absorption spectra at $t = 0$. Directly after the ionization, the cation will still be in the same geometry as the neutral molecule in its ground state, since the nuclei didn't have the time to move far within the XUV excitation and successive Auger decay. At later times, when the the nuclei have moved, a gradual decrease in the contribution $\Delta a_0(t)$ can be observed (see Figure 6.14), which is linked to the bleaching of this initial state. The subsequent increase in $\Delta a_2(t)$ can be linked to the molecule progressing through the isomeric geometry 2. Its contribution peaks at $\sim 200\,\mathrm{fs}$, which is where the transient increase of absorption in the low-energy region E_{low} of the experimental absorption also has its maximum (cf. Figure 6.9, Figure 6.10). Additionally, an increase in $\Delta a_3(t)$ can be observed, which saturates roughly 400 fs after the temporal overlap of the pump and probe pulses. Based on the completion of the decrease of initial-state geometry and transient geometry 2 at very late times, one may conclude that the indirect dissociation process has only been completed after about 400 fs. The small background contribution $b(t)$ for positive time delays can be explained by nonresonant absorption of the isomeric geometries 1-3 or molecular fragments, which are not considered in the theoretical absorption spectra. The molecular fragments possess no

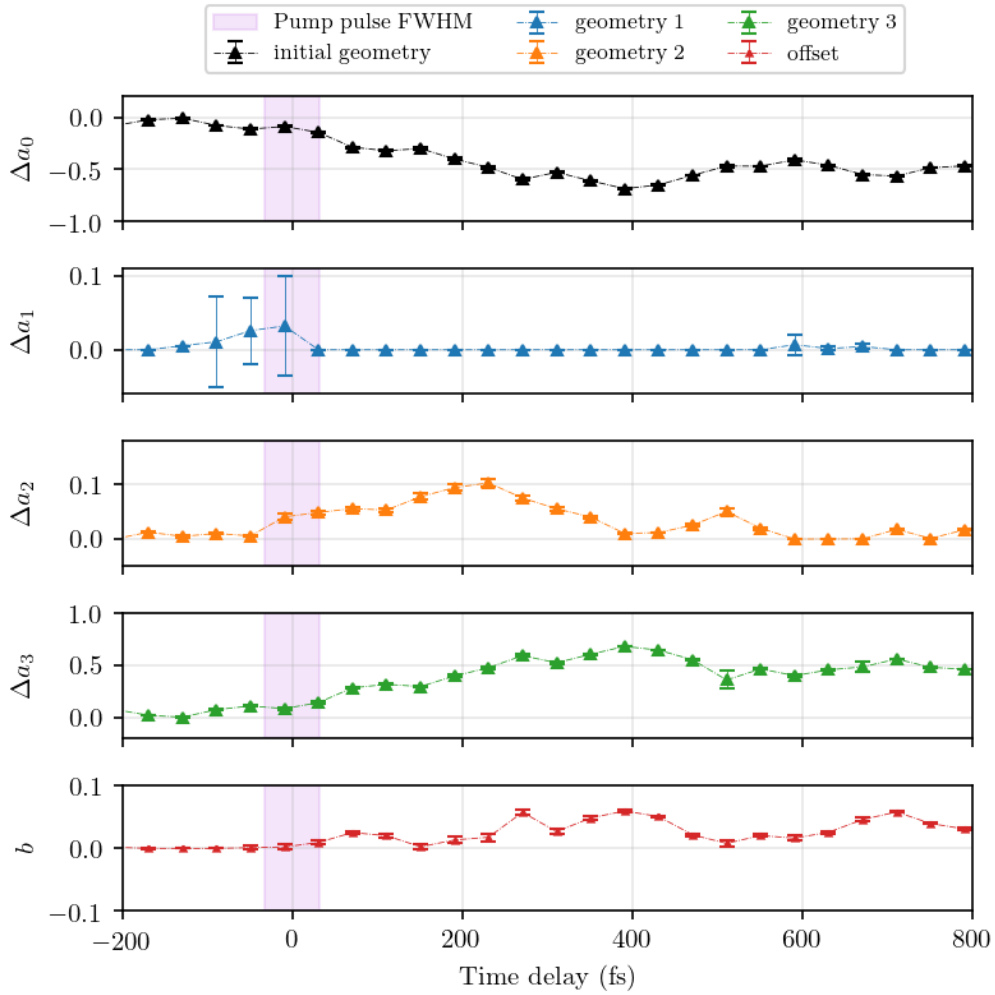

Figure 6.14.: The amplitudes Δa_j $(j = 0, 1, 2, 3)$ are the results from fitting Eq. (6.6) to the experimental data and represent the contributions of the individual configurations of the target to the total absorption. $\Delta a_0(t)$ represents the temporal evolution of the initial geometry, while $\Delta a_1(t)$, $\Delta a_2(t)$ and $\Delta a_3(t)$ are the absorption contributions from the cationic geometries 1-3 as drawn in Fig. 6.11. $b(t)$ is the contribution of the nonresonant background to the absorption. The duration (FWHM) of the pump pulse is illustrated by the purple shaded area.

resonant absorption features in the probe window. Examples of the fragment spectra can be found in the Appendix B.

To have a better comparability to the experimentally measured ΔOD, the fit amplitudes $\Delta a_j(t)$, together with the corresponding absorption spectra $S_j(\omega)$, with $j = 0, 1, 2, 3$, are used to reconstruct $\Delta\mathrm{OD}^{(\mathrm{rec.})}(E, t)$ (see Figure 6.15). The overall features of the experimental ΔOD, namely the gradual decrease of absorption in the vicinity of the $4\mathrm{d}_{5/2}$–σ^* resonance (E_{res}) and the transient increase in the low-energy region E_{low} are reproduced very well.

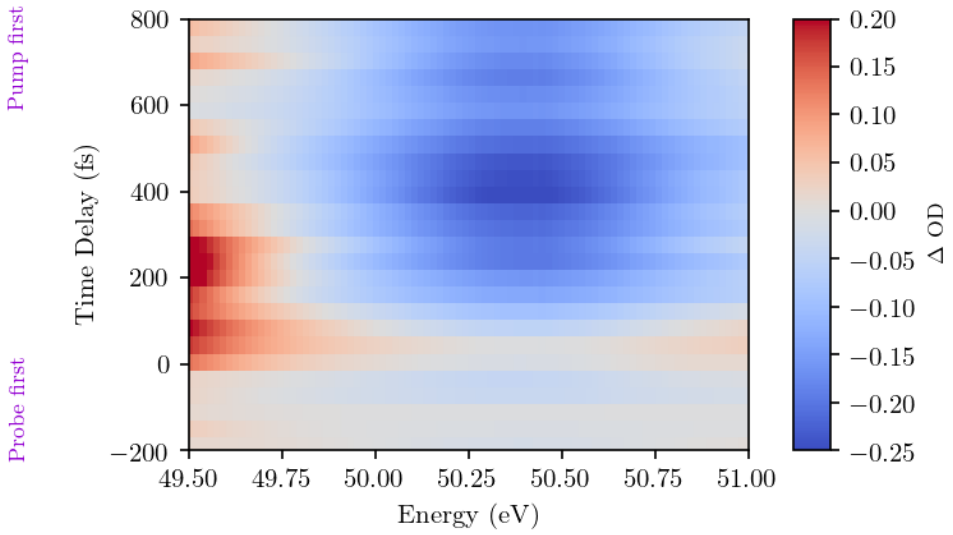

Figure 6.15.: To have a better comparability to the experimental data, the absorption spectra $S_j(E)$ and their respective absorption contributions $\Delta a_j(t)$ ($j = 0, 1, 2, 3$), are used to reconstruct $\Delta\mathrm{OD}^{(\mathrm{rec.})}(E,t)$. The main features of the experimental $\Delta\mathrm{OD}(E,t)$, specifically the gradual decrease of absorption around E_{res} and the transient increase and subsequent decay in $\Delta\mathrm{OD}(E,t)$ in the low-energy region (E_{low}) are reproduced very well (cf. Figure 6.9).

The reconstruction of $\Delta\mathrm{OD}^{(\mathrm{rec.})}$ can also be done selectively. For this, only individual components $\left[\Delta a_j(t) \times S_j(\omega)\right]$, with $j = 0, 1, 2, 3$, of Eq. (6.6) are used for the reconstruction. This enables to resolve each molecular geometry's contribution to the different absorption features. In Figure 6.16 the contributions of all molecular configurations 0,1,2,3 are depicted, starting from the top left panel in clockwise direction. As can be seen, the bleaching in absorption in the vicinity of the resonance E_{low} is exclusively caused by the dynamical evolution of the molecule's initial configuration 0. Furthermore, it can be seen that the emergence of geometry 2 is the main cause of the transient increase in absorption around E_{low}. Geometry 3 gradually adds to the absorption around E_{low}, while the total absorption is largely unaffected by geometry 1.

The connection from the fit model using the theoretically calculated absorption spectra [Eq. (6.6)] to the time constants retrieved via the global exponential model [Eq. (6.5)] is made via the partial reconstruction of $\Delta\mathrm{OD}^{(\mathrm{rec.})}$. Therefore, the partial reconstruction is performed for the two components:

$$\begin{aligned} \Delta\mathrm{OD}_{0,b}^{(\mathrm{rec.})}(E,t) &= \left[\Delta a_0(t) \times S_0(\omega) + b(t)\right], \\ \Delta\mathrm{OD}_{2}^{(\mathrm{rec.})}(E,t) &= \left[\Delta a_2(t) \times S_2(\omega)\right], \end{aligned} \tag{6.7}$$

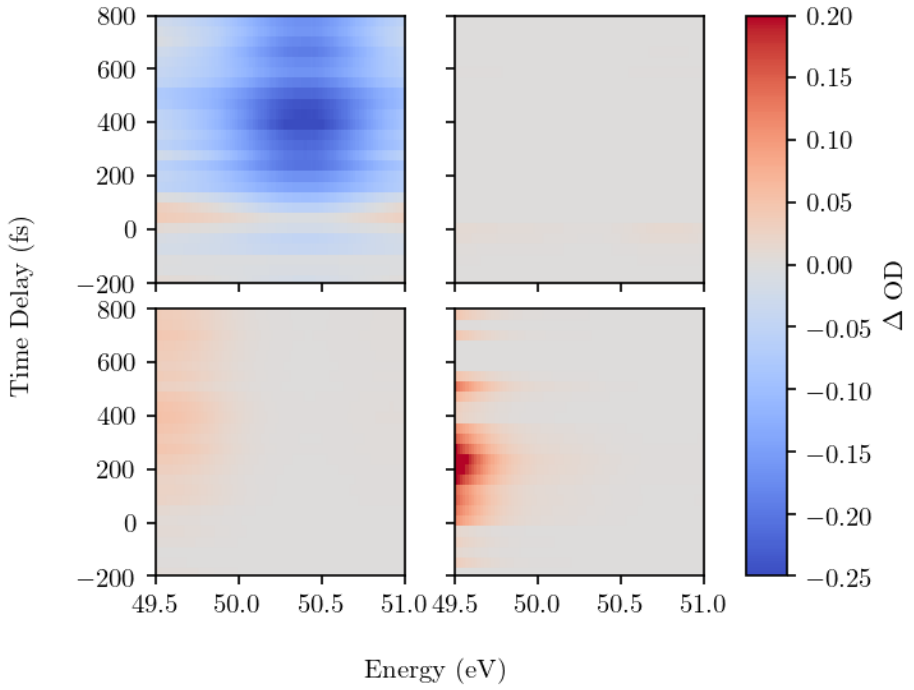

Figure 6.16.: Selectively reconstructed $\Delta\mathrm{OD}^{(\mathrm{rec.})}(E,t)$. The individual panels show only the absorption contributions of individual molecular configurations $\Delta\mathrm{OD}_j^{(\mathrm{rec.})}(E,t) = \left[\Delta a_j(t) \times S_j(\omega)\right]$ with $j = 0,\ldots,3$. From the top left in clockwise direction these are the contributions from geometry 0 to 3.

setting all other contributions to zero. The component $\Delta\mathrm{OD}_2^{(\mathrm{rec.})}(E,t)$, is spectrally integrated over E_{low}, while for the component $\Delta\mathrm{OD}_{0,b}^{(\mathrm{rec.})}(E,t)$ is spectrally integrated over E_{res}. The resulting lineouts are plotted in Figure 6.17, with the lineouts of the experimental ΔOD in the background (cf. Figure 6.10).

It is apparent that the decrease of absorption on resonance is dominated by the bleaching of the initial geometry 0, while the transient increase in absorption in the low-energy region (E_{low}) is predominantly caused by the temporal evolution of geometry 2. The observed dynamics can be explained by the two dissociation channels occurring in parallel (cf. Figure 6.11). On the one hand, the direct dissociation channel of the diiodomethane cation mainly manifests as the resonant decrease (E_{res}) of absorption with the time constant $\tau_1 = 166 \pm 11\,\mathrm{fs}$. On the other hand, the indirect dissociation channel, which involves an isomeric molecular geometry, leads to the transient increase in absorption in the lower-energy region (E_{low}). This feature appears more slowly than the IRF of the system (cf. Figure 6.17) and decays with the time constant $\tau_2 = 290 \pm 30\,\mathrm{fs}$, as revealed by the bi-exponential fit [Eq. (6.5)].

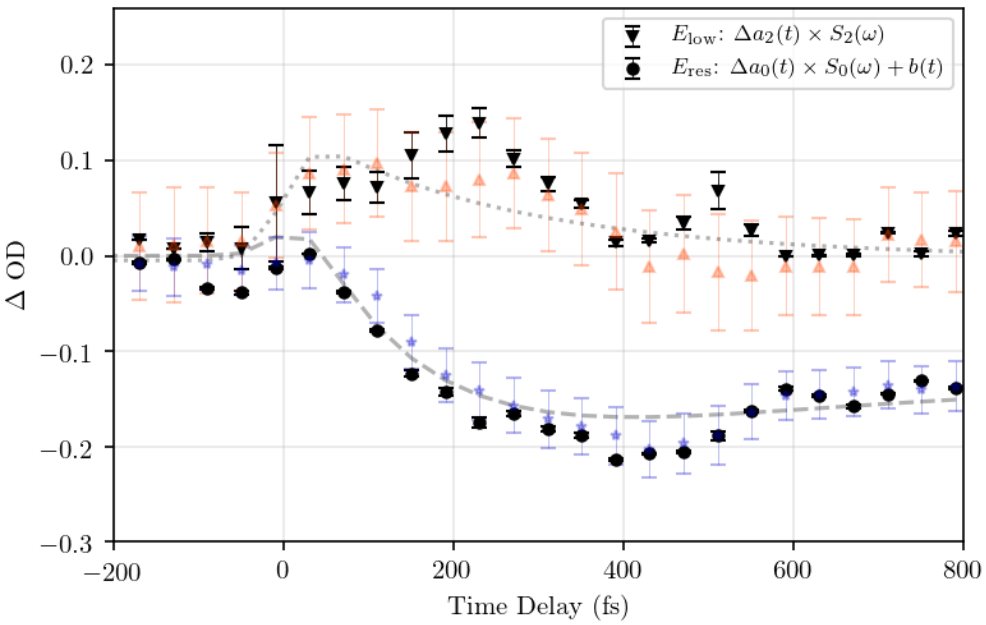

Figure 6.17.: Lineouts of the selectively reconstructed $\Delta\mathrm{OD}^{(\mathrm{rec.})}(E,t)$, with only specific channels (Δa_0, respectively Δa_2) included and all other channels set to zero. The lineouts of the experimental ΔOD are shown in the background for a better comparability (cf. Figure 6.10).

It has to be noted, that the pump pulse creates an ensemble of multiple excited states, whose pathways all contribute on average to the observed dynamics in this spectral range. The temporal evolution of the molecule's initial geometry and the isomeric geometry 2 hereby dominate the observed transient absorption features (cf. Figure 6.16, Figure 6.17). Through the performed analysis, we are able to reveal the relaxation pathways of this site-specifically excited molecule. The reconstructed absorption components that are reduced to the contribution of individual geometries ($\Delta\mathrm{OD}_{0,b}^{(\mathrm{rec.})}(E,t)$ and $\Delta\mathrm{OD}_{2}^{(\mathrm{rec.})}(E,t)$) show additional deviations as compared to the bi-exponential fit model (cf. Figure 6.17). This stems from the fact, that in the experiment multiple decaying pathways are naturally averaged, which is not the case when selecting individual channels, as is done here.

In the presented work, the prospect of all-XUV transient absorption spectroscopy as a powerful tool for the investigation of XUV-initiated femtosecond molecular dynamics is demonstrated. Through the high photon flux of the employed FEL radiation it is possible to perform site-specific XUV-pump–XUV-probe transient absorption spectroscopy, here applied in the vicinity of the iodine $4d_{5/2}$–σ^* absorption resonance. With the support of ab-initio calculated ionization spectra for the different

molecular geometries it was possible to follow the molecular relaxation pathways. The time constants of these parallel relaxation paths could be extracted through a global fit model. These results were obtained despite the limitations set by the relatively narrow probe spectrum of the FEL, which in this case is on the order of 0.5 eV FWHM[4]. In the future, these limitations are expected to be overcome by combining a high-harmonic XUV source as a broadband probe that spans multiple tens of eV with an intense FEL pump. The site-specific excitation with the FEL pump pulse can be retained by synchronization of the FEL pulses and the generating HHG laser [117]. Access to a broader bandwidth of XUV excitations can also be reached via novel two-color FEL operation modes [118, 119]. The availability of these schemes will make it possible to detect and identify a much wider range of bound final states of the molecular target. These include charged, as well as neutral molecular fragments [92, 120], which are inaccessible with the already widely used electron-ion spectroscopy schemes.

The presented experiment can be seen as a first step in implementing a novel experimental tool for the study of ultrafast molecular dynamics. However, the full potential of site-specific FEL excitations will only be unleashed when their combination with a broadband XUV probe is realized. A wide range of experimental schemes can be imagined, which possibly can be realized in this way. One such scheme would be the site-selective excitation of targets with two different absorption sites via a resonant FEL pump pulse. In combination with a broadband XUV probe pulse, the transport of excitation throughout a molecule can in principle be studied. The realization of such a scheme could find application in the study of large biomolecules with their different functional groups.

[4]This bandwidth of 1 % of the given photon energy is typical for SASE FELs [58].

7. XUV-initiated dissociation dynamics of oxygen (O_2)

In this chapter a second all-XUV transient absorption spectroscopy experiment using SASE FEL pulses is presented. The experimental settings and the FEL parameters are identical to the experiment performed in diiodomethane, as presented in chapter 6. For the experiment presented in this chapter, the oxygen molecule was chosen as a target. Oxygen is one of the most important molecules for (human) life on earth. More than a fifth of earth's atmosphere [121] and roughly half of earth's crust [122] (in the form of oxides) is made from oxygen. It plays a central role in combustion processes [123] and in the metabolism of many life forms [124]. In the shape of the ozone (O_3) layer it protects life on earth from harmful ultraviolet radiation [121].

On top of that, as a diatomic molecule, it has the potential to serve as a test system for the theoretical calculation of nuclear wave packet dynamics [125–128]. Until recently, such experiments were mainly performed using few-cycle near-infrared (NIR) laser pulses in time-resolved pump–probe spectroscopy experiments [127–130]. The highly intense NIR pulses, however, introduce strong couplings between electronic states. Therefore, rather the field-dressed potential-energy curves (PECs) are probed, instead of the more fundamental field-free potential energy curves.

The advent of XUV free-electron lasers enabled the implementation of XUV-pump–XUV-probe schemes for the investigation of such dynamics, as was discussed already in chapter 6. The first XUV pulse ionizes the molecule, thereby initiating a nuclear wave-packet. Only a small number of XUV photons is needed for this ionization step, which is in contrast to the multiphoton excitation with an NIR pulse. The hereby introduced coupling between excited states is negligible. The second XUV pulse subsequently probes the evolution of the initiated nuclear wavepacket on the almost field-free potential energy curves. The probing can be either done by further ionization of the target [131, 132], or via the detection of the molecule's absorption spectrum as a function of the pump-probe time delay, as is presented in this work.

7.1. Time-dependent absorption lines

For the presented measurement, the experimental scheme, as well as all settings were exactly the same as delineated in chapter 6. The employed FEL pulses have a photon energy of $\sim 50\,\mathrm{eV}$, a pulse duration of $65 \pm 15\,\mathrm{fs}$ and an intensity in the $10^{13}\,\mathrm{W\,m^{-2}}$ regime. Pump and probe pulses are generated by geometrically splitting the incoming FEL pulses in the FLASH BL2 autocorrelator (see section 4.2 and chapter 6). The spectra of the probe pulse, transmitted through an oxygen sample are detected as a function of the pump-probe time delay. Unfortunately, the set target pressure was not stable during the experimental run but fluctuated between 40 mbar and 45 mbar with an average of $\bar{p}_{\mathrm{target}} = 41\,\mathrm{mbar}$, as can be seen in Figure 7.1. Since

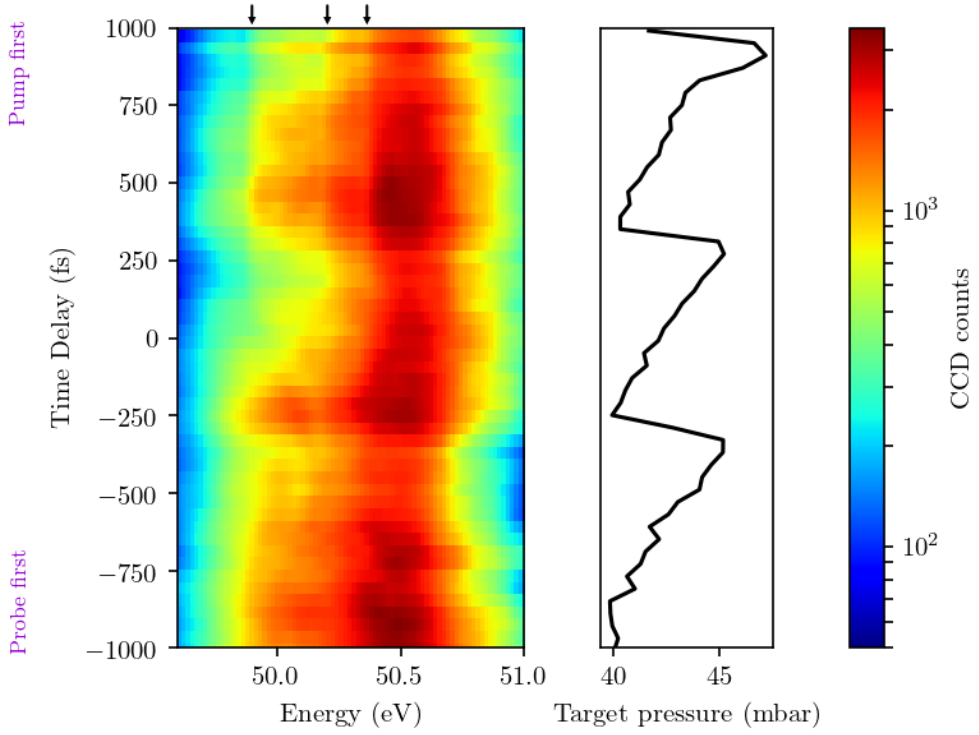

Figure 7.1.: Left panel: Time-dependent transmission of the probe spectrum through the oxygen target. The emerging absorption lines are indicated via small arrows on top of the panel. Right panel: Target pressure.

the absorption coefficient in Lambert-Beer's law is proportional to the density of the absorbing medium (cf. Eq. 2.18, Eq. 2.19), this directly translates into fluctuations of the transmitted probe intensity (see Figure 7.1). Regions with high target pressures hereby lead to low transmission and vice versa. Nevertheless, some sharp absorption features can already be recognized in the transmission data for positive time delays,

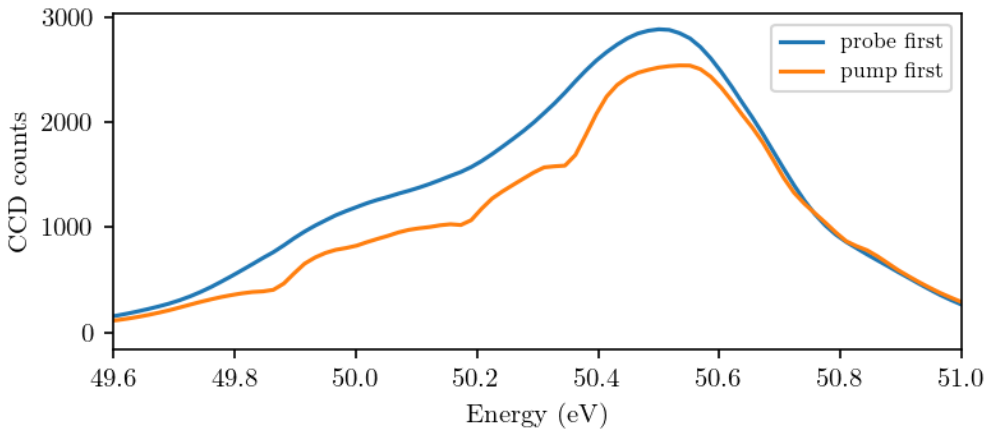

Figure 7.2.: Average transmission spectra of the probe pulse for the cases of the probe pulse preceding the pump by more than 400 fs (blue) and vice versa (orange). For the case of the pump pulse passing the oxygen target first, sharp absorption features can be observed in the probe spectrum. They are the result of multiple ionization of the O_2 target by the pump and subsequent dissociation into O^{2+}.

where the pump pulse precedes the probe pulse (marked by the black arrows in Figure 7.1). They are not present for negative time delays. The origin of these absorption lines will be investigated further in the following.

In Figure 7.2, the average transmitted spectrum of the probe pulse is shown for the case were the pump pulse precedes the probe pulse by more than 400 fs, as well as for the opposite case. The emergence of sharp absorption features is clearly visible for the case of a preceding pump pulse in addition to the reduction of the overall count rate via increased nonresonant absorption. These pump-induced absorption changes can be calculated as follows and can be seen in the lower panel of Figure 7.3:

$$\Delta \mathrm{OD}_{\text{pump induced}}(\omega) = -\log_{10}\left(\frac{I_{\text{pump first}}(\omega)}{I_{\text{probe first}}(\omega)}\right). \tag{7.1}$$

In the top panel of Figure 7.3, the energetic positions and relative intensities of several transitions of the O^{2+} cation are plotted. The line parameters are taken from reference [133] and are summarized in Table 7.1. The the letters A-E are assigned to individual absorption features for easier identification. Feature A refers to all transitions from the $2p^2 - 2p5d$ triplet, since they are indistinguishable with the available spectrometer resolution. An unambiguous assignment of the observed absorption resonances to transitions of the O^{2+} cation is possible. The observed resonances are summarized in Table 7.1.

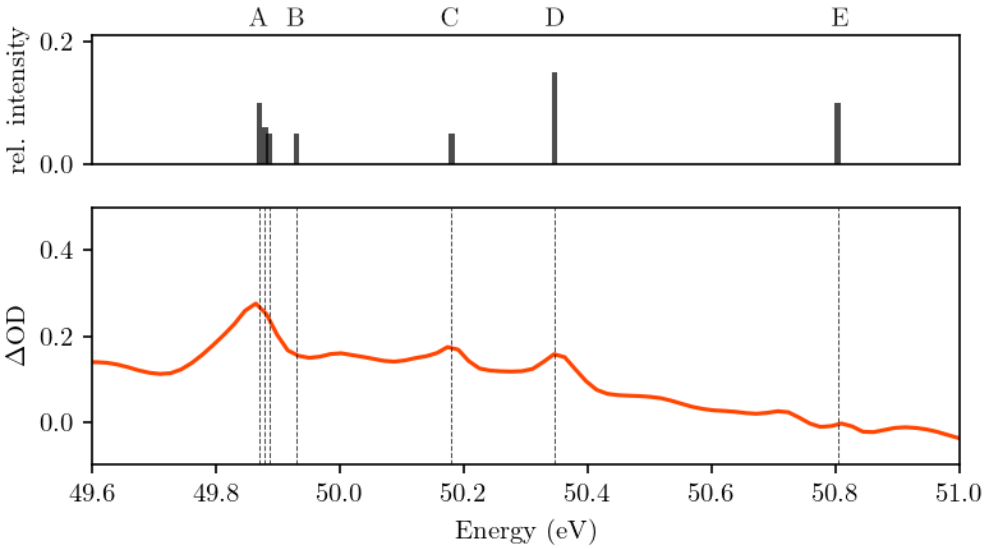

Figure 7.3.: Pump-induced absorption changes in the O_2 target, including several absorption resonances (lower panel) and their assignment to known absorption resonances of O^{2+} from literature [133] (upper panel).

Table 7.1.: Parameters of O^{2+} absorption lines [133].

Transition	**Term Scheme**	**Energy (eV)**
A: $2p^2 - 2p5d$	$(g^3P_2) - (^3D^o_3)$	49.87
A: $2p^2 - 2p5d$	$(g^3P_1) - (^3D^o_2)$	49.88
A: $2p^2 - 2p5d$	$(g^3P_0) - (^3D^o_1)$	49.89
B: $2p^2 - 2p7d$	$(^1D_2) - (^1F^o_3)$	49.93
C: $2s^22p^2 - 2s2p^23p$	$(^1D_2) - (^1F^o_3)$	50.18
D: $2s^22p^2 - 2s2p^23p$	$(^1D_2) - (^1D^o_2)$	50.35
E: $2s^22p^2 - 2s2p^23p$	$(^1D_2) - (^1P^o_1)$	50.80

The observed O^{2+} absorption resonances have widths on the order of a few 10 meV, which is much narrower than the width of the average FEL spectrum, that is on the order of several 100 meV. To determine the time constants with which these absorption lines appear, a reference spectrum is therefore constructed via a Fourier bandpass filter of the probe transmission spectrum $I_{\text{probe}}(\omega, t)$ for every time delay step t. This reconstructed reference intrinsically mirrors the fluctuations through the pressure variation of the transmitted spectrum. Calculating the optical density with the reconstructed reference, thereby alleviates the fluctuations in the nonresonant part of the OD. Nevertheless, the data has to be normalized by the relative pressure

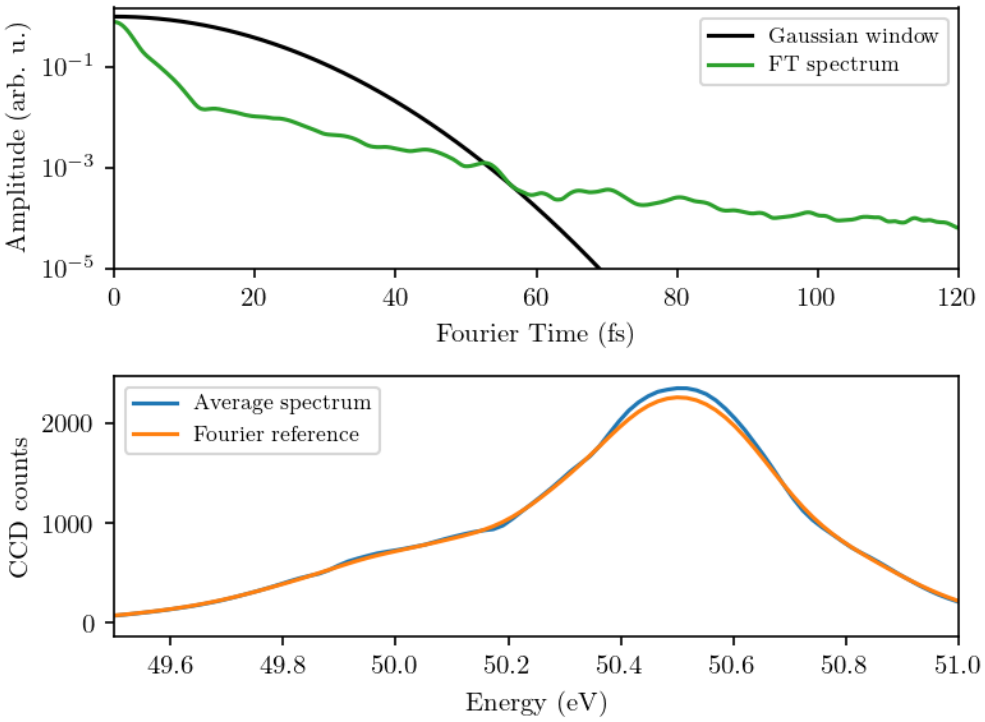

Figure 7.4.: Upper panel: Fourier transformed (FT) spectrum of the average transmitted spectrum (green). Gaussian low-pass filter (black). Lower panel: Average probe transmision spectrum (blue). Reference spectrum generated with the described Fourier filtering method (orange).

fluctuation to get the correct strengths for the resonant absorption features, since the OD is proportional to the pressure. In a first step, the transmitted spectrum is tapered with a $\cos^2$-function to suppress the image noise in regions where no light hits the CCD chip. This noise would otherwise lead to artificial high-frequency components in the Fourier-transformed (FT) spectrum. The tapered transmission spectrum is then Fourier transformed along its energy axis. An example of this FT spectrum can be found in the upper panel of Figure 7.4. The Gaussian low-pass filter can also be seen in this plot. It is defined as:

$$w(t) = \exp\left(-\frac{1}{2}\left(\frac{t}{\sigma}\right)^2\right). \tag{7.2}$$

Its width σ is chosen in a way that it best approximates the region in the low-energy flank of the transmitted spectrum where the absorption lines of interest lie. This leads to deviations of the Fourier reference from the real transmitted spectrum in the region of the peak between 50.4 eV and 50.7 eV. However, none of the absorption

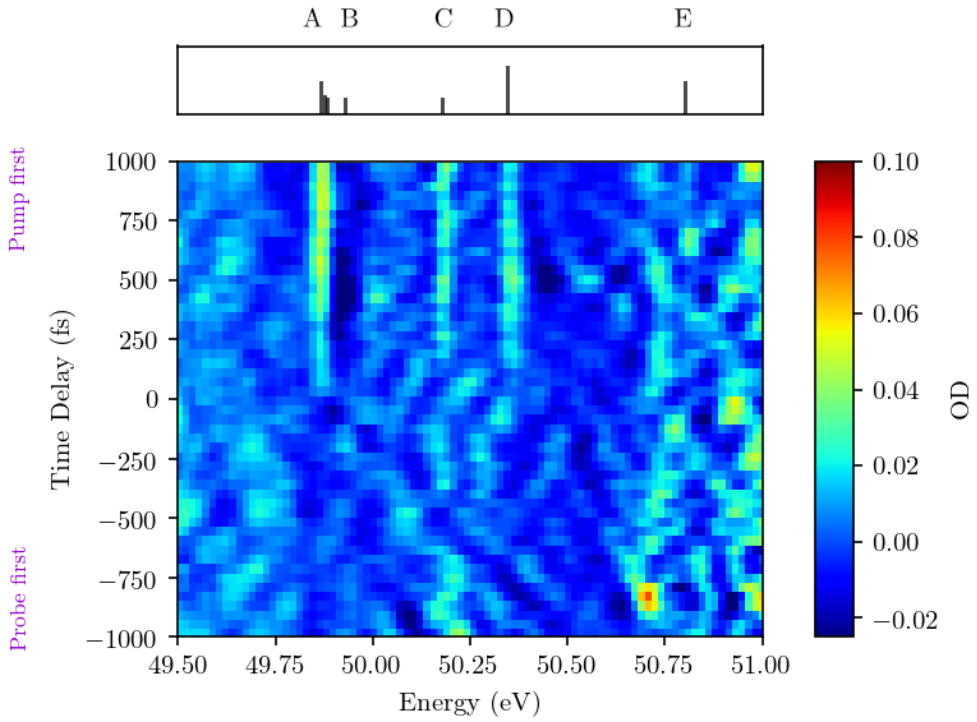

Figure 7.5.: Time-dependent optical density calculated with the generated Fourier reference spectra. The emergence of absorption features A, C and D (cf. Table 7.1) is clearly visible over the course of the time delay. The other absorption lines are hidden in the noise floor of the OD.

lines of interest lie in this spectral region (cf. Figure 7.2). The time-dependent optical density, calculated with the generated Fourier references, can be seen in Figure 7.5. It has to be noted that, albeit the fluctuations in the transmitted spectrum being removed by calculating the optical density with the generated Fourier reference spectra, the strengths of the absorption lines are also altered through the variation of the target density. Therefore, the optical density is normalized by the relative pressure fluctuation, since the absorption cross section is proportional to the target density (cf. Eq. 2.18, Eq. 2.19).

Three absorption lines emerge for positive time delays. The most prominent feature can be assigned to the triplet of $2p^2 - 2p5d$ around 49.88 eV. Additionally, two signatures of the $2s^22p^2 - 2s2p^23p$ transition at 50.18 eV and 50.35 eV can be observed, while the remaining absorption lines remain hidden in the noise level of the optical density. The lineouts through the energy regions of the absorption features A, C, D and E can be found in Figure 7.6. The lineout of absorption feature B is omitted here, since it is energetically very close to absorption line A. It is suppressed by an

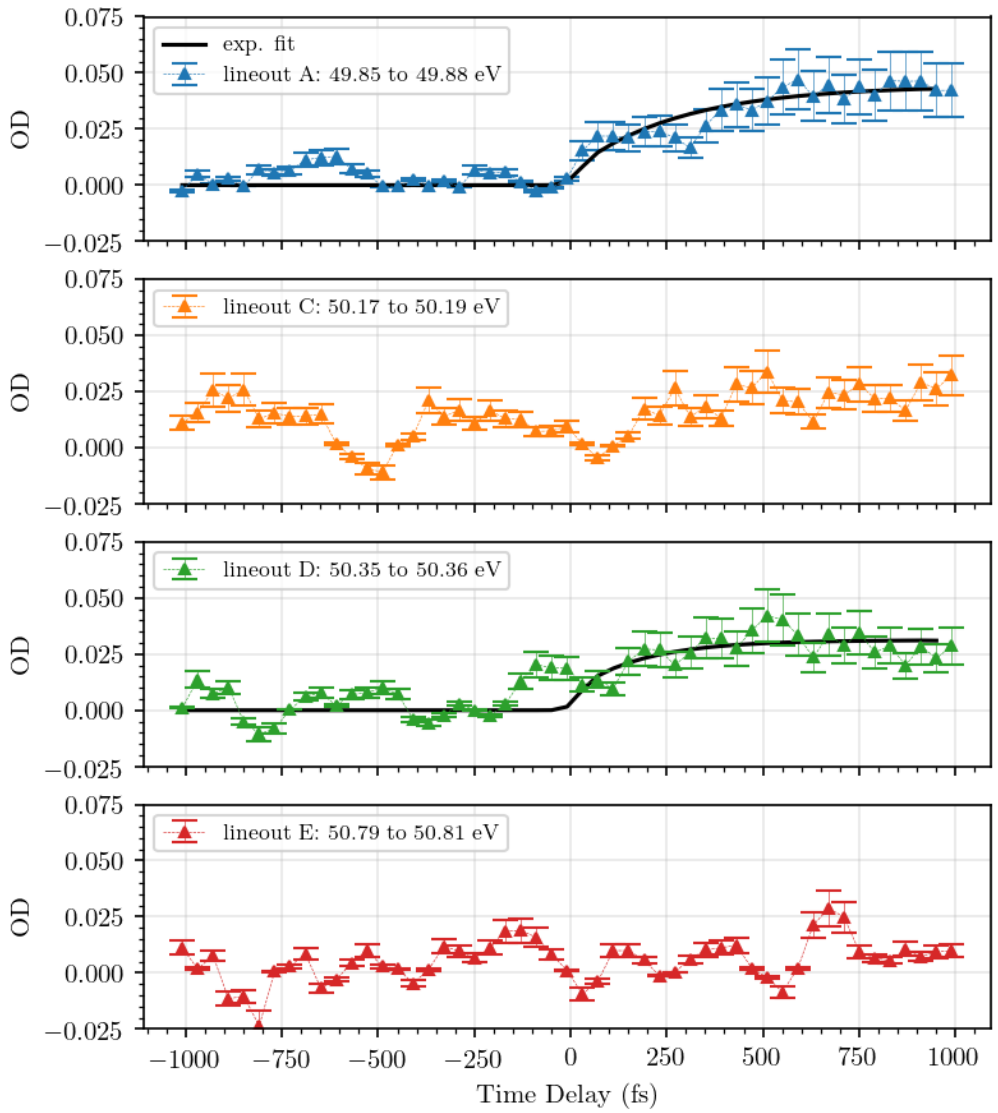

Figure 7.6.: Lineouts of the OD, averaged over the absorption resonances A, C, D and E. The lineouts of A and D are fit with the exponential model introduced in Eq. (7.3). The results of this fit are summarized in Table 7.2.

artifact of the Fourier filter as can be seen in Figure 7.5. The error bars of the lineouts are calculated from the relative error of the pulse energy of 28 %, since it is difficult to estimate the error of the Fourier reference. The lineouts of the most prominent absorption features A and D, are fit with an exponential model, similar to the global fit model introduced in Eq. (6.5):

$$\Delta\mathrm{OD}(E,t) = y(E) + \mathrm{IRF}(t) * \left[\Theta(t) \times \left(a(E) + b(E)e^{-t/\tau}\right)\right]. \tag{7.3}$$

Here, $y(E)$ is a time-independent offset, IRF(t) is the instrument response function and $\Theta(t)$ is the heaviside step function. The $*$-symbol denotes the convolution between instrument response function and the function which describes the dynamics, while the $\times$-symbol denotes multiplication. $a(E)$ and $b(E)$ are fit amplitudes, while τ is the time constant of the exponential rise of the absorption line. The fits are performed for three different widths σ of the Fourier filter [Eq. (7.2)] to get an estimate of its influence on the time scales. The results of the fit are summarized in Table 7.2. All

Table 7.2.: Results of fitting Eq. (7.3) to the lineouts A and D.

	Filter 1 ($\sigma_1 = 19\,\text{fs}$)	**Filter 2** ($\sigma_2 = 23\,\text{fs}$)	**Filter 3** ($\sigma_3 = 27\,\text{fs}$)	**Average**
A:	$\tau_{A1} = 300 \pm 60\,\text{fs}$	$\tau_{A2} = 290 \pm 50\,\text{fs}$	$\tau_{A3} = 270 \pm 50\,\text{fs}$	$\bar{\tau}_A = 290 \pm 30\,\text{fs}$
D:	$\tau_{D1} = 178 \pm 79\,\text{fs}$	$\tau_{D2} = 177 \pm 77\,\text{fs}$	$\tau_{D3} = 186 \pm 73\,\text{fs}$	$\bar{\tau}_D = 180 \pm 44\,\text{fs}$

three results per lineout agree well within the error margins. A strong influence of the width of the Gaussian low-pass filter on the resulting time scales can thus be ruled out.

As can be seen in Figure 7.6, there is an increase in absorption feature D before the temporal overlap of pump and probe pulses. This is most likely linked to an artifact of the Fourier filter as can be seen in Figure 7.5. The fit model mostly ignores this artifact through the heaviside step function $\Theta(t)$. Nevertheless, the results of fitting lineout D should be regarded with caution. The emergence of the absorption resonance A of the $2p^2 - 2p5d$ triplet with a time constant of $\bar{\tau}_A = 290 \pm 30\,\text{fs}$ is reproduced reasonably well by the exponential fit model [Eq. (7.3)].

7.2. The dissociation mechanism

As was discussed in the previous section, the observed absorption lines stem from the O^{2+} cation. To generate this doubly charged cation via Coulomb explosion, the oxygen molecule has to be ionized at least thrice. For this, the interaction with at least two 50 eV photons is needed to introduce the required 81.60 eV into the system [134].

$$O_2 + 2\,\gamma \longrightarrow O_2^{3+} \longrightarrow O^+ + O^{2+} \tag{7.4}$$

Under the assumption of this direct triple ionization, the dissociation dynamics of O_2 will be investigated with a simple classical model for the dissociation of a diatomic

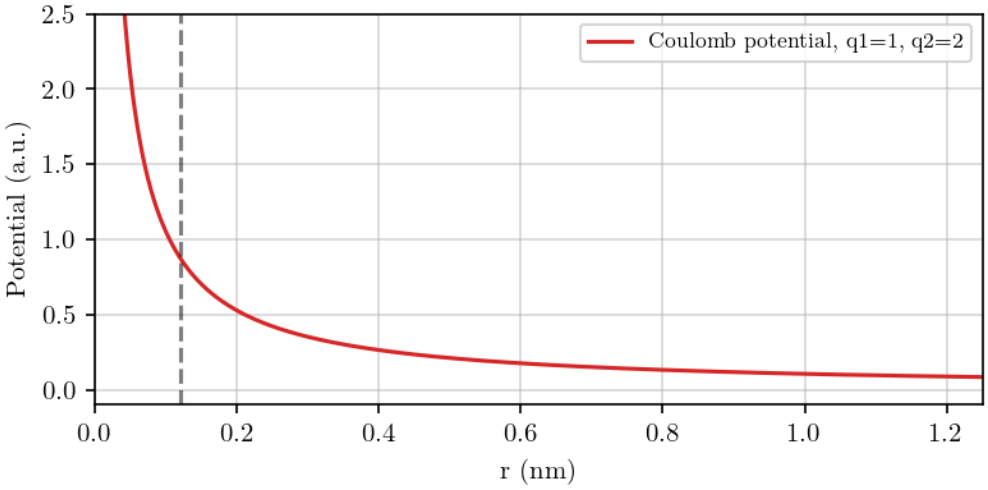

Figure 7.7.: Coulomb potential with charges $q_1 = 1$ and $q_2 = 2$. The dashed vertical line indicates the equilibrium distance of O_2 of $r_0 = 1.208\,\text{Å}$.

molecule. The real dissociating potential energy curve of the oxygen molecule, is hereby approximated by a Coulomb potential:

$$V(r) = \frac{q_1\, q_2}{r}, \tag{7.5}$$

with the fragment charges q_1, q_2. The Coulomb potential for the dissociation channel (7.4) with $q_1 = 1$, $q_2 = 2$ is shown in Figure 7.7. The pump step is implemented by placing a point-like particle in this potential at the equilibrium distance $r_0 = 1.208\,\text{Å}$ of the neutral oxygen molecule according to the Franck-Condon principle. The particle has the reduced mass $\mu = \frac{m_1 m_2}{m_1 + m2}$ and the initial velocity $v_0 = 0$. The relaxation path of the particle is calculated by numerical integration along the reaction coordinate r. Therefore, the reaction coordinate r is discretized into equally sized incremental steps $\Delta R = r_i - r_{i-1}$. From the potential, the acceleration a_i of the particle can be calculated at every point i along the reaction coordinate:

$$a_i = -\frac{1}{\mu}\frac{\Delta V_i}{\Delta R}, \tag{7.6}$$

where $\Delta V_i = V(r_i) - V(r_{i-1})$. From this, the time that is needed to go from one point i of the reaction coordinate to the next $(i + 1)$ is calculated:

$$\Delta t_{i+1} = \frac{\Delta R}{\sqrt{(v_i^2 + 2a_i \Delta R)}}, \tag{7.7}$$

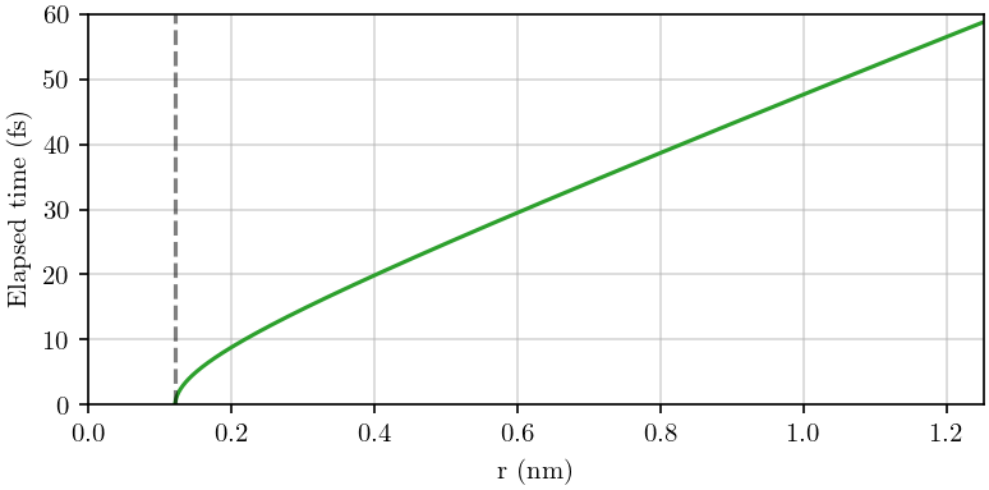

Figure 7.8.: Total travel time of a particle with the reduced mass of oxygen placed at $r_0 = 1.208\,\text{Å}$ (dashed vertical line) in a 2/R potential. The particle reaches ten times its initial distance in about 60 fs.

with the momentary velocity of the particle v_i which is initially $v_0 = 0$. It is updated for every step via the total kinetic energy the particle has after the respective step:

$$v_i = \sqrt{2(V_0 - V_i)/\mu}, \tag{7.8}$$

where V_0 is the particle's initial potential energy and V_i is its potential energy at every step i. To calculate the total elapsed time, the incremental time steps Δt_i are simply summed up.

A particle with the reduced mass of the oxygen molecule is initiated into a 2/R Coulomb potential at the equilibrium distance of the oxygen molecule of $r_0 = 1.208\,\text{Å}$. As can be seen in Figure 7.8, the total elapsed time until the distance between the fragments has reached 10 times r_0 is roughly 60 fs. Neglecting large Rydberg orbitals, the molecule might be considered as fully dissociated at this point. The possible influence of such Rydberg orbitals on the observed dissociation process has to be investigated further. It is apparent, that the expected dissociation time is on the order of several ten femtoseconds. The observed absorption lines of the dissociation fragments, however, emerge with time constants on the order of a few hundred femtoseconds. A previous ion-ion coincidence study on the dissociation dynamics of oxygen under the influence of intense XUV light has suggested that additional intermediate states play a role in this dissociation process [132]. Another ion-ion coincidence measurement, albeit using an optical pump step, has suggested that the

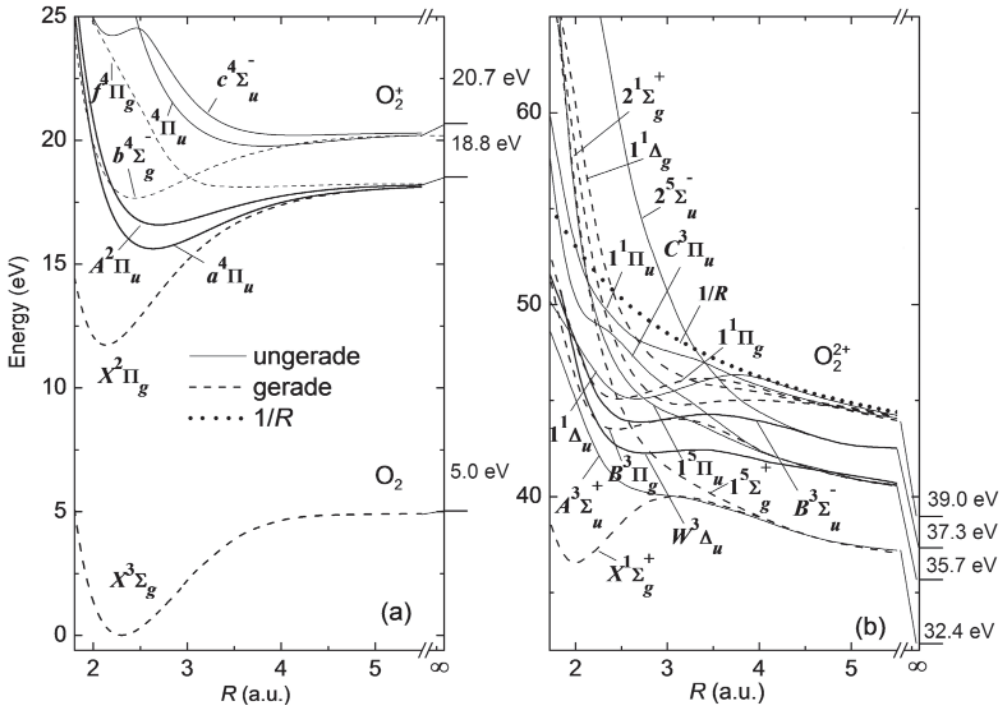

Figure 7.9.: Oxygen PECs, adapted from reference [132].

involved potential energy curves are non-Coulombic for small internuclear distances below 3 Å [134]. This is not surprising considering the richness of potential energy curves within this energy range, as can be seen for the case of doubly-charged oxygen in Figure 7.9.

It is also possible that the molecule's dissociation path starts from the lower charge state O_2^{2+} and involves the further ionization of already fragmented ions.

$$\begin{aligned} O_2 + \gamma &\longrightarrow O_2^{2+} \longrightarrow O^+ + O^+ \\ O^+ + \gamma &\longrightarrow O^{2+} \end{aligned} \tag{7.9}$$

However, the dissociation along the hereby involved 1/R potential takes only marginally longer as in the 2/R case, as can be seen in Figure 7.10.

The neutral dissociation of oxygen is in principle possible, which could explain the observed dissociation time constant of 290 fs. However, this pathway seems unlikely, since the employed photon energy 50 eV is already far above the double ionization threshold of O_2 of ~ 36 eV. Nevertheless, this pathway should be investigated in more detail.

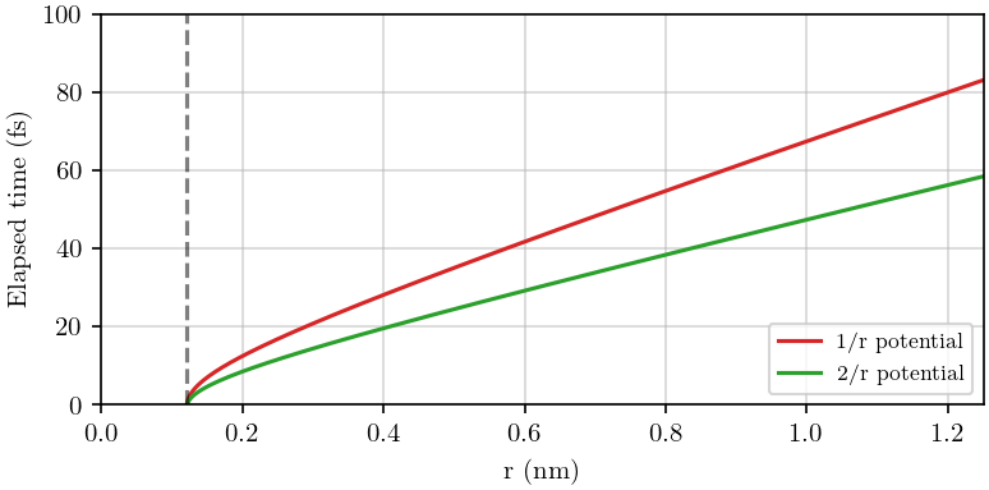

Figure 7.10.: Comparison of the travel times of a particle initiated into a 1/R (red) and 2/R (green) Coulomb potential.

Support from theory is needed for a better understanding of the processes involved in the observed ultrafast dissociation of the oxygen molecule. Nevertheless, the potential of the presented XUV-pump–XUV-probe transient absorption spectroscopy for the investigation of bound-state dynamics in dissociating molecules is demonstrated. The extension to a broader probe spectrum, as discussed in chapter 6, will tremendously increase the possibilities of this technique, since access to a much wider range of intermediate and final states will be granted in this way. The advantage of transient absorption spectroscopy over ion spectroscopy experiments hereby lies in the access to the bound state dynamics of ionic and neutral fragments.

8. Conclusion & Outlook

The main topic of this work is the implementation of XUV-pump–XUV-probe transient absorption spectroscopy at the FEL FLASH and its application to the ultrafast dissociation dynamics of the molecules diiodomethane (CH_2I_2) and oxygen (O_2).

In the case of the diiodomethane target, all-XUV transient absorption spectroscopy was performed near the site-specific $4d_{5/2}$–σ^* core-to-valence transition. A dynamical change in absorbance over the course of the pump-probe time delay was observed. The origin of this transient absorption change could be linked to a nontrivial dissociation process, which includes a direct and an indirect dissociation channel. With the help of ab-initio calculated absorption spectra for different molecular configurations of the cation, it was found that the indirect dissociation path includes isomeric geometries of the molecular cation. The involved time constants of the two channels could be extracted via a global exponential fit model.

In the case of oxygen, the fragmentation of the molecule was initiated via (multiple) ionization of the target by the pump pulse. The emergence of sharp absorption features in the probe spectrum was observed for the case of a preceding pump pulse. The observed absorption resonances could be assigned to transitions in the O^{2+} cation. An exponential fit model was employed to determine the time constants of the rise of these resonances. Additionally, a simple classical model was deployed to model the Coulomb explosion of an ionized oxygen molecule along Coulomb potentials of different charge states.

Both of the presented experiments were conducted with a newly constructed experimental setup. It was designed with the goal of flexible operation at either FEL sources, or with a table-top high-harmonic source.

The experiments highlighted in this work were, to the best of the author's knowledge, the first all-XUV transient absorption spectroscopy studies on molecular dynamics at FLASH. The results could be obtained, despite the relatively narrow probe spectrum of the FEL of 0.5 eV, which highlights the potential of the introduced experimental scheme for future studies. The combination of an intense FEL pump with a broadband

(spanning multiple tens of eV) high-harmonic generated probe, or novel two-color FEL operation modes, will give access to a much wider range of final states while retaining the site-specific excitation step. The probed quantities include bound states of the neutral and ionized molecular target, as well as charged and neutral molecular and atomic fragments, thereby unleashing the full potential of all-XUV transient absorption spectroscopy.

One conceivable target that benefits from the combination of a site-specific excitation step and broadband probing is a molecule with several different XUV absorption sites (e.g. $Cl{-}(CH_2)_x{-}I$). Resonant site-specific excitation of one of the absorption sites by the FEL, together with broadband time-resolved probing could give access to the propagation of electronic excitation throughout a molecule. An extension of this proposal would be the study of biomolecules with multiple absorbing functional groups.

A. Appendix A

As was discussed in chapter 6.3, a systematic deviation from the real OD can be observed in the diiodomethane measurement due to the unequal pump and probe spectra. To correct for it, a reference measurement without a gas target in the interaction cell is taken. The optical density of this measured reference shows the same trend as the diiodomethane OD. A temporal average of the optical densities of measured reference and diiodomethane target can be seen in Figure A.1. The OD of the measured reference represents the systematic error in the data that arises from the unequal pump and probe spectra. This systematic error can be corrected for by

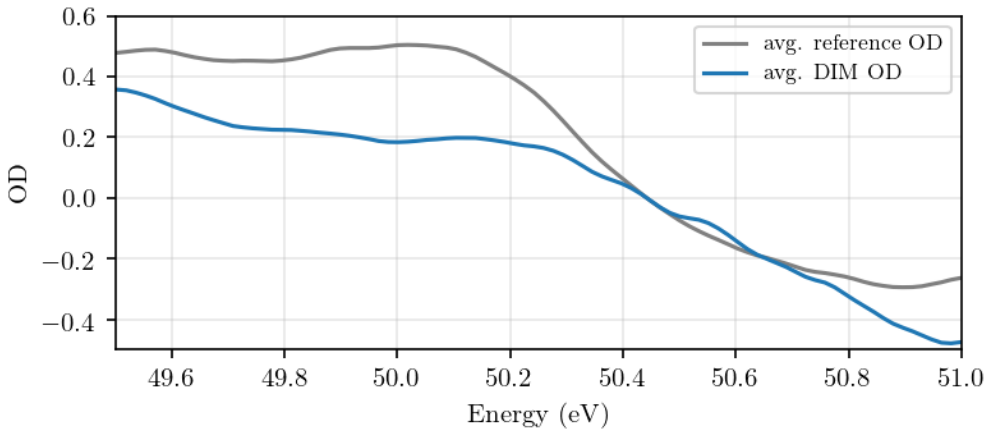

Figure A.1.: Average OD of the measured Reference

subtracting the time-averaged OD of the measured reference from the sample OD. The mathematical representation of this approach can be found in Eq. (A.1):

$$\begin{aligned} \mathrm{OD}_{\mathrm{DIM}} &= \widetilde{\mathrm{OD}}_{\mathrm{DIM}} - \mathrm{OD}_{\text{meas. ref.}} \\ &= -\left[\log_{10}\left(\frac{I_{\text{probe, DIM}}(\omega,t)}{I_{\text{online ref.}}(\omega,t)}\right) - \log_{10}\left(\frac{I_{\text{meas. ref.}}(\omega)}{I_{\text{online ref.}}(\omega)}\right)\right] \\ &\simeq -\log_{10}\left(\frac{I_{\text{probe, DIM}}(\omega,t)}{I_{\text{meas. ref.}}(\omega)}\right), \end{aligned} \tag{A.1}$$

where $\mathrm{OD}_{\mathrm{DIM}}$ is the real optical density of the DIM sample, $\widetilde{\mathrm{OD}}_{\mathrm{DIM}}$ is the experimental OD still including the systematic error and $\mathrm{OD}_{\mathrm{meas.\ ref.}}$ is the optical density of the reference measurement. In principle the optical density could directly be calculated with a measured reference. The advantage in first calculating the optical densities of the diiodomethane target and the measured reference with their corresponding online reference spectra lies in the statistical nature of the SASE FEL pulses. The SASE spectra show large fluctuations in intensity and wavelength between shots (cf. section 3.4). Having a direct reference spectrum for every single SASE pulse thereby greatly reduces the noise level of the data.

The optical density that results in applying Eq. (A.1) to the data is shown in Figure A.2. The $4d_{5/2}$–σ^* absorption resonance can be clearly seen between $\sim 50.2\,\mathrm{eV}$ and $\sim 50.9\,\mathrm{eV}$ (cf. Figure 6.2). A decrease of this absorption resonance can be observed for positive time delays, where the pump pulse precedes the probe pulse. An additional absorption feature transiently appears around $t = 200\,\mathrm{fs}$ at the energy of $49.5\,\mathrm{eV}$. Both of these features can already be seen in Figure 6.7.

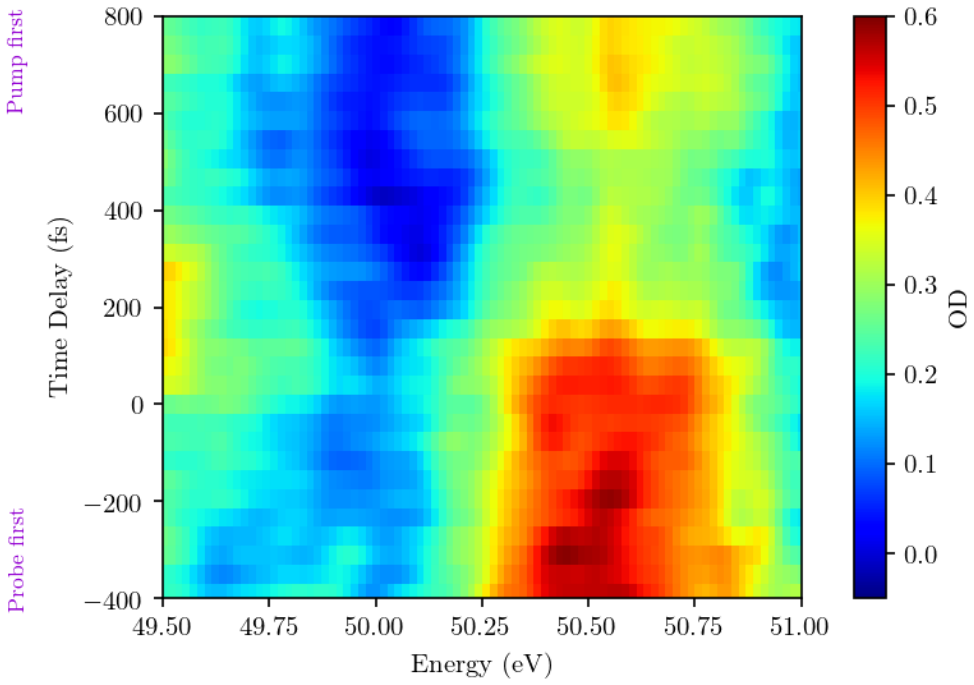

Figure A.2.: DIM OD

To illustrate the equivalency of the two approaches, the ΔOD directly calculated from the raw $\widetilde{\mathrm{OD}}$, as well as the ΔOD calculated from the OD with the systematic

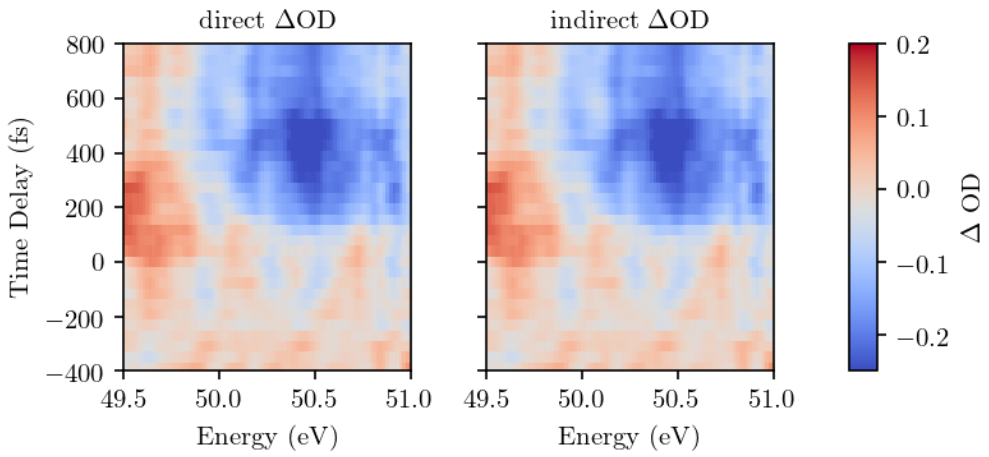

Figure A.3.: DIM ΔOD

error already removed are shown side-by-side in Figure A.3. The two methods lead to virtually identical results. This is a strong indication that the average OD of the reference measurement without a target (see Figure A.1) is a good measure for the systematic error.

B. Appendix B

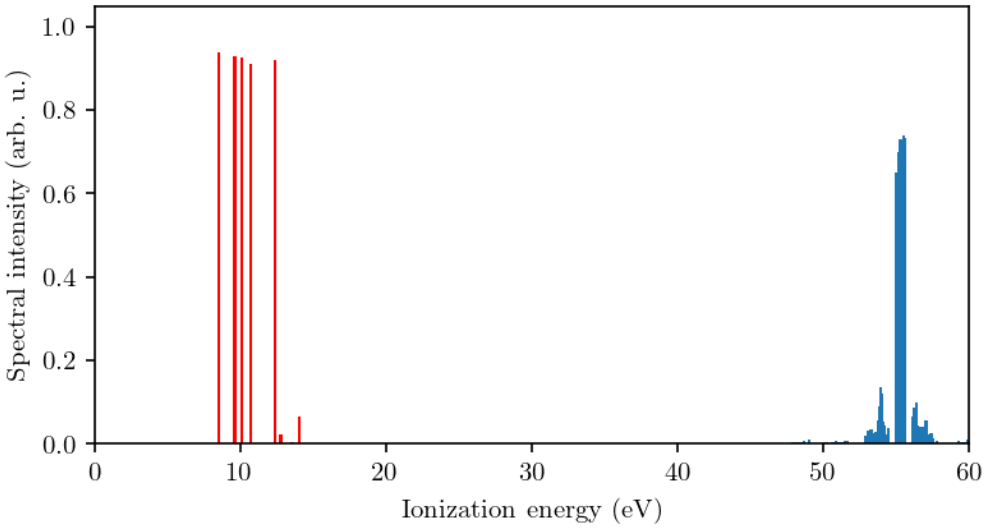

Figure B.1.: Ionization spectrum of cationic geometry 1.

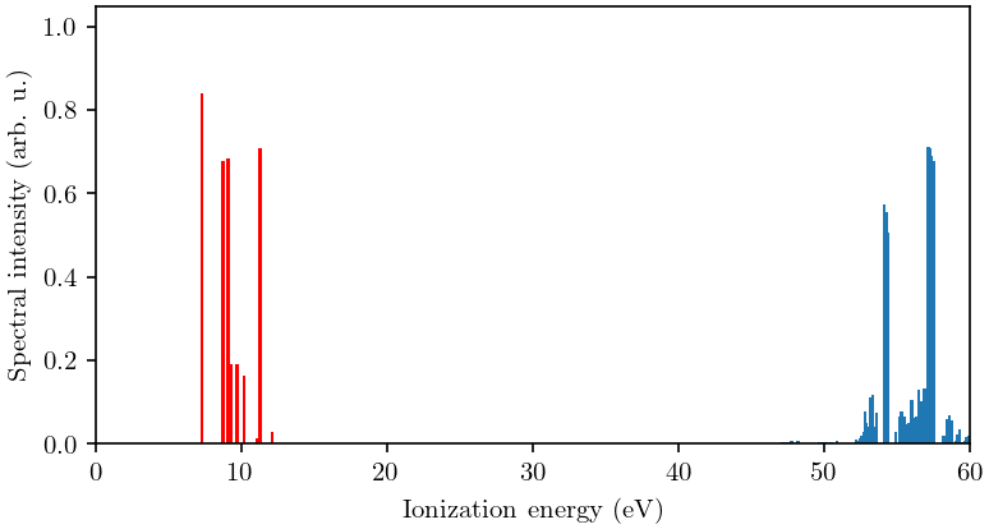

Figure B.2.: Ionization spectrum of cationic geometry 2.

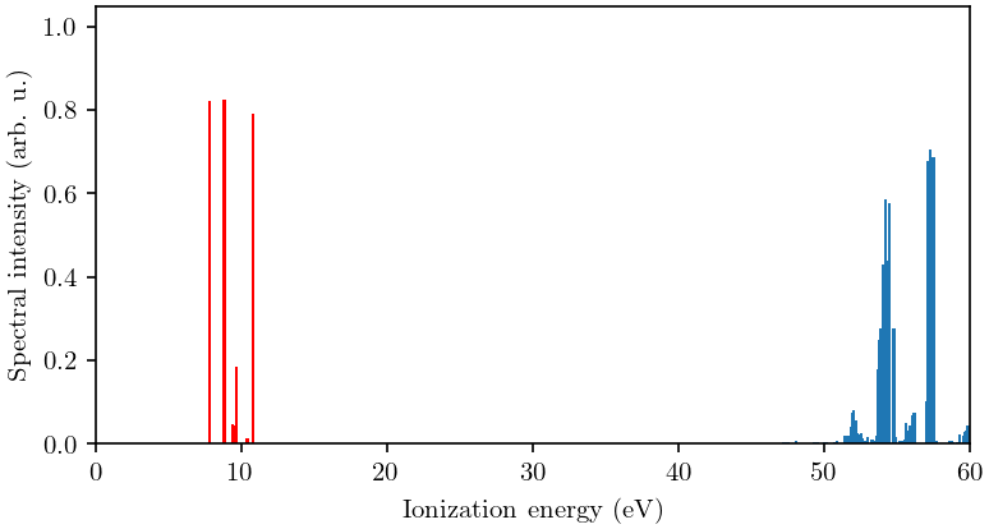

Figure B.3.: Ionization spectrum of cationic geometry 3.

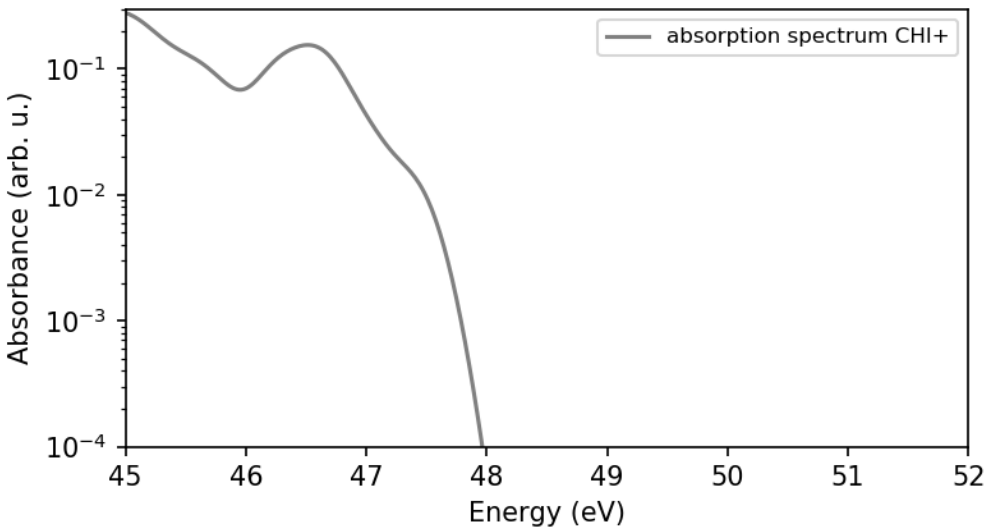

Figure B.4.: Absorption spectrum of the molecular fragment CHI^+, calculated along the lines described in chapter 6.3.2. It can be seen, that it has no resonant absorption contribution to the absorbance in the probed spectral window.

List of publications

- M. Rebholz, T. Ding, V. Despré, L. Aufleger, M. Hartmann, K. Meyer, V. Stooß, A. Magunia, D. Wachs, P. Birk, Y. Mi, G. D. Borisova, C. da Costa Castanheira, P. Rupprecht, G. Schmid, K. Schnorr, C. D. Schröter, R. Moshammer, Z.-H. Loh, A. R. Attar, S. R. Leone, T. Gaumnitz, H. J. Wörner, S. Roling, M. Butz, H. Zacharias, S. Düsterer, R. Treusch, G. Brenner, J. Vester, A. I. Kuleff, C. Ott, and T. Pfeifer. *All-XUV pump-probe transient absorption spectroscopy of the structural molecular dynamics of diiodomethane.* submitted manuscript.

- T. Ding, C. Ott, A. Kaldun, A. Blättermann, K. Meyer, V. Stooß, M. Rebholz, P. Birk, A. Brown, H. Van der Hart, and T. Pfeifer., *Time-resolved four-wave-mixing spectroscopy for inner-valence transitions.* Opt. Lett 41:709-712, 2016.

- C. Ott, L. Aufleger, T.s Ding, M. Rebholz, A. Magunia, M. Hartmann, V. Stooß, D. Wachs, P. Birk, G. D. Borisova, K. Meyer, P. Rupprecht, C. da Costa Castanheira, R. Moshammer, A. R. Attar, T. Gaumnitz, Z. H. Loh, S. Düsterer, R. Treusch, J. Ullrich, Y. Jiang, M. Meyer, P. Lambropoulos, and T. Pfeifer., *Strong-field extreme-ultraviolet dressing of atomic double excitation.* Phys. Rev. Lett. 123:163201, 2019.

- T. Ding, M. Rebholz, L. Aufleger, M. Hartmann, K. Meyer, V. Stooß, A. Magunia, D. Wachs, P. Birk, Y. Mi, G. D. Borisova, C. da Costa Castanheira, P. Rupprecht, Z.-H. Loh, A. R. Attar, T. Gaumnitz, S. Roling, M. Butz, H. Zacharias, S. Düsterer, R. Treusch, S. M. Cavaletto, C. Ott, and T. Pfeifer. *Nonlinear Coherence Effects in Transient- Absorption Ion Spectroscopy with Stochastic Extreme-Ultraviolet Free-Electron Laser Pulses.* Phys. Rev. Lett. 123:103001, 2019.

- A. Magunia, L. Aufleger, T. Ding, P. Rupprecht, M. Rebholz, C. Ott and T. Pfeifer. *Bound-State Electron Dynamics Driven by Near-Resonantly Detuned Intense and Ultrashort Pulsed XUV Fields.* Appl. Sci. 10, 6153, 2020.

- L. Aufleger, P. Friebel, P. Rupprecht, A. Magunia, T. Ding, M. Rebholz, M. Hartmann, V. Stooß, C. Ott, and T. Pfeifer. *Pulse length effects on autoionizing states under the influence of intense SASE XUV fields.* Journal of Physics B: Atomic, Molecular and Optical Physics, accepted 18-Sep-2020.

Bibliography

[1] Joseph Fraunhofer. Bestimmung des Brechungs- und des Farbenzerstreungs-Vermögens verschiedener Glasarten, in Bezug auf die Vervollkommnung achromatischer Fernröhre. *Annalen der Physik*, 56(7):264–313, 1817.

[2] G. Kirchhoff. *Untersuchungen über das Sonnenspectum und die Spectren der chemischen Elemente, Teile 1-2*. Ferd. Dümmler's Verlagsbuchhandlung, 1866.

[3] Niels Bohr. On the constitution of atoms and molecules. *Philos. Mag.*, 26(1), 1913.

[4] A. L. Schawlow and C. H. Townes. Infrared and optical masers. *Phys. Rev.*, 112:1940–1949, 1958.

[5] T. H. Maiman. Stimulated Optical Radiation in Ruby. *Nature*, 187(4736): 493–494, 1960.

[6] A. Bauch and H. R. Telle. Frequency standards and frequency measurement. *Reports on Progress in Physics*, 65(5):789–843, 2002.

[7] Willis E. Lamb. Theory of an optical maser. *Phys. Rev.*, 134:A1429–A1450, 1964.

[8] L. E. Hargrove, R. L. Fork, and M. A. Pollack. Locking of he–ne laser modes induced by synchronous intracavity modulation. *Applied Physics Letters*, 5(1): 4–5, 1964.

[9] Ahmed H. Zewail. Femtochemistry. *The Journal of Physical Chemistry*, 97(48): 12427–12446, 1993.

[10] Ahmed H. Zewail. Femtochemistry: Atomic-scale dynamics of the chemical bond. *Journal of Physical Chemistry A*, 104:5660–5694, 2000.

[11] R. Moshammer, M. Unverzagt, W. Schmitt, J. Ullrich, and H. Schmidt-Böcking. A 4π recoil-ion electron momentum analyzer: a high-resolution "microscope" for the investigation of the dynamics of atomic, molecular and nuclear reactions. *Nuclear Instruments and Methods in Physics Research Section B: Beam Interactions with Materials and Atoms*, 108(4):425–445, 1996.

[12] J. Itatani, F. Quéré, G. L. Yudin, M. Yu. Ivanov, F. Krausz, and P. B. Corkum. Attosecond streak camera. *Phys. Rev. Lett.*, 88:173903, 2002.

[13] The history of synchrotron radiation. https://www.esrf.eu/about/synchrotron-science/history-synchrotron. [Online; accessed 25-Sep-2020].

[14] A. McPherson, G. Gibson, H. Jara, U. Johann, T. S. Luk, I. A. McIntyre, K. Boyer, and C. K. Rhodes. Studies of multiphoton production of vacuum-ultraviolet radiation in the rare gases. *J. Opt. Soc. Am. B*, 4(4):595–601, Apr 1987.

[15] X. F. Li, A. L'Huillier, M. Ferray, L. A. Lompré, and G. Mainfray. Multiple-harmonic generation in rare gases at high laser intensity. *Phys. Rev. A*, 39: 5751–5761, 1989.

[16] A. L'Huillier, K. J. Schafer, and K. C. Kulander. Theoretical aspects of intense field harmonic generation. *Journal of Physics B: Atomic, Molecular and Optical Physics*, 24(15):3315–3341, 1991.

[17] P B Corkum and Ferenc Krausz. Attosecond science. *Nature Physics*, 3(6): 381–387, 2007.

[18] Brian W. J. McNeil and Neil R. Thompson. X-ray free-electron lasers. *Nature Photonics*, 4(12):814–821, 2010.

[19] K Schnorr, A Senftleben, M Kurka, A Rudenko, G Schmid, T Pfeifer, K Meyer, M Kübel, M F Kling, Y H Jiang, R Treusch, S Düsterer, B Siemer, M Wöstmann, H Zacharias, R Mitzner, T J M Zouros, J Ullrich, C D Schröter, and R Moshammer. Electron Rearrangement Dynamics in Dissociating I_2^{n+} Molecules Accessed by Extreme Ultraviolet Pump-Probe Experiments. *Physical Review Letters*, 113: 073001, 2014.

[20] K. Schnorr, A. Senftleben, M. Kurka, A. Rudenko, L. Foucar, G. Schmid, A. Broska, T. Pfeifer, K. Meyer, D. Anielski, R. Boll, D. Rolles, M. Kübel, M. F.

Kling, Y. H. Jiang, S. Mondal, T. Tachibana, K. Ueda, T. Marchenko, M. Simon, G. Brenner, R. Treusch, S. Scheit, V. Averbukh, J. Ullrich, C. D. Schröter, and R. Moshammer. Time-resolved measurement of interatomic coulombic decay in ne_2. *Phys. Rev. Lett.*, 111:093402, 2013.

[21] W. Ackermann, G. Asova, V. Ayvazyan, A. Azima, N. Baboi, J. Bähr, V. Balandin, B. Beutner, A. Brandt, A. Bolzmann, R. Brinkmann, O. I. Brovko, M. Castellano, P. Castro, L. Catani, E. Chiadroni, S. Choroba, A. Cianchi, J. T. Costello, D. Cubaynes, J. Dardis, W. Decking, H. Delsim-Hashemi, A. Delserieys, G. Di Pirro, M. Dohlus, S. Düsterer, A. Eckhardt, H. T. Edwards, B. Faatz, J. Feldhaus, K. Flöttmann, J. Frisch, L. Fröhlich, T. Garvey, U. Gensch, Ch Gerth, M. Görler, N. Golubeva, H. J. Grabosch, M. Grecki, O. Grimm, K. Hacker, U. Hahn, J. H. Han, K. Honkavaara, T. Hott, M. Hüning, Y. Ivanisenko, E. Jaeschke, W. Jalmuzna, T. Jezynski, R. Kammering, V. Katalev, K. Kavanagh, E. T. Kennedy, S. Khodyachykh, K. Klose, V. Kocharyan, M. Körfer, M. Kollewe, W. Koprek, S. Korepanov, D. Kostin, M. Krassilnikov, G. Kube, M. Kuhlmann, C. L.S. Lewis, L. Lilje, T. Limberg, D. Lipka, F. Löhl, H. Luna, M. Luong, M. Martins, M. Meyer, P. Michelato, V. Miltchev, W. D. Möller, L. Monaco, W. F.O. Müller, O. Napieralski, O. Napoly, P. Nicolosi, D. Nölle, T. Nũez, A. Oppelt, C. Pagani, R. Paparella, N. Pchalek, J. Pedregosa-Gutierrez, B. Petersen, B. Petrosyan, G. Petrosyan, L. Petrosyan, J. Pflüger, E. Plönjes, L. Poletto, K. Pozniak, E. Prat, D. Proch, P. Pucyk, P. Radcliffe, H. Redlin, K. Rehlich, M. Richter, M. Roehrs, J. Roensch, R. Romaniuk, M. Ross, J. Rossbach, V. Rybnikov, M. Sachwitz, E. L. Saldin, W. Sandner, H. Schlarb, B. Schmidt, M. Schmitz, P. Schmüser, J. R. Schneider, E. A. Schneidmiller, S. Schnepp, S. Schreiber, M. Seidel, D. Sertore, A. V. Shabunov, C. Simon, S. Simrock, E. Sombrowski, A. A. Sorokin, P. Spanknebel, R. Spesyvtsev, L. Staykov, B. Steffen, F. Stephan, F. Stulle, H. Thom, K. Tiedtke, M. Tischer, S. Toleikis, R. Treusch, D. Trines, I. Tsakov, E. Vogel, T. Weiland, H. Weise, M. Wellhöfer, M. Wendt, I. Will, A. Winter, K. Wittenburg, W. Wurth, P. Yeates, M. V. Yurkov, I. Zagorodnov, and K. Zapfe. Operation of a free-electron laser from the extreme ultraviolet to the water window. *Nature Photonics*, 1:336–342, 2007.

[22] Robin Santra, Vladislav S Yakovlev, Thomas Pfeifer, and Zhi-heng Loh. Theory

of attosecond transient absorption spectroscopy of strong-field-generated ions. *Physical Review A*, 83, 2011.

[23] J. C. Baggesen, E. Lindroth, and L. B. Madsen. Theory of attosecond absorption spectroscopy in krypton. *Physical Review A*, 85, 2012.

[24] Mengxi Wu, Shaohao Chen, Seth Camp, Kenneth J. Schafer, and Mette B. Gaarde. Theory of strong- field attosecond transient absorption. *Journal of Physics B: Atomic, Molecular and Optical Physics*, 49, 2016.

[25] B. E. A. Saleh and M. C. Teich. *Fundamentals of Photonics*. Wiley-Interscience, second edition, 2006.

[26] Peter W. Milonni and Joseph H. Eberly. *Laser Physics*. Wiley, Hoboken, New Jersey, 2010.

[27] H. Hertz. Ueber einen Einfluss des ultravioletten Lichtes auf die electrische Entladung. *Annalen der Physik*, 267(8):983–1000, 1887.

[28] Wilhelm Hallwachs. Ueber den Einfluss des Lichtes auf electrostatisch geladene Körper. *Annalen der Physik*, 269(2):301–312, 1888.

[29] Wilhelm Hallwachs. Ueber die Electrisirung von Metallplatten durch Bestrahlung mit electrischem Licht. *Annalen der Physik*, 270(8A):731–734, 1888.

[30] P. Lenard. Erzeugung von Kathodenstrahlen durch ultraviolettes Licht. *Annalen der Physik*, 307(6):359–375, 1900.

[31] A. Einstein. Über einen die Erzeugung und Verwandlung des Lichtes betreffenden heuristischen Gesichtspunkt. *Annalen der Physik*, 322(6):132–148, 1905.

[32] Bong Hyun Boo and Norio Saito. Dissociative multiple photoionization of Br2, IBr, and I2 in the VUV and X-ray regions: A comparative study of the inner-shell processes involving Br(3d,3p,3s) and I(4d,4p,4s,3d,3p). *Journal of Electron Spectroscopy and Related Phenomena*, 127(3):139–152, 2002.

[33] Ugo Fano. Effects of Integration on Intensities and Phase Shifts. *Physical Review*, 124(6):1866–1878, 1961.

[34] P. D. Innes. On the Velocity of the Cathode Particles Emitted by Various Metals under the Influence of Röntgen Rays, and Its Bearing on the Theory of

Atomic Disintegration. *Proceedings of the Royal Society of London. Series A, Containing Papers of a Mathematical and Physical Character*, 79(532):442–462, 1907.

[35] Kai Siegbahn. Electron Spectroscopy for Atoms, Molecules, and Condensed Matter. *Science*, 217(4555):111–121, 1982.

[36] J. Ullrich, R. Moshammer, R. Dorner, O. Jagutzki, V. Mergel, H. Schmidt-Bocking, and L. Spielberger. Recoil-ion momentum spectroscopy. *J. Phys. B: At. Mol. Opt. Phys*, 30:2917–2974, 1997.

[37] F. J. Comes, U. Nielsen, and W. H. E. Schwarz. Inner electron excitation of iodine in the gaseous and solid phase. *The Journal of Chemical Physics*, 58(6): 2230–2237, 1973.

[38] G. O'Sullivan, C. McGuinness, J. T. Costello, E. T. Kennedy, and B. Weinmann. Trends in 4d-subshell photoabsorption along the iodine isonuclear sequence: I, I+ and I++. *Physical Review A - Atomic, Molecular, and Optical Physics*, 53 (5):3211–3226, 1996.

[39] J. N. Cutler, G. M. Bancroft, D. G. Sutherland, and K. H. Tan. Chemical dependence of core-level linewidths and ligand-field splittings: High-resolution core-level photoelectron spectra of I 4d levels. *Physical Review Letters*, 67(12): 1531–1534, 1991.

[40] J. N. Cutler, G. M. Bancroft, and K. H. Tan. Ligand-field splittings and core-level linewidths in I 4d photoelectron spectra of iodine molecules. *The Journal of Chemical Physics*, 97:7932–7943, 1992.

[41] D. L. Matthews, P. L. Hagelstein, M. D. Rosen, M. J. Eckart, N. M. Ceglio, A. U. Hazi, H. Medecki, B. J. MacGowan, J. E. Trebes, B. L. Whitten, E. M. Campbell, C. W. Hatcher, A. M. Hawryluk, R. L. Kauffman, L. D. Pleasance, G. Rambach, J. H. Scofield, G. Stone, and T. A. Weaver. Demonstration of a soft x-ray amplifier. *Phys. Rev. Lett.*, 54:110–113, 1985.

[42] S. Suckewer, C. H. Skinner, H. Milchberg, C. Keane, and D. Voorhees. Amplification of stimulated soft x-ray emission in a confined plasma column. *Phys. Rev. Lett.*, 55:1753–1756, Oct 1985.

[43] J. J. Rocca. Table-top soft x-ray lasers. *Review of Scientific Instruments*, 70 (10):3799–3827, 1999.

[44] Hiroyuki Daido. Review of soft x-ray laser researches and developments. *Reports on Progress in Physics*, 65(10):1513–1576, sep 2002.

[45] S. Suckewer and P. Jaeglé. X-ray laser: past, present, and future. *Laser Physics Letters*, 6(6):411–436, 2009.

[46] P. Emma, R. Akre, J. Arthur, R. Bionta, C. Bostedt, J. Bozek, A. Brachmann, P. Bucksbaum, R. Coffee, F. J. Decker, Y. Ding, D. Dowell, S. Edstrom, A. Fisher, J. Frisch, S. Gilevich, J. Hastings, G. Hays, Ph Hering, Z. Huang, R. Iverson, H. Loos, M. Messerschmidt, A. Miahnahri, S. Moeller, H. D. Nuhn, G. Pile, D. Ratner, J. Rzepiela, D. Schultz, T. Smith, P. Stefan, H. Tompkins, J. Turner, J. Welch, W. White, J. Wu, G. Yocky, and J. Galayda. First lasing and operation of an ångstrom-wavelength free-electron laser. *Nature Photonics*, 4(9):641–647, 2010.

[47] Nina Rohringer, Duncan Ryan, Richard A London, Michael Purvis, Felicie Albert, James Dunn, John D Bozek, Christoph Bostedt, Alexander Graf, Randal Hill, Stefan P Hau-Riege, and Jorge J Rocca. Atomic inner-shell X-ray laser at 1.46 nanometres pumped by an X-ray free-electron laser. *Nature*, 481(7382): 488–491, 2012.

[48] Peter Schmüser, Martin Dohlhus, and Jörg Rossbach. *Ultraviolet and Soft X-Ray Free-Electron Lasers*. Springer, 2008.

[49] A.M. Kondratenko and E.L. Saldin. Generation of coherent radiation by a relativistic electron beam in an ondulator. *Part. Acc.*, 10:207–216, 1980.

[50] V. Ayvazyan, N. Baboi, I. Bohnet, R. Brinkmann, M. Castellano, P. Castro, L. Catani, S. Choroba, A. Cianchi, M. Dohlus, H. T. Edwards, B. Faatz, A. A. Fateev, J. Feldhaus, K. Flöttmann, A. Gamp, T. Garvey, H. Genz, Ch Gerth, V. Gretchko, B. Grigoryan, U. Hahn, C. Hessler, K. Honkavaara, M. Hüning, R. Ischebeck, M. Jablonka, T. Kamps, M. Körfer, M. Krassilnikov, J. Krzywinski, M. Liepe, A. Liero, T. Limberg, H. Loos, M. Luong, C. Magne, J. Menzel, P. Michelato, M. Minty, U. C. Müller, D. Nölle, A. Novokhatski, C. Pagani, F. Peters, J. Pflüger, P. Piot, L. Plucinski, K. Rehlich, I. Reyzl, A. Richter, J. Rossbach, E. L. Saldin, W. Sandner, H. Schlarb, G. Schmidt, P. Schmüser,

J. R. Schneider, E. A. Schneidmiller, H. J. Schreiber, S. Schreiber, D. Sertore, S. Setzer, S. Simrock, R. Sobierajski, B. Sonntag, B. Steeg, F. Stephan, K. P. Sytchev, K. Tiedtke, M. Tonutti, R. Treusch, D. Trines, D. Türke, V. Verzilov, R. Wanzenberg, T. Weiland, H. Weise, M. Wendt, I. Will, S. Wolff, K. Wittenburg, M. V. Yurkov, and K. Zapfe. Generation of GW Radiation Pulses from a VUV Free-Electron Laser Operating in the Femtosecond Regime. *Physical Review Letters*, 88(10):4, 2002.

[51] E. Allaria, R. Appio, L. Badano, W. A. Barletta, S. Bassanese, S. G. Biedron, A. Borga, E. Busetto, D. Castronovo, P. Cinquegrana, S. Cleva, D. Cocco, M. Cornacchia, P. Craievich, I. Cudin, G. D'Auria, M. Dal Forno, M. B. Danailov, R. De Monte, G. De Ninno, P. Delgiusto, A. Demidovich, S. Di Mitri, B. Diviacco, A. Fabris, R. Fabris, W. Fawley, M. Ferianis, E. Ferrari, S. Ferry, L. Froehlich, P. Furlan, G. Gaio, F. Gelmetti, L. Giannessi, M. Giannini, R. Gobessi, R. Ivanov, E. Karantzoulis, M. Lonza, A. Lutman, B. Mahieu, M. Milloch, S. V. Milton, M. Musardo, I. Nikolov, S. Noe, F. Parmigiani, G. Penco, M. Petronio, L. Pivetta, M. Predonzani, F. Rossi, L. Rumiz, A. Salom, C. Scafuri, C. Serpico, P. Sigalotti, S. Spampinati, C. Spezzani, M. Svandrlik, C. Svetina, S. Tazzari, M. Trovo, R. Umer, A. Vascotto, M. Veronese, R. Visintini, M. Zaccaria, D. Zangrando, and M. Zangrando. Highly coherent and stable pulses from the FERMI seeded free-electron laser in the extreme ultraviolet. *Nature Photonics*, 6:699–704, 2012.

[52] Tadashi Togashi, Eiji J. Takahashi, Katsumi Midorikawa, Makoto Aoyama, Koichi Yamakawa, Takahiro Sato, Atsushi Iwasaki, Shigeki Owada, Tomoya Okino, Kaoru Yamanouchi, Fumihiko Kannari, Akira Yagishita, Hidetoshi Nakano, Marie E. Couprie, Kenji Fukami, Takaki Hatsui, Toru Hara, Takashi Kameshima, Hideo Kitamura, Noritaka Kumagai, Shinichi Matsubara, Mitsuru Nagasono, Haruhiko Ohashi, Takashi Ohshima, Yuji Otake, Tsumoru Shintake, Kenji Tamasaku, Hitoshi Tanaka, Takashi Tanaka, Kazuaki Togawa, Hiromitsu Tomizawa, Takahiro Watanabe, Makina Yabashi, and Tetsuya Ishikawa. Extreme ultraviolet free electron laser seeded with high-order harmonic of ti:sapphire laser. *Opt. Express*, 19(1):317–324, 2011.

[53] J. Amann, W. Berg, V. Blank, F. J. Decker, Y. Ding, P. Emma, Y. Feng, J. Frisch, D. Fritz, J. Hastings, Z. Huang, J. Krzywinski, R. Lindberg, H. Loos, A. Lutman, H. D. Nuhn, D. Ratner, J. Rzepiela, D. Shu, Yu Shvyd'Ko, S. Spampinati, S. Stoupin, S. Terentyev, E. Trakhtenberg, D. Walz, J. Welch, J. Wu, A. Zholents,

and D. Zhu. Demonstration of self-seeding in a hard-X-ray free-electron laser. *Nature Photonics*, 6:693–698, 2012.

[54] FLASH schematics. https://flash.desy.de, . [Online; accessed 16-Jul-2020].

[55] S. Schreiber, C. Grün, K. Klose, J. Rönsch-Schulenburg, and B. Steffen. FLASH Photoinjector Laser Systems. In *Proc. FEL'19*, number 39 in Free Electron Laser Conference, pages 430–433. JACoW Publishing, Geneva, Switzerland, nov 2019. ISBN 978-3-95450-210-3. doi: 10.18429/JACoW-FEL2019-WEP048. URL http://jacow.org/fel2019/papers/wep048.pdf. https://doi.org/10.18429/JACoW-FEL2019-WEP048.

[56] B Faatz, E Plönjes, S Ackermann, A Agababyan, V Asgekar, V Ayvazyan, S Baark, N Baboi, V Balandin, N von Bargen, Y Bican, O Bilani, J Bödewadt, M Böhnert, R Böspflug, S Bonfigt, H Bolz, F Borges, O Borkenhagen, M Brachmanski, M Braune, A Brinkmann, O Brovko, T Bruns, P Castro, J Chen, M K Czwalinna, H Damker, W Decking, M Degenhardt, A Delfs, T Delfs, H Deng, M Dressel, H-T Duhme, S Düsterer, H Eckoldt, A Eislage, M Felber, J Feldhaus, P Gessler, M Gibau, N Golubeva, T Golz, J Gonschior, A Grebentsov, M Grecki, C Grün, S Grunewald, K Hacker, L Hänisch, A Hage, T Hans, E Hass, A Hauberg, O Hensler, M Hesse, K Heuck, A Hidvegi, M Holz, K Honkavaara, H Höppner, A Ignatenko, J Jäger, U Jastrow, R Kammering, S Karstensen, A Kaukher, H Kay, B Keil, K Klose, V Kocharyan, M Köpke, M Körfer, W Kook, B Krause, O Krebs, S Kreis, F Krivan, J Kuhlmann, M Kuhlmann, G Kube, T Laarmann, C Lechner, S Lederer, A Leuschner, D Liebertz, J Liebing, A Liedtke, L Lilje, T Limberg, D Lipka, B Liu, B Lorbeer, K Ludwig, H Mahn, G Marinkovic, C Martens, F Marutzky, M Maslocv, D Meissner, N Mildner, V Miltchev, S Molnar, D Mross, F Müller, R Neumann, P Neumann, D Nölle, F Obier, M Pelzer, H-B Peters, K Petersen, A Petrosyan, G Petrosyan, L Petrosyan, V Petrosyan, A Petrov, S Pfeiffer, A Piotrowski, Z Pisarov, T Plath, P Pototzki, M J Prandolini, J Prenting, G Priebe, B Racky, T Ramm, K Rehlich, R Riedel, M Roggli, M Röhling, J Rönsch-Schulenburg, J Rossbach, V Rybnikov, J Schäfer, J Schaffran, H Schlarb, G Schlesselmann, M Schlösser, P Schmid, C Schmidt, F Schmidt-Föhre, M Schmitz, E Schneidmiller, A Schöps, M Scholz, S Schreiber, K Schütt, U Schütz, H Schulte-Schrepping, M Schulz, A Shabunov, P Smirnov, E Sombrowski, A Sorokin, B Sparr, J Spengler, M Staack, M Stadler, C Stechmann, B Steffen, N Stojanovic, V Sychev, E Syresin, T Tanikawa, F Tavella,

N Tesch, K Tiedtke, M Tischer, R Treusch, S Tripathi, P Vagin, P Vetrov, S Vilcins, M Vogt, A de Zubiaurre Wagner, T Wamsat, H Weddig, G Weichert, H Weigelt, N Wentowski, C Wiebers, T Wilksen, A Willner, K Wittenburg, T Wohlenberg, J Wortmann, W Wurth, M Yurkov, I Zagorodnov, and J Zemella. Simultaneous operation of two soft x-ray free-electron lasers driven by one linear accelerator. *New Journal of Physics*, 18(6):062002, 2016.

[57] FLASH1 parameters. https://photon-science.desy.de/facilities/flash/flash_parameters/index_eng.html, . [Online; accessed 21-Jul-2020].

[58] K. Tiedtke, A. Azima, N. Von Bargen, L. Bittner, S. Bonfigt, S. Düsterer, B. Faatz, U. Frühling, M. Gensch, Ch Gerth, N. Guerassimova, U. Hahn, T. Hans, M. Hesse, K. Honkavaar, U. Jastrow, P. Juranic, S. Kapitzki, B. Keitel, T. Kracht, M. Kuhlmann, W. B. Li, M. Martins, T. Núñez, E. Plönjes, H. Redlin, E. L. Saldin, E. A. Schneidmiller, J. R. Schneider, S. Schreiber, N. Stojanovic, F. Tavella, S. Toleikis, R. Treusch, H. Weigelt, M. Wellhöfer, H. Wabnitz, M. V. Yurkov, and J. Feldhaus. The soft x-ray free-electron laser FLASH at DESY: Beamlines, diagnostics and end-stations. *New Journal of Physics*, 11:023029, 2009.

[59] K. Tiedtke, J. Feldhaus, U. Hahn, U. Jastrow, T. Nunez, T. Tschentscher, S. V. Bobashev, A. A. Sorokin, J. B. Hastings, S. Möller, L. Cibik, A. Gottwald, A. Hoehl, U. Kroth, M. Krumrey, H. Schöppe, G. Ulm, and M. Richter. Gas detectors for x-ray lasers. *Journal of Applied Physics*, 103(094511), 2008.

[60] G. Brenner, S. Kapitzki, M. Kuhlmann, E. Ploenjes, T. Noll, F. Siewert, R. Treusch, K. Tiedtke, R. Reininger, M. D. Roper, M. A. Bowler, F. M. Quinn, and J. Feldhaus. First results from the online variable line spacing grating spectrometer at FLASH. *Nuclear Instruments and Methods in Physics Research A*, 635:S99–S103, 2011.

[61] M. Wöstmann, R. Mitzner, T. Noll, S. Roling, B. Siemer, F. Siewert, S. Eppenhoff, F. Wahlert, and H. Zacharias. The XUV split-and-delay unit at beamline BL2 at FLASH. *Journal of Physics B: Atomic, Molecular and Optical Physics*, 46:164005, 2013.

[62] Thomas Ding, Marc Rebholz, Lennart Aufleger, Maximilian Hartmann, Kristina Meyer, Veit Stooß, Alexander Magunia, David Wachs, Paul Birk, Yonghao Mi,

Gergana Dimitrova Borisova, Carina da Costa Castanheira, Patrick Rupprecht, Zhi-Heng Loh, Andrew R. Attar, Thomas Gaumnitz, Sebastian Roling, Marco Butz, Helmut Zacharias, Stefan Düsterer, Rolf Treusch, Stefano M. Cavaletto, Christian Ott, and Thomas Pfeifer. Nonlinear Coherence Effects in Transient-Absorption Ion Spectroscopy with Stochastic Extreme-Ultraviolet Free-Electron Laser Pulses. *Physical Review Letters*, 123:103001, 2019.

[63] Hitachi Aberration-Corrected Concave Gratings for Flat-Field Spectrographs, 001-0640. https://www.hitachi-hightech.com/products/images/9797/ana-grating_05.pdf. [Online; accessed 02-Sep-2020].

[64] Princeton Instruments PIXIS-XO: 400B. https://www.princetoninstruments.com/wp-content/uploads/2020/04/PIXIS-XO_400B_datasheet.pdf. [Online; accessed 04-Sep-2020].

[65] C. Ott. *Attosecond multidimensional interferometry of single and two correlated electrons in atoms.* Ph.d. thesis, Universität Heidelberg, 2012.

[66] Smaract SMS-20-20-S-HV. https://www.smaract.com/pdf-details/sms-20-20. [Online; accessed 04-Sep-2020].

[67] Mirror reflectivity. https://henke.lbl.gov/optical_constants/mirror2.html. [Online; accessed 04-Sep-2020].

[68] Piezo-controlled tip/tilt stage, Physikinstrumente S-325. https://www.physikinstrumente.de/de/produkte/piezo-nanopositioniertische/piezokippspiegel/s-325-piezo-hub-und-kipp-plattform-300650/#specification. [Online; accessed 15-Sep-2020].

[69] Piezo-controlled delay stage, Physikinstrumente Hera P-622. https://static.physikinstrumente.com/fileadmin/user_upload/physik_instrumente/files/datasheets/P-62x.Z-Datasheet.pdf. [Online; accessed 15-Sep-2020].

[70] Carina da Costa Castanheira. *Towards multidimensional spectroscopy experiments in the XUV.* Master thesis, Universität Heidelberg, 2018.

[71] L. Aufleger. *Measurement of electron dynamics in atoms and molecules with intense XUV FEL radiation.* Master thesis, Universität Heidelberg, 2016.

[72] Peter Hamm and Martin Zanni. *Concepts and Methods of 2D Infrared Spectroscopy*. Cambridge University Press, 2011.

[73] Hexapod 6-axis manipulator, Physikinstrumente H-811. https://www.physikinstrumente.de/de/produkte/hexapoden-parallelkinematiken/h-811i2-6-achsen-miniatur-hexapod-700886/. [Online; accessed 15-Sep-2020].

[74] R. Moshammer, Th. Pfeifer, A. Rudenko, Y. H. Jiang, L. Foucar, M. Kurka, K. U. Kühnel, C. D. Schröter, J. Ullrich, O. Herrwerth, M. F. Kling, X.-J. Liu, K. Motomura, H. Fukuzawa, A. Yamada, K. Ueda, K. L. Ishikawa, K. Nagaya, H. Iwayama, A. Sugishima, Y. Mizoguchi, S. Yase, M. Yao, N. Saito, A. Belkacem, M. Nagasono, A. Higashiya, M. Yabashi, T. Ishikawa, H. Ohashi, H. Kimura, and T. Togashi. Second-order autocorrelation of XUV FEL pulses via time resolved two-photon single ionization of He. *Optics Express*, 19(22): 21698–21706, 2011.

[75] A. A. Sorokin, A. Gottwald, A. Hoehl, U. Kroth, H. Schöppe, G. Ulm, M. Richter, S. V. Bobashev, I. V. Domracheva, D. N. Smirnov, K. Tiedtke, S. Düsterer, J. Feldhaus, U. Hahn, U. Jastrow, M. Kuhlmann, T. Nunez, E. Plönjes, and R. Treusch. Method based on atomic photoionization for spot-size measurement on focused soft x-ray free-electron laser beams. *Applied Physics Letters*, 89 (221114):1–4, 2006.

[76] M. Richter, A. Gottwald, U. Kroth, A. A. Sorokin, S. V. Bobashev, L. A. Shmaenok, J. Feldhaus, Ch Gerth, B. Steeg, K. Tiedtke, and R. Treusch. Measurement of gigawatt radiation pulses from a vacuum and extreme ultraviolet free-electron laser. *Applied Physics Letters*, 83(14):2970–2972, 2003.

[77] R. Akre, L. Bentson, P. Emma, and P. Krejcik. A transverse RF deflecting structure for bunch length and phase space diagnostics. *Proceedings of the IEEE Particle Accelerator Conference*, 3(June):2353–2355, 2001.

[78] Michael Röhrs, Christopher Gerth, Markus Hüning, and Holger Schlarb. Slice emittance measurements at FLASH. *EPAC 2006 - Contributions to the Proceedings*, pages 77–79, 2006.

[79] Arvid Eislage. personal communication.

[80] D. Wachs. *Kalibrationen von XUV-Spektren für Absorptionsmessungen am FLASH.* Bachelor thesis, Universität Heidelberg, 2016.

[81] Christian Ott, Lennart Aufleger, Thomas Ding, Marc Rebholz, Alexander Magunia, Maximilian Hartmann, Veit Stooß, David Wachs, Paul Birk, Gergana D. Borisova, Kristina Meyer, Patrick Rupprecht, Carina da Costa Castanheira, Robert Moshammer, Andrew R. Attar, Thomas Gaumnitz, Zhi-Heng Loh, Stefan Düsterer, Rolf Treusch, Joachim Ullrich, Yuhai Jiang, Michael Meyer, Peter Lambropoulos, and Thomas Pfeifer. Strong-field extreme-ultraviolet dressing of atomic double excitation. *Phys. Rev. Lett.*, 123:163201, 2019.

[82] L. Aufleger, P. Friebel, P. Rupprecht, A. Magunia, T. Ding, M. Rebholz, M. Hartmann, V. Stooß, C. Ott, and T. Pfeifer. Pulse length effects on autoionizing states under the influence of intense SASE XUV fields. *Journal of Physics B: Atomic, Molecular and Optical Physics*, accepted 18-Sep-2020.

[83] Thomas Ding. *Quantum dynamics in weak and strong fields measured by XUV nonlinear spectroscopy.* Ph.d. thesis, Universität Heidelberg, 2018.

[84] Zhengrong Wei, Jialin Li, Lin Wang, Soo Teck See, Mark Hyunpong Jhon, Yingfeng Zhang, Fan Shi, Minghui Yang, and Zhi-Heng Loh. Elucidating the origins of multimode vibrational coherences of polyatomic molecules induced by intense laser fields. *Nature Communications*, 8:735, 2017.

[85] Mark J. Rosker, Marcos Dantus, and Ahmed H. Zewail. Femtosecond real-time probing of reactions. I. The technique. *The Journal of Chemical Physics*, 89 (10):6113–6127, 1988.

[86] Arne Baumann, Dimitrios Rompotis, Oliver Schepp, Marek Wieland, and Markus Drescher. Time-Resolved Dissociation Dynamics of Iodomethane Resulting from Rydberg and Valence Excitation. *Journal of Physical Chemistry A*, 122:4779–4784, 2018.

[87] Andrew R. Attar, Aditi Bhattacherjee, and Stephen R. Leone. Direct Observation of the Transition-State Region in the Photodissociation of CH_3I by Femtosecond Extreme Ultraviolet Transient Absorption Spectroscopy. *Journal of Physical Chemistry Letters*, 6:5072–5077, 2015.

[88] L. Drescher, M. C.E. Galbraith, G. Reitsma, J. Dura, N. Zhavoronkov, S. Patchkovskii, M. J.J. Vrakking, and J. Mikosch. Communication: XUV transient absorption spectroscopy of iodomethane and iodobenzene photodissociation. *The Journal of Chemical Physics*, 145:011101, 2016.

[89] M.C.E. Galbraith, S. Scheit, N.V. Golubev, G. Reitsma, N. Zhavoronkov, V. Despré, F. Lépine, A.I. Kuleff, M.J.J. Vrakking, O. Kornilov, H. Köppel, and J. Mikosch. Few-femtosecond passage of conical intersections in the benzene cation. *Nature Communications*, 8(1):1–6, 2017.

[90] Yoann Pertot, Cédric Schmidt, Mary Matthews, Adrien Chauvet, Martin Huppert, Vit Svoboda, Aaron Von Conta, Andres Tehlar, Denitsa Baykusheva, Jean Pierre Wolf, and Hans Jakob Wörner. Time-resolved x-ray absorption spectroscopy with a water-window high-harmonic source. *Science*, 355(6322): 264–267, 2017.

[91] L. Drescher, G. Reitsma, T. Witting, S. Patchkovskii, J. Mikosch, and M. J.J. Vrakking. State-Resolved Probing of Attosecond Timescale Molecular Dipoles. *The Journal of Physical Chemistry Letters*, 10:265–269, 2019.

[92] Yuki Kobayashi, Kristina F. Chang, Tao Zeng, Daniel M. Neumark, and Stephen R. Leone. Direct mapping of curve-crossing dynamics in IBr by attosecond transient absorption spectroscopy. *Science*, 365(6448):79–83, 2019.

[93] Benjamin Erk, Rebecca Boll, Sebastian Trippel, Denis Anielski, Lutz Foucar, Benedikt Rudek, Sascha W Epp, Ryan Coffee, Sebastian Carron, Sebastian Schorb, Ken R Ferguson, Michele Swiggers, John D Bozek, Marc Simon, Tatiana Marchenko, Jochen Küpper, and Ilme Schlichting. Imaging charge transfer in iodomethane upon x-ray photoabsorption. *Science*, 345(6194):288–291, 2014.

[94] Rebecca Boll, Benjamin Erk, Ryan Coffee, Sebastian Trippel, Thomas Kierspel, Cédric Bomme, John D. Bozek, Mitchell Burkett, Sebastian Carron, Ken R. Ferguson, Lutz Foucar, Jochen Küpper, Tatiana Marchenko, Catalin Miron, Minna Patanen, Timur Osipov, Sebastian Schorb, Marc Simon, Michelle Swiggers, Simone Techert, Kiyoshi Ueda, Christoph Bostedt, Daniel Rolles, and Artem Rudenko. Charge transfer in dissociating iodomethane and fluoromethane molecules ionized by intense femtosecond X-ray pulses. *Structural Dynamics*, 3: 043207, 2016.

[95] M. Hollstein, K. Mertens, S. Klumpp, N. Gerken, S. Palutke, I. Baev, G. Brenner, S. Dziarzhytski, M. Meyer, W. Wurth, D. Pfannkuche, and M. Martins. Ultrafast charge redistribution in small iodine containing molecules. *New Journal of Physics*, 21:33017, 2019.

[96] Koji Motomura, Edwin Kukk, Hironobu Fukuzawa, Shin Ichi Wada, Kiyonobu Nagaya, Satoshi Ohmura, Subhendu Mondal, Tetsuya Tachibana, Yuta Ito, Ryosuke Koga, Tsukasa Sakai, Kenji Matsunami, Artem Rudenko, Christophe Nicolas, Xiao Jing Liu, Catalin Miron, Yizhu Zhang, Yuhai Jiang, Jianhui Chen, Mailam Anand, Dong Eon Kim, Kensuke Tono, Makina Yabashi, Makoto Yao, and Kiyoshi Ueda. Charge and Nuclear Dynamics Induced by Deep Inner-Shell Multiphoton Ionization of CH_3I Molecules by Intense X-ray Free-Electron Laser Pulses. *The Journal of Physical Chemistry Letters*, 6(15):2944–2949, 2015.

[97] Hironobu Fukuzawa, Tsukasa Takanashi, Edwin Kukk, Koji Motomura, Shin ichi Wada, Kiyonobu Nagaya, Yuta Ito, Toshiyuki Nishiyama, Christophe Nicolas, Yoshiaki Kumagai, Denys Iablonskyi, Subhendu Mondal, Tetsuya Tachibana, Daehyun You, Syuhei Yamada, Yuta Sakakibara, Kazuki Asa, Yuhiro Sato, Tsukasa Sakai, Kenji Matsunami, Takayuki Umemoto, Kango Kariyazono, Shinji Kajimoto, Hikaru Sotome, Per Johnsson, Markus S. Schöffler, Gregor Kastirke, Kuno Kooser, Xiao Jing Liu, Theodor Asavei, Liviu Neagu, Serguei Molodtsov, Kohei Ochiai, Manabu Kanno, Kaoru Yamazaki, Shigeki Owada, Kanade Ogawa, Tetsuo Katayama, Tadashi Togashi, Kensuke Tono, Makina Yabashi, Aryya Ghosh, Kirill Gokhberg, Lorenz S. Cederbaum, Alexander I. Kuleff, Hiroshi Fukumura, Naoki Kishimoto, Artem Rudenko, Catalin Miron, Hirohiko Kono, and Kiyoshi Ueda. Real-time observation of X-ray-induced intramolecular and interatomic electronic decay in CH_2I_2. *Nature Communications*, 10:2186, 2019.

[98] Y. H. Jiang, A. Rudenko, O. Herrwerth, L. Foucar, M. Kurka, K. U. Kühnel, M. Lezius, M. F. Kling, J. Van Tilborg, A. Belkacem, K. Ueda, S. Düsterer, R. Treusch, C. D. Schröter, R. Moshammer, and J. Ullrich. Ultrafast Extreme Ultraviolet Induced Isomerization of Acetylene Cations. *Physical Review Letters*, 105:263002, 2010.

[99] Artem Rudenko and Daniel Rolles. Time-resolved studies with FELs. *Journal of Electron Spectroscopy and Related Phenomena*, 204:228–236, 2015.

[100] A. Picón, C. S. Lehmann, C. Bostedt, A. Rudenko, A. Marinelli, T. Osipov,

D. Rolles, N. Berrah, C. Bomme, M. Bucher, G. Doumy, B. Erk, K. R. Ferguson, T. Gorkhover, P. J. Ho, E. P. Kanter, B. Krässig, J. Krzywinski, A. A. Lutman, A. M. March, D. Moonshiram, D. Ray, L. Young, S. T. Pratt, and S. H. Southworth. Hetero-site-specific X-ray pump-probe spectroscopy for femtosecond intramolecular dynamics. *Nature Communications*, 7(May):5–10, 2016.

[101] Alfonso Saiz-Lopez, John M. C. Plane, Alex R. Baker, Lucy J. Carpenter, Roland von Glasow, Juan C. Gómez Martín, Gordon McFiggans, and Russell W. Saunders. Atmospheric Chemistry of Iodine. *Chemical Reviews*, 9781118466: 591–601, 2014.

[102] Colin D. O'Dowd, Jose L. Jimenez, Roya Bahreini, Richard C. Flagan, John H. Seinfeld, Kaarle Hämerl, Lilsa Pirjola, Markku Kulmala, S. Gerard Jennings, and Thorsten Hoffmann. Marine aerosol formation from biogenic iodine emissions. *Nature*, 417:632–636, 2002.

[103] S. Tegtmeier, K. Krüger, B. Quack, E. L. Atlas, I. Pisso, A. Stohl, and X. Yang. Emission and transport of bromocarbons: From the West Pacific ocean into the stratosphere. *Atmospheric Chemistry and Physics*, 12:10633–10648, 2012.

[104] C. E. Jones, K. E. Hornsby, R. M. Dunk, R. J. Leigh, and L. J. Carpenter. Coastal measurements of short-lived reactive iodocarbons and bromocarbons at Roscoff, Brittany during the RHaMBLe campaign. *Atmospheric Chemistry and Physics*, 9:8757–8769, 2009.

[105] F. Ziska, B. Quack, K. Abrahamsson, S. D. Archer, E. Atlas, T. Bell, J. H. Butler, L. J. Carpenter, C. E. Jones, N. R.P. Harris, H. Hepach, K. G. Heumann, C. Hughes, J. Kuss, K. Krüger, P. Liss, R. M. Moore, A. Orlikowska, S. Raimund, C. E. Reeves, W. Reifenhäuser, A. D. Robinson, C. Schall, T. Tanhua, S. Tegtmeier, S. Turner, L. Wang, D. Wallace, J. Williams, H. Yamamoto, S. Yvon-Lewis, and Y. Yokouchi. Global sea-to-air flux climatology for bromoform, dibromomethane and methyl iodide. *Atmospheric Chemistry and Physics*, 13: 8915–8934, 2013.

[106] James W. Fitzgerald. Marine aerosols: A review. *Atmospheric Environment Part A, General Topics*, 25(3-4):533–545, 1991.

[107] Hélène Pellissier. Recent developments in asymmetric cyclopropanation. *Tetrahedron*, 64(30):7041 – 7095, 2008.

[108] L. Nahon, P. Morin, and F. Combet-Farnoux. Relaxation of the nd → (n + 1)p resonances in atomic bromine and iodine. *Physica Scripta*, 1992(T41):104–112, 1992.

[109] D. M.P. Holland, I. Powis, G. Öhrwall, L. Karlsson, and W. von Niessen. A study of the photoionisation dynamics of chloromethane and iodomethane. *Chemical Physics*, 326:535–550, 2006.

[110] Terry N Olney, Glyn Cooper, and C E Brion. Quantitative studies of the photoabsorption (4 . 5 – 488 eV) and photoionization (9 – 59 . 5 eV) of methyl iodide using dipole electron impact techniques. *Chemical Physics*, pages 211–237, 1998.

[111] Veniamin A. Borin, Sergey M. Matveev, Darya S. Budkina, Patrick Z. El-Khoury, and Alexander N. Tarnovsky. Direct photoisomerization of CH2I2 vs. CHBr3 in the gas phase: a joint 50 fs experimental and multireference resonance-theoretical study. *Physical Chemistry Chemical Physics*, 18:28883–28892, 2016.

[112] Antonella Cartoni, Anna Rita Casavola, Paola Bolognesi, Stefano Borocci, and Lorenzo Avaldi. VUV photofragmentation of CH2I2: The [CH2/I-I]•+ isodiiodomethane intermediate in the I-loss channel from [CH2I2]•+. *The Journal of Physical Chemistry A*, 119:3704–3709, 2015.

[113] Physical and chemical properties of diiodomethane. http://surface-tension.de/LIQUIDS/Diiodomethane3.htm. [Online; accessed 15-Sep-2020].

[114] L. Nahon, L. Duffy, P. Morin, F. Combet-Farnoux, J. Tremblay, and M. Larzilliere. Relaxation of the 4d5p resonance in atomic iodine. *Physical Review A*, 41 (9):4879–4888, 1990.

[115] J. Schirmer, A. B. Trofimov, and G. Stelter. A non-Dyson third-order approximation scheme for the electron propagator. *The Journal of Chemical Physics*, 109(12):4734–4744, 1998.

[116] V Despré, A Marciniak, V Loriot, M C E Galbraith, A Rouzée, M J J Vrakking, F Lépine, and A I Kuleff. Attosecond Hole Migration in Benzene Molecules Surviving Nuclear Motion. *The Journal of Physical Chemistry Letters*, 6(3): 426–431, 2015.

[117] Elisa Appi, Christina C Papadopoulou, Jose Louise Mapa, Nishad Wesavkar, Christoph Jusko, Philip Mosel, Skirmantas Ališauskas, Tino Lang, Christoph M Heyl, Bastian Manschwetus, Maciej Brachmanski, Markus Braune, Hannes Lindenblatt, Florian Trost, Severin Meister, Patrizia Schoch, Rolf Treusch, Robert Moshammer, Ingmar Hartl, Uwe Morgner, and Milutin Kovacev. A synchronized VUV light source based on high-order harmonic generation at FLASH. *Scientific Reports*, 10(1):6867, 2020.

[118] A. A. Lutman, R. Coffee, Y. Ding, Z. Huang, J. Krzywinski, T. Maxwell, M. Messerschmidt, and H.-D. Nuhn. Experimental Demonstration of Femtosecond Two-Color X-Ray Free-Electron Lasers. *Physical Review Letters*, 110: 134801, 2013.

[119] E. Schneidmiller et al. Two-Color Operation of FLASH2 Undulator. In *Proc. FEL'19*, number 39 in Free Electron Laser Conference, pages 168–171. JACoW Publishing, Geneva, Switzerland, nov 2019. ISBN 978-3-95450-210-3. doi: doi:10.18429/JACoW-FEL2019-TUP055. URL http://jacow.org/fel2019/papers/tup055.pdf. https://doi.org/10.18429/JACoW-FEL2019-TUP055.

[120] Zhengrong Wei, Jialin Li, Huimin Zhang, Yunpeng Lu, Minghui Yang, and Zhi-Heng Loh. Ultrafast dissociative ionization and large-Amplitude vibrational wave packet dynamics of strong-field-ionized di-iodomethane. *The Journal of Chemical Physics*, 151:214308, 2019.

[121] Gerald Schubert. Earth. In Arthur N. Cox, editor, *Allen's Astrophysical Quantities*, chapter 9. Springer, New-York, 2002.

[122] R. L. Rudnick and S. Gao. Composition of the continental crust. In H. D. Holland and K. K. Turekian, editors, *In The Crust*, chapter 3. Elsevier-Pergamon, Oxford, 2003.

[123] Hilton M Weiss. Appreciating Oxygen. *Journal of Chemical Education*, 85(9): 1218, 2008.

[124] Klaus Schmidt-Rohr. Oxygen is the high-energy molecule powering complex multicellular life: Fundamental corrections to traditional bioenergetics. *ACS Omega*, 5(5):2221–2233, 2020.

[125] B. Feuerstein, Th. Ergler, A. Rudenko, K. Zrost, C. D. Schröter, R. Moshammer, J. Ullrich, T. Niederhausen, and U. Thumm. Complete characterization of molecular dynamics in ultrashort laser fields. *Phys. Rev. Lett.*, 99:153002, 2007.

[126] Uwe Thumm, Thomas Niederhausen, and Bernold Feuerstein. Time-series analysis of vibrational nuclear wave-packet dynamics in $D_2{}^+$. *Phys. Rev. A*, 77: 063401, Jun 2008.

[127] I. A. Bocharova, A. S. Alnaser, U. Thumm, T. Niederhausen, D. Ray, C. L. Cocke, and I. V. Litvinyuk. Time-resolved coulomb-explosion imaging of nuclear wave-packet dynamics induced in diatomic molecules by intense few-cycle laser pulses. *Phys. Rev. A*, 83:013417, 2011.

[128] S. De, M. Magrakvelidze, I. A. Bocharova, D. Ray, W. Cao, I. Znakovskaya, H. Li, Z. Wang, G. Laurent, U. Thumm, M. F. Kling, I. V. Litvinyuk, I. Ben-Itzhak, and C. L. Cocke. Following dynamic nuclear wave packets in n_2, o_2, and co with few-cycle infrared pulses. *Phys. Rev. A*, 84:043410, 2011.

[129] Th. Ergler, A. Rudenko, B. Feuerstein, K. Zrost, C. D. Schröter, R. Moshammer, and J. Ullrich. Time-resolved imaging and manipulation of h_2 fragmentation in intense laser fields. *Phys. Rev. Lett.*, 95:093001, 2005.

[130] S. De, I. A. Bocharova, M. Magrakvelidze, D. Ray, W. Cao, B. Bergues, U. Thumm, M. F. Kling, I. V. Litvinyuk, and C. L. Cocke. Tracking nuclear wave-packet dynamics in molecular oxygen ions with few-cycle infrared laser pulses. *Phys. Rev. A*, 82:013408, 2010.

[131] A Rudenko, Y H Jiang, M Kurka, K U Kühnel, L Foucar, O Herrwerth, M Lezius, M F Kling, C D Schröter, R Moshammer, and J Ullrich. Exploring few-photon, few-electron reactions at FLASH: from ion yield and momentum measurements to time-resolved and kinematically complete experiments. *Journal of Physics B: Atomic, Molecular and Optical Physics*, 43(19):194004, 2010.

[132] M. Magrakvelidze, O. Herrwerth, Y. H. Jiang, A. Rudenko, M. Kurka, L. Foucar, K. U. Kühnel, M. Kübel, Nora G. Johnson, C. D. Schröter, S. Düsterer, R. Treusch, M. Lezius, I. Ben-Itzhak, R. Moshammer, J. Ullrich, M. F. Kling, and U. Thumm. Tracing nuclear-wave-packet dynamics in singly and doubly charged states of N 2 and O 2 with XUV-pump-XUV-probe experiments. *Physical Review A - Atomic, Molecular, and Optical Physics*, 86(1):1–11, 2012.

[133] R. L. Kelly, editor. *Atomic and Ionic Emission Lines below 2000 Angstroms*. U.S. Govt. Printing Office, Washington D.C., 1973.

[134] Chengyin Wu, Yudong Yang, Zhifeng Wu, Bozhen Chen, Hua Dong, Xianrong Liu, Yongkai Deng, Hong Liu, Yunquan Liu, and Qihuang Gong. Coulomb explosion of nitrogen and oxygen molecules through non-coulombic states. *Phys. Chem. Chem. Phys.*, 13:18398–18408, 2011.

Erklärung:

Ich versichere, dass ich diese Arbeit selbstständig verfasst, und keine anderen als die angegebenen Quellen und Hilfsmittel benutzt habe.

Heidelberg, den 03. November 2020 .....

Declaration:

I hereby certify that the thesis I am submitting is entirely my own original work except where otherwise indicated.

Heidelberg, November 3rd 2020 .....